Republic of Iraq

Ministry of Higher Education
and Scientific Research

University of Babylon

College of Engineering

Civil Engineering Department

Optimal Hydraulic Design for Flow Deflector in the Stilling Basin of Multi-vents Regulator

A Thesis

Submitted to the College of Engineering University of Babylon in Partial Fulfillment of the Requirements for the Degree of Master of Science in Engineering \ Civil Engineering \ Water Resources

By

Ahmed Raheem Sahib Yaseen

Supervised By

Asst. Prof. Dr. Imad Habeeb Obead

2023 **1445**

بسم الله الرحمن الرحيم

أمَنْ جَعَلَ الأرضَ قَراراً و جَعَلَ خِلالَها أنهاراً و جَعَلَ لَها رواسِيَ وَ جَعَلَ بَينَ البَحرِينِ حاجِزاً أ إلهٌ مَعَ اللهِ بَلْ أكثَرُهُم لا يَعلَمون

صدق الله العلي العظيم

سورة النمل / الآية ﴿ 61 ﴾

Dedication

To my beloved my parents ….

To my beloved my brothers ….

Without whom none of my success would be possible

With my sincere respect and appreciation ….

Ahmed

2023

Acknowledgments

In the name of Allah, the most gracious, the most merciful

Praise be to Allah and prayer and peace be upon the Prophet Mohammed and his posterity the good, the virtuous

Before anything, thank Allah who enabled me to achieve this research despite the difficulties that I faced during that period.

I wish to express my deep gratitude and great appreciation to my supervisor **Asst. Prof. Dr. Imad Habeeb Obead** whom I have the honor to work under his supervision for his guidance and encouragement were indispensable throughout the preparation of this thesis.

I would also like to thank the head and the staff of the university of Babylon as well as the head and the staff of the civil engineering department.

Sincere thanks are expressed to **Al-Nawafith Company (NSGF Co. Ltd.)** for production of sand and gravel filters for supplying me the sand which was used in the experiments without any fees.

Finally, my best thanks and greetings to my beloved family for their continuous guidance at all stages of this work.

Abstract

The research problem addressed in this study is the limited use of theoretical models that incorporate a two-phase flow consisting of water, and sand to simulate and analyze erosion around hydraulic structures. This limitation suggests that there is a need for further investigation into this area. To address this research gap, the present research conducted laboratory experiments and utilized a Computational Fluid Dynamics (CFD) model to investigate the flow properties and scour patterns downstream of a hydraulic structure. Specifically, the study investigated the use of four basic shapes of submerged deflectors (single perforated triangle, double solid triangle, single perforated semi-circle, and double solid semi-circle) with various angles and positions along the flow direction. The aim of the study was to compare the effectiveness of these deflectors in reducing scouring under different flow conditions and to compare them to the case where no deflector was installed. By addressing this research gap, the study aims to contribute to the field of hydraulic engineering and provide insights into the erosion around hydraulic structures.

In this study, Computational Fluid Dynamics (CFD) modeling was used to examine how the location, apex angle of flow deflectors, and passageway percentage influenced the depth of scour across various flow conditions. Four types of deflectors were used, including two single perforated deflectors (semicircular and triangular) and two double solid deflectors (semicircular and triangular). The Navier-Stokes and continuity equations were discretized using a finite volume and finite difference approach to solve fluid motions, while the RNG κ-ε turbulence model was adopted to model turbulence. The excess bed shear stress resulting from the flowing water was used to determine the bed load model, and the Volume of Fluid (VOF) technique was used to model free surfaces. Results indicated that the single semicircular perforated deflector was the most effective in

reducing the maximum local scour depth. This deflector reduced maximum scour depth by about 76.8%, while the double semicircular solid deflector reduced maximum scour depth by about 75.7%. The triangular perforated deflector and double triangular solid deflector reduced maximum scour depth by about 22% and 71.1%, respectively, when compared to the stilling basin without the deflector. These findings recommend that the single semicircular perforated deflector is the optimal choice for reducing maximum local scour depth.

The problem is characterized as a multi-optimization problem, which requires the need to optimize multiple factors simultaneously in order to achieve a reliable solution. The optimization solution results facilitated the estimation of scour depth and the determination of optimal design dimensions for flow deflectors, taking into account conditions similar to those used in this study.

List of Contents

List of Figures

List of Tables

List of Abbreviations

Symbol	Abbreviation
$a_{opening}$	Area of opening area of deflector.
A_t	The total solid area of any type of deflector.
A_x	Fractional areas open to flow in the x direction.
A_y	Fractional areas open to flow in the y direction.
A_z	Fractional areas open to flow in the z direction.
b	Width of opening area between two solid deflectors.
B	Width of channel.
B_g	Width of opening gate.
D_{50}	Median bed material size.
D_{90}	90% finer bed material size.
D_{95}	95% finer bed material size.
d_i	The bed material species i's diameter.
d_s	Depth of maximum scour at equilibrium.
d_{Si}	Is the i^{th} measured depth of scour both for specified flow deflectors.
d_{Si2}	Is the i^{th} predicted depth of scour for the model to be evaluated.
d_{st}	Depth of maximum scour at any time t.
d_t	Tailwater depth.
E%	The efficiency of energy dissipation.
E_1	The specific energy of the flow at the upstream of the flow.
E_2	The specific energy of the flow at the downstream of the flow.
F_d	Particle densimetric froude number.
$F_{d(95)}$	Particle densimetric froude number based on d_{95}.
fi	Reynolds stress.
Fr	Froude number.
Fr_1	Froude number at opening gate.
g_i	Gravitational acceleration in the subscript’s direction.
Gs	Specific gravity.
h	The height of deflector.
h_0	Initial or average flow depth.
h_j	The height of the jump.
h_t	The distance between the apex of the triangular weir and the flume bed.
K_D	Dimentionless multiplying factors expressing the influence on scour depth of bed material size.
K_{dt}	Dimentionless multiplying factors expressing the influence on scour depth of tailwater depth.
K_g	Is the function of geometric shape of the flow deflector.

K_L	Dimentionless multiplying factors expressing the influence on scour depth of apron length.
K_σ	Dimentionless multiplying factors expressing the influence on scour depth of bed material gradation.
L	Length of apron downstream of sluice gate.
L_0	Relative position of the flow deflector.
L_B	Length of the stilling basin.
L_j	The length of a hydraulic jump.
L_S	Corresponding position.
MSE	Mean squared error.
n	Number of opening gates.
N	Is the number of the flow deflectors across the flow.
NSE	Nash Sutcliffe Efficiency coefficient.
P'	Hydrostatic pressure.
PBIAS	Percent bias.
P_k	Turbulent kinetic energy.
q	Discharge per unit width.
Q	Discharge of the hydraulic structure.
R	The radius of semicircular deflector.
R^2	Coefficient of determination.
RMSE	Root mean squared error.
S_{DC}	Solid Surface area of double-solid semi-circular flow deflector.
S_{DT}	Solid Surface area of double-solid triangular flow deflector.
S_{ij}	The mean strain.
S_{SC}	Solid Surface area of single-perforated semi-circular flow deflector.
S_{ST}	Solid surface area of single-perforated triangular flow deflector.
t	Time of scouring.
t_1	Characteristic time at which the maximum scour depth equals $h_{0.}$
u	Velocity components in the x direction.
u_{*c}	Critical bed shear velocity.
v	Velocity components in the y direction.
V_1	Mean flow velocity at the inlet section.
V_2	Mean flow velocity at the outlet section.
V_a	Approach velocity.
V_c	Critical velocity.
V_F	The volume fraction of fluid in each cell.
v_i	The mean velocity of the flow.
w	Velocity components in the z direction.

x	The length of one side of the triangular deflector or the length of perimeter of the semi-circular deflector.
y_1	High of water at the inlet section.
y_2	High of water at the outlet section.
y_m	Maximum scour depth.
α	The correction coefficient of the kinetic energy.
α_0	The proportion of the waterway passages.
γ	Coefficient, $\gamma = 0.4–0.8$.
ΔE	The energy loss.
Δh	Difference between upstream and downstream water level.
η	The dimensionless shear rate.
θ	For a triangular deflector, the apex angle is considered, while for a semicircular deflector, the oriented angle is taken into account.
$\theta_{cr,i}$	The critical shields parameter of species i in the bed material
λ'	Scour factor given by may et al.
μ	Dynamic viscosity.
μ_t	Turbulent dynamic viscosity.
ρ_f	Fluid density.
ρ_i	The bed material species i's density.
ρ_s	Density of bed material.
σ_g	Geometric standard deviation of bed material size.
τ	The local bed shear stress.
τ_{c*}	Shields parameter.
φ	Angle of repose of bed material.
Φ_i	The dimensionless bed-load transport rate.
ω	Bed material fall velocity.

Chapter One

Introduction

1.1 General

The hydraulic structures, such as spillways, weirs, and sluice gates, are installed in waterways for a variety of purposes, including raising the upstream level of water, measuring flow, decreasing flow velocity, and so on, where they are subjected to the effects of high variability water flows. As a result a local scour surrounding the hydraulic structure may occur, which might eventually lead to structural failure **(Bajkowski, 2007)**, Therefore, it is highly recommended to prevent scouring the downstream bed of the waterway if possible or to reduce the dimensions of the scour hole and force it to form away from the end of the stilling basin to maximize the structure's safety.

Scour is the process by which bed material is eroded and transported from the bed of a river or stream. Downstream flow deflectors are designed to redirect the flow of water and can have an impact on scour depth. When water flows around a flow deflector, it creates a local scour hole downstream of the structure. The scour depth is affected by a variety of factors including the velocity and turbulence of the water, the bed material and shape, and the geometry of the hydraulic structure.

The process of scour can be explained as follows: as water flows around the downstream flow deflector, it creates a region of high velocity downstream of the structure. The high velocity water creates a low-pressure zone, which can cause bed material to be eroded from the bed of the river or stream. As the bed material is eroded, it is carried away by the flow of water, deepening the scour hole downstream of the structure **(Akan, 2006)**.

The geometry of the hydraulic structure can also play a role in the depth of scour. A narrow structure will create a deeper scour hole than a wider structure, all else being equal. Similarly, a structure with a more acute angle of deflection will create a deeper scour hole than a structure with a less acute angle.

Many researchers have been studying the local scour downstream of hydraulic structures for several decades to determine the main variables that influence the local scour downstream of structures and to find solutions. It was found that one of the methods for the amount of scouring downstream of a hydraulic structure is to use an appropriate energy dissipator, such as baffle blocks, sills, etc. For many years, several models of energy dissipators have been studied to reduce the scouring phenomena **(Blaisdell, 1948, Dardeer, 2022)**. Even if they are not required to produce a stable hydraulic jump, baffle blocks should be installed in the stilling basin.

1.2 Research Aim and Objectives:

The aim of the present research is to investigate the use of flow deflectors as a means of protecting downstream waterway beds from excessive scouring caused by high-velocity flows. Specifically, the research aims to develop an optimal design for flow deflectors downstream of a multi-vent regulator that will effectively dissipate the energy of hydraulic jumps and stabilize the flow to prevent scouring.

In order to achieve this aim, the following objectives will be pursued:

1) Collecting data on the hydraulic characteristics of the multi-vent regulator and the downstream waterway bed to identify the potential for scouring.
2) Conducting laboratory tests on the use of flow deflectors and consequent scour depth downstream waterway beds and the design principles for multi-vent regulators.

3) Developing numerical models to simulate the hydraulic behavior of the flow deflectors downstream of the multi-vent regulator, including the scouring patterns.
4) Analyzing the effect of different flow deflector designs on the hydraulic behavior of the flow downstream of the multi-vent regulator, with a focus on energy dissipation and scour prevention.
5) Optimizing the flow deflector design based on the results of the numerical modeling and analysis. In addition, validating the optimized design through physical modeling and field testing.

1.3 Organization of the Thesis

The following is a summary of the five chapters that introduce the research outlines and results.

In Chapter Two, a literature review is presented which covers the fundamental concepts of scour, theoretical and experimental research related to predicting scour depth, as well as scour under submerged flow conditions beyond the deflectors.

Chapter Three focuses on the methodology employed in the present research, including details on the experimental equipment, models, and procedures.

In Chapter Four, the results of laboratory and numerical analysis run for various types of deflectors and flow conditions are presented along with a comprehensive discussion. In addition, the chapter provides a detailed explanation of how the optimization problem for designing optimal flow deflectors is formulated, solved, and verified.

Chapter Five, the key conclusions from this research are summarized, and recommendations for future studies are presented.

Chapter Two

Theoretical Aspects And Review Of Literature

2.1 General

The hydraulic structure's stability is influenced by scour downstream of the stilling basin. This is because the scour can lead to erosion of the soil and bed material around the foundation, which weakens the structure's support and stability. Scouring can be caused by various factors, such as high velocity flows, bed material transport, and changes in water levels. Due to the complicated nature of the flow and the interaction between the flow and the bed material downstream of the stilling basin, the approach has mainly been empirical in estimating the scour hole's characteristic features, such as maximum depth, distance from the end of a rigid apron, scour hole extent, maximum height of the dune, and so on **(Aamir and Ahmad, 2016)** . The phenomenon of scour near the hydraulic structures has taken the attention of several studies because of its importance in ensuring the safety of these structures.

An overview of the theoretical aspects of the bed scours phenomenon with an intensive but brief review of relevant studies that cover such phenomenon will be presented in this chapter.

2.2 Hydraulic Jump

A hydraulic jump is a sudden change in water flow characteristics within a channel. It occurs in short channel segments where friction is negligible compared to other forces. Hydraulic jumps are marked by high velocity and momentum coefficients, resulting in complex flow patterns. They transition the flow from supercritical to subcritical, leading to a discontinuous surface profile with turbulence and energy loss. The behavior of hydraulic jumps is categorized based on the Froude number as shown in Figure (2.1), with ranges from impossible jumps to stable, well-balanced ones. These jumps have different characteristics and energy dissipation levels as shown in Figure (2.2).

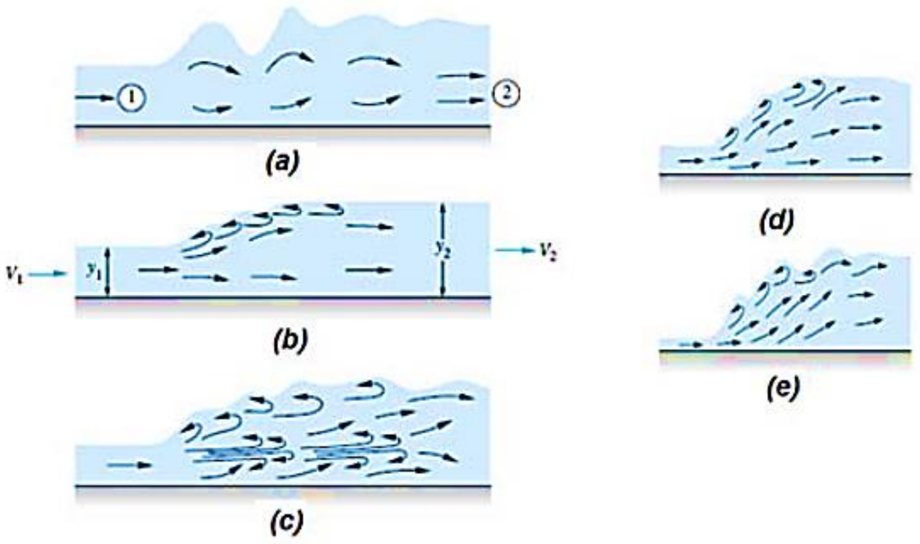

(a) Fr = 1.0 to 1.7: undular jumps;
(b) Fr = 1.7 to 2.5: weak jump;
(c) Fr = 2.5 to 4.5: oscillating jump;
(d) Fr = 4.5 to 9.0: steady jump
(e) Fr ≥ 9.0 : Strong jump

Figure (2.1): Types of hydraulic jumps.

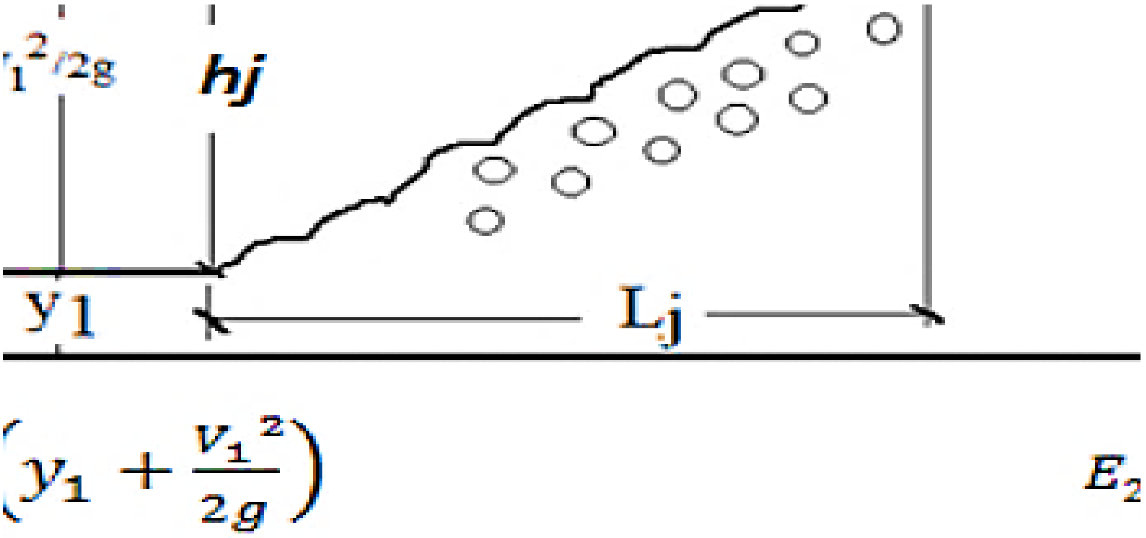

Figure (2.2): Simple hydraulic jump on horizontal bed.

E_1: Specific energy before jump.

E_2: Specific energy after jump.

ΔE: The energy loss.

y_1, y_2: depth of water at section 1 and 2 respectively.

h_j is the height of the jump = $(y_2 - y_1)$

V_1, V_2: mean velocity of water at section 1 and 2 respectively.

Fr: Froude numbers are: $Fr_1 = \frac{V_1}{\sqrt{g\,y_1}}$; $Fr_2 = \frac{V_2}{\sqrt{g\,y_2}}$

L_j The length of a hydraulic jump=$k(y_2 - y_1)$

2.3 Fundamental Concepts of the Scour Phenomenon

The scour phenomenon refers to the erosion of bed material around structures such as bridge piers, culverts, or offshore foundations, caused by the flow of water as shown in Figure (2.3). The fundamental concept behind scour is that the flow of water around a structure creates pressure differences and turbulence, which can cause the bed material to be eroded and removed from around the structure **(Pizarro et al., 2020)**.

Among many different types of scours, the local scour was occurring because of the concentration of turbulence generated by structures, which block and separated the flow such as bridge piers, abutments, and flow deflectors. It arises due to the limited extent of their influence on the flow of the river. The key factors that affect scour include the velocity of the water, the geometry of the structure, the type of bed material around the structure, and the duration of the flow.

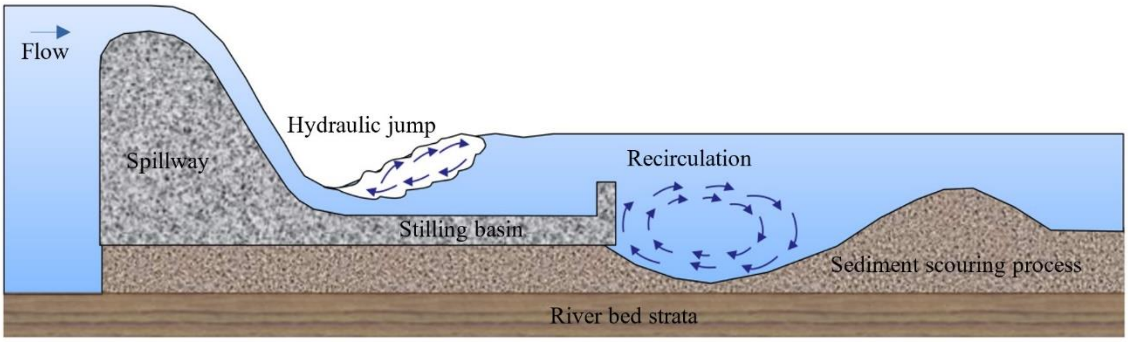

Figure (2.3): Bed material scouring process **(Padhi, 2022).**

In order to predict scour at positions with the complicated three-dimensional flow, physical models are used in combination with the computational results of horizontal (depth-averaged, two-dimensional) numerical models. **Breusers (1966)** stated that the turbulence level at the boundary between both erodible and the fixed beds and the flow rate determine how the scouring process develops. By using this idea, the scour prediction can be constrained to a single computation.

When dealing with concerns related to local scour, only the scour that has the maximum depth in the equilibrium phase is essential **(Hoffmans and Verheij, 2022)**. This is especially valid for stationary hydraulic structures that are isolated, such as spur dikes, bridge piers, and other permanent structures (weirs, final closure works, and sills). However, there are situations in which the passage of time is crucial, such as when water body branches must be closed.

Zanke (1978) identified four phases in the formation of a scour hole, as shown in Figure (2.4), according to clear-water scour laboratory tests, that is, no upstream sediment transport, using small Froude numbers with scale models **(Breusers, 1966)**. These phases are the initial phase, the development phase, the stabilization phase, and the equilibrium phase.

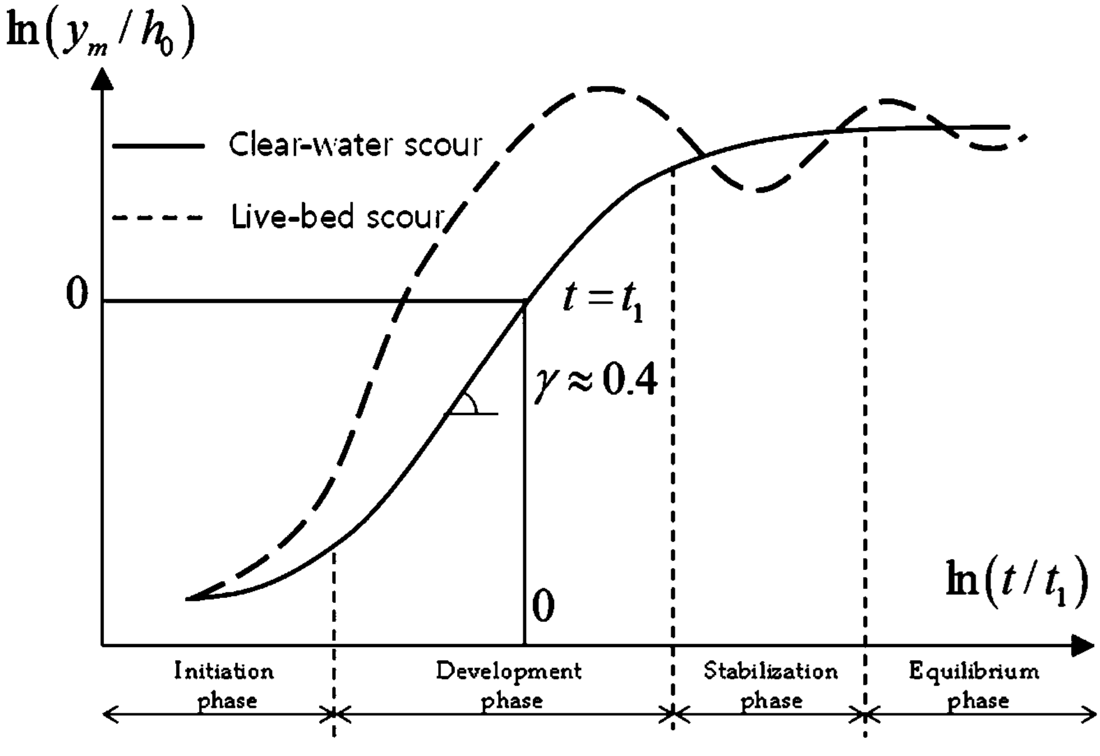

Figure (2.4): Development of the scour process **(Park et al., 2019).**

γ: Coefficient, $\gamma = 0.4$–0.8

t=Time

y_m= Maximum scour depth

h_0 =Initial or average flow depth

t_1=Characteristic time at which the maximum scour depth equals h_0

In the initial phase, the flow in the longitudinal direction of the scour hole is nearly uniform. The most severe erosion capacity is present during this phase of the scouring process, which can be described as this phase. Numerous investigations, which utilized fine bed material (e.g., Breusers' study in 1966), revealed that some bed material close to the upstream scouring slope went into suspension at the start of the scouring process. Because of the internal balance between the downward flux caused by gravity and the upward diffusive flux, the majority of the suspended particles stay in suspension within the main flow by following convectional paths. Due to the intense turbulent flow close to the bed, some of the particles will settle and be re-suspended. Other particles are transported as bed loads if they jump below a specified saltation or reference height.

During the development phase, the depth of the scour increases significantly while the scour hole's shape remains relatively unchanged. In this stage, there is a fairly constant relationship between the maximum local scour depth and the distance between the end of the stilling basin and the maximum local scour depth. **Hoffmans (1990)** conducted measurements that revealed the upper portion of the upstream scour slope is in equilibrium while the lower portion is still forming. In comparison to the situation in the initial phase, the suspended load close to the bed significantly decreases. Despite an increase in turbulent energy, the main cause of this is the gradual decline in flow velocities close to the bed. Even though the flow picks up and carries bed particles, the instantaneous velocities in the upstream and downstream directions produce roughly equal contributions to bed material transport, making the value of bed material transport time-averaged at the upstream scour slope's upper part negligible.

In the stabilization phase, the maximum scour depth development rate slows down. Due to the fact that the scour hole's deepest portion has a lower erosion capacity than the region downstream of the point of reattachment, the scour hole's dimensions increase more longitudinally than vertically. The flow velocities above the lower portion of the upstream scouring slope decrease as the scouring process progresses. The equilibrium condition for the maximum scour depth and the upstream scour slope is almost attained during the stabilization phase. The phase in which there are no notable changes to the scour hole's dimensions is known as the equilibrium phase.

Van der meulen and Vinjé (1975) investigated the downstream three-dimensional scour process of a partial waterway constriction (according to more than a hundred tests with bed protections that are hydraulically smooth, medium, or rough). He found that the scour hole's shape is unaffected by bed material or flow velocity.

2.4 Prediction of Scour Depth

Prediction of scour depth is a process that aims to estimate the amount of erosion that may occur around a structure due to the movement of water. This involves the analysis of many factors such as flow velocity, bed material type, and water depth to determine the likelihood and extent of scour. These findings are then used to design appropriate measures to mitigate the potential risks associated with scouring. This section provides a concise overview of previous research concerning the use or not of flow deflectors in stilling basins.

2.5 The stilling basin.

During the period from the 1940 to the 1960, a diverse range of standard stilling basin designs was developed and extensively tested using models and prototypes under various flow conditions. As a result of these comprehensive tests, the performance characteristics of these prototypes have been thoroughly understood.

The accumulation of extensive observations, practical experience, and model studies has led to the establishment of several standard designs for stilling basins. Figure (2.5) in the report by the US Bureau of Reclamation (1987) displays three common types of stilling basins. These designs incorporate chute blocks at the entrance to not only stabilize but also shorten the length of the jump. Moreover, the addition of solid or dented end sills at the basin's end further aids in reducing the jump length. Baffle piers strategically positioned at intermediate locations within the stilling basin facilitate energy dissipation through impact. The choice of the appropriate stilling basin type depends on the upstream Froude number, as different flow conditions require specific designs for optimal performance. It is crucial to note that when referencing the findings or information from this report, proper citation and acknowledgment of the original source are necessary.

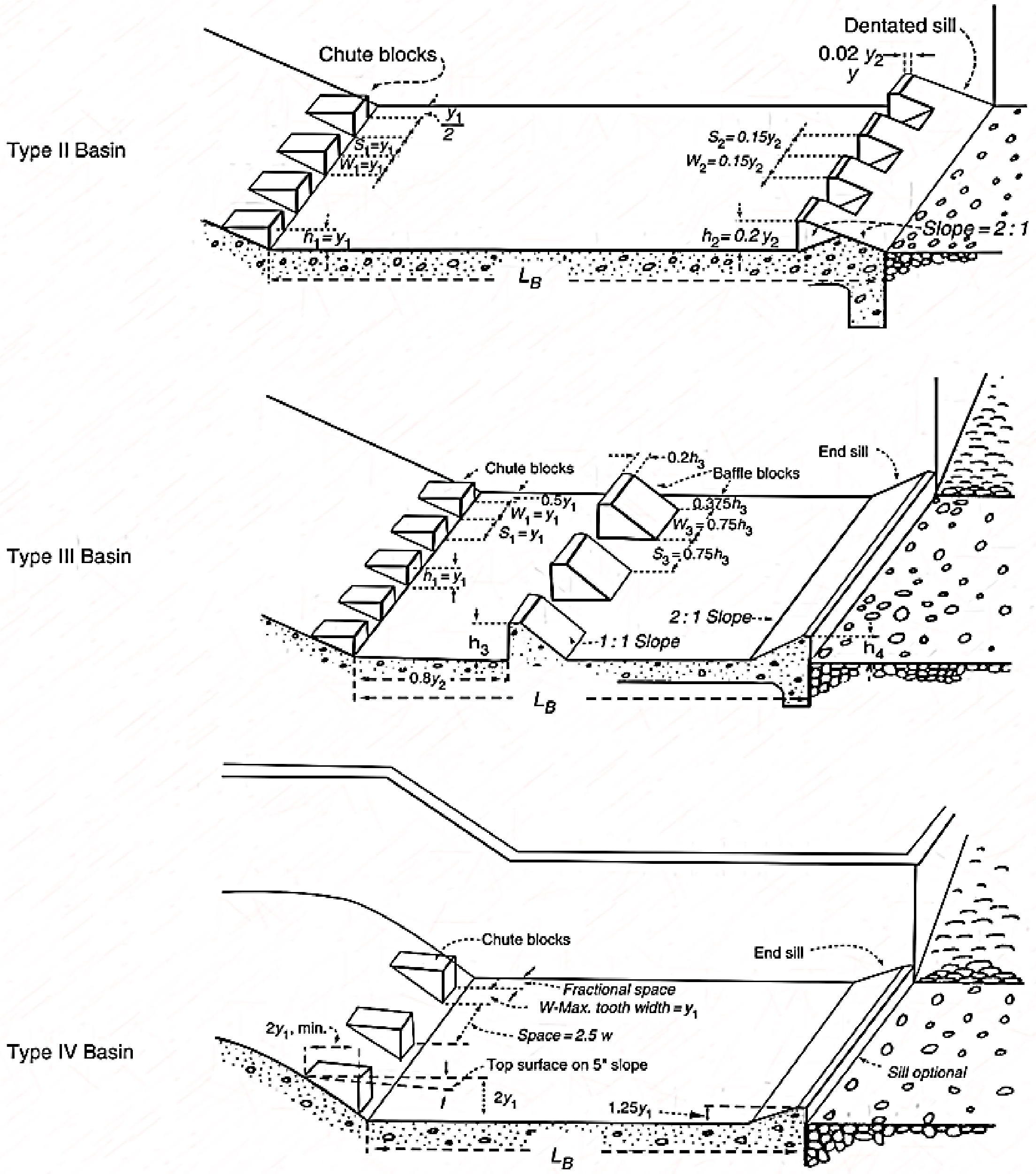

Figure (2.5): Standard designs for stilling basins after the US Bureau of Reclamation (1987).

2.5.1 Hydraulic Design of Standard Stilling Basin

For Froude numbers falling within the range of 2.5 to 4.5, it is recommended to use Type IV basins. In specific situations, the inclusion of auxiliary wave dampeners or wave suppressors becomes necessary to maintain a uniform flow downstream. To control the spread of the hydraulic jump and aid in wave suppression, it is essential to maintain water depths in the basin that are approximately 10% greater than the calculated conjugate depth. In simpler terms, the basin depth (y_t) should be designed to be 1.1 times greater than the conjugate depth (y_2). To determine the appropriate length of the basin, refer to Figure (2.6), **(Akan, 2006)**.

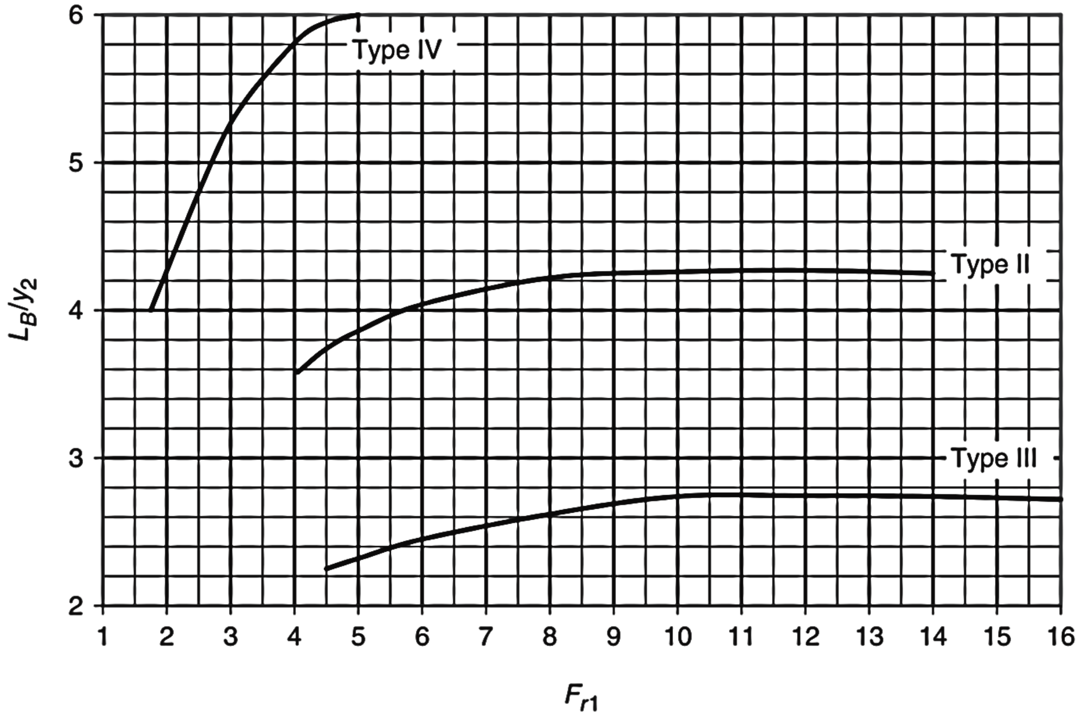

Figure (2.6): Length of the stilling basin after the US Bureau of Reclamation (1987).

For Froude numbers above 4.5 and incoming velocities (V_1) below 20 m/sec, Type III basins are used. These basins utilize chute blocks, impact baffle blocks, and an end sill to reduce the jump length and dissipate high-velocity flow within the basin. In Figure (2.5), the height of the chute blocks (h_1) equals y_1 **(Akan, 2006)**.

The height of the baffle blocks (h_3) can be calculated using a specific formula:

$$h_3=y_1\left[\left(1.30+0.164(Fr_1-4.0)\right)\right]$$

The height of the end sill (h_4) is given by Roberson et al. (1998):

$$h_4=y_1\left[\left(1.25+0.056(Fr_1-4.0)\right)\right]$$

The length of the basin can be determined from the Figure (2.6). If the Froude numbers exceed 4.5 and the inflow velocities go beyond 20 m/sec, or if impact baffle blocks are not employed, the type II basin becomes a suitable option. Dissipation in this type of basin mainly depends on hydraulic jump action, resulting in a longer basin compared to the type III basin. However, the inclusion of chute blocks and end sill remain effectively reduces the overall length.

For adequate dissipation, maintain the tail-water depth in the basin at around 5% higher than the calculated conjugate depth (y_T) **(Chanson, 2015)**:

$$y_T=1.05y_2$$

The floor elevation for stilling basins must be chosen carefully, considering the tail-water. The design's critical aim is to prevent the hydraulic jump from extending beyond the basins into the natural stream channel, regardless of the discharge over the spillway. This is achieved by comparing calculated conjugate depths with tail-water depths for various discharges. For an efficient design, the tail-water depths should be slightly greater than the conjugate depths. If the conjugate depth exceeds the tail-water depth, there is a risk of the hydraulic jump escaping into the natural stream. Conversely, if the conjugate depth is much smaller, the hydraulic jump will be fully submerged and ineffective.

2.5.2 Stilling Basin without Flow Deflectors

Several researchers conducted experimental investigations that resulted in various scour prediction models, a summary of these studies were presented in Table (2.1).

Ali et al. (2014) conducted an experimental study to investigate the impact of different spaced corrugated aprons on downstream local scour caused by submerged jumps. The study involved sixty runs in a horizontal rectangular flume, aiming to identify the most effective corrugation wavelength for minimizing scour. It was used two types of non-cohesive soil and conducted experiments under various Froude numbers. The results indicated that using spaced triangular corrugated aprons resulted in substantial reductions in scour depth and length for both fine and coarse sand. Specifically, the reductions averaged 63.4% and 30.2% for fine sand and 44.2% and 20.6% for coarse sand, as compared to classical jumps. Additionally, the research highlighted that scour depth and length displayed an inverse relationship with the mean diameter of grain size particles.

Helal (2014) carried out an extensive study, running 117 experiments, to explore how a single row of floor water jets affects scour hole characteristics downstream of a control structure. They tested different jet discharges, positions, and tailwater depths. The results showed that using these floor water jets significantly reduced the maximum scour depth (by 50% to 90%) and the length of the scour hole (by 42% to 85%) compared to scenarios without the jets. Furthermore, this system effectively moved the maximum scour depth closer to the floor. The most effective location for the water jets was found to be 40% of the floor length away from the weir toe. When jet discharge values were increased, it led to higher maximum scour depth, a longer scour hole, and a shift in the location of maximum scour depth away from the floor end.

Table (2.1): Prediction equations of local scour depth under submerged wall jets proposed by different investigators **(Aamir and Ahmad, 2016)**.

Investigator	Equation
Eggenberger and Mueller (1944)	$d_s + d_t = \omega_e \frac{\Delta h^{0.5} * q^{0.6}}{D_{90}^{0.4}}$; where ω_e = a coefficient
Valentin (1967)	$\log(\frac{d_s}{y_1}) = \frac{Fr_1 - 2}{4.7} - 0.55\log(\frac{D_{90}}{y_1})$
Altinbilek and Basmaci (1973)	$\frac{d_s}{y_1} = (\frac{y_1}{D_{50}} \tan\emptyset)^{0.5} F_d^{1.5}$
Ali and Lim (1986)	$d_s + d_t = 2.3F_d^{0.75}\left(\frac{V_1}{\omega}\right)^{0.5}\left(\frac{D_{50}}{R'}\right)^{0.375} - 1.19$; where ω=sediment fall velocity ; R'= hydraulic radius of the jet, defined as (a) R'= for a deeply submerged 2D jet issuing from sluice opining with a well-rounded lip; (b) $R'= \alpha_1$ for a deeply submerged 2D jet issuing from sharp sluice gate ;and ; (c) R'= the ratio of jet area to its parameter for 2D and 3D jets with shallow tailwater depth; where α_1= thickness of jet at vena contracta.
Breusers and Raudkivi (1991)	$\frac{d_s}{y_1} = 0.008(\frac{V_1}{u_{*c}})^2$; where u_{*c}= critical bed shear velocity
Chatterjee et al. (1994)	$\frac{d_s}{y_1} = 0.775Fr_1$
Hoffmans (1998)	$\frac{d_s}{y_1} = \frac{50}{\lambda'}(1 - \frac{V_2}{V_1})$; where λ'=scour factor given by **may et al**., wich is defined by and $\lambda' = 2.95D_{90}^{0.33}$;for $0.1 < D_{90} < 12.5$ mm and $\lambda' = 6.85$:for $D_{90} > 12.5$ mm
Aderibigbe and Rajaratnam (1998)	$\frac{d_s}{y_1} = 2.3F_{d(95)} - 6.11$
Lim and Yu (2002)	$\frac{d_s}{y_1} = 1.04F_d^{1.47}\sigma_g^{-0.69}\left(\frac{D_{50}}{y_1}\right)^{0.33} k_L'$; where k_L'=factor to account for the effects of an apron downstream from the outlet, which is given by $k_L' = e^{-0.004F_d^{-0.35}\sigma_g^{-0.5}\left(\frac{D_{50}}{y_1}\right)^{-0.5}\left(\frac{L}{y_1}\right)^{1.4}}$
Dey and Westrich (2003)	$\frac{d_{st}}{y_1} = 0.00886\left(\frac{tV}{y_1}\right)^{0.429}\left(\frac{L}{y_1}\right)^{-0.648}\left(\frac{d_t}{y_1}\right)^{0.949}(\frac{\Delta h}{y_1})^{0.216}$
Hopfinger et al. (2004)	$\frac{d_s}{y_1} = \left[\frac{0.01tan\emptyset}{\tau_c'}\right]^{0.55} F_d^{1.1}\left(\frac{D_{50}}{y_1}\right)^{0.11} - 0.2$
Sarkar and Dey (2005)	$\frac{d_s}{y_1} = 0.42F_d^{0.49}\left(\frac{L}{y_1}\right)^{-0.36}\left(\frac{d_t}{y_1}\right)^{1.08}$
Dey and Sarkar (2006)	$\frac{d_s}{y_1} = 2.59F_d^{0.94}\left(\frac{L}{y_1}\right)^{-0.37}\left(\frac{d_t}{y_1}\right)^{0.16}\left(\frac{D_{50}}{y_1}\right)^{0.25}$
Mellvile and Lim (2014)	$\frac{d_s}{y_1} = 3FK_D K_{dt} K_\sigma K_L$; where Ks are dimentionless multiplying factors expressing the influence on scour depth of sediment size (K_D),tailwater depth (K_{dt}),sediment gradation (K_σ), and apron length (K_L)

y_1 = high of opening gate.

d_s = Depth of maximum scour at equilibrium

d_t = Tailwater depth

d_{st} = Depth of maximum scour at any time t

Fr_1 = Froude number at opening gate

F_d = Particle densimetric Froude number

$F_{d(95)}$ = Particle densimetric Froude number based on D_{95}

Δh = Difference between upstream and downstream water level

L = Length of apron downstream of sluice gate

q = Discharge per unit width

V_1 = mean flow velocity at the inlet section.

V_2= mean flow velocity at the outlet section+

t = Time of scouring

D_{50} = Median sediment size

D_{95} = 95% finer sediment size

D_{90} = 90% finer sediment size

φ = Angle of repose

σ_g = Geometric standard deviation of bed material size

τ_{c*} = Shields parameter

Aamir and Ahmad (2016) presented a thorough analysis of the research conducted on local scour caused by wall jets, highlighting the key factors that influence the scouring process and providing insight into the flow characteristics within the scour hole and on the apron. Also, a range of formulas for estimating scour depth were offered, which could prove invaluable in developing effective remedial measures to mitigate against this phenomenon. It was found that a better understanding of the scouring process and its parameters is essential to developing accurate prediction models for local scour caused by wall jets. Further research is needed to address the impact of apron roughness on maximum scour depth, the response of jets to cohesive beds, and the flow characteristics over a mixture of bed materials. Additionally, large-scale model studies are necessary to gain insight into these problems, as laboratory models may not accurately represent the characteristics of flow in the prototype.

Aamir et al. (2022) conducted an experimental study to examine the scour downstream of rough and smooth stiff aprons influenced by wall jets, and the impact of various parameters on the scour depth. The findings of the analysis indicate that the maximum scour depth decreases as bed material size, sluice opening, and apron length increase, while it is directly proportional to the densimetric Froude number. Initially, the maximum scour depth decreases with an increase in the tailwater level, reaching a minimum, but thereafter it starts to increase. Based on the conclusions drawn from this study, it is recommended to incorporate roughness on the surface of stiff aprons to confine scour caused by under-wall jets. The application of roughness results in a significant reduction in the maximum scour depth, ranging between 70% and 83%.

2.5.3 Stilling Basins with Flow Deflectors

A stilling basin with a flow deflector is a type of stilling basin that is designed to reduce the velocity of the water more efficiently by deflecting the water flow. The flow deflector can also be designed to create turbulence, which can help to dissipate energy effectively. The deflector can be placed either upstream or downstream of the basin, depending on the specific design and function of the stilling basin.

The addition of a flow deflector can have a significant impact on the scouring potential of a stilling basin. It can modify the flow characteristics of the water, changing the bed material transport patterns, and affecting the rate and extent of scour. As a result, predicting scour depths in stilling basins with flow deflectors requires careful consideration of various factors, such as the geometry of the deflector, the angle of incidence of the water flow, and the bed material characteristics **(Pagliara et al., 2009)**.

EL-masry and Sarhan (2000) conducted 153 experiments to study the impact of using a single line of V-baffles , characterized by a 90° apex angle, in order to minimize the effects of excessive severe scouring of downstream water structures. The effects of the deflector location and the deflector height under various Froude numbers were tested. It was found that V-baffles significantly reduced the scour hole compared to no baffles. Furthermore, Locating the suggested baffles near the middle of the floor gives the most reduction on the depth of scour. Additionally, when the distance between baffles line and the toe of the weir increases, the effect of changing the height of baffles has small influence on scour hole depth

Saleh et al. (2004) conducted an experimental investigation to examine how the inclusion of end sills in sudden expanding stilling basins affected the scour downstream. The study encompassed three different expansion ratios and five different sill heights. It was found that, the scour occurring downstream of the basins with end sills exhibited an asymmetric pattern. The presence of end sills led to a minor alteration in the flow pattern upstream but had a significant impact in the immediate downstream area. The extent of scour and deposition was found to be dependent on factors such as the Froude number, end sill height, and expansion ratio. To prevent the deflection of the primary flow jet just downstream, it was observed that the height of the end sill should not exceed the dominant height of the gate.

Biron et al. (2005) studied the three-dimensional mean and turbulent flow characteristics around paired flow deflectors for three deflector angles (45^o, 90^o, and 135^o) and two deflector heights (with flow under and over the deflector height) over a smooth (plexiglass) bed and a sandabed. Three-dimensional velocity measures were performed with an acoustic doppler velocimeter at multiple planform locations at two elevations above theabed. It was shown that the deflectors with an angle of 90° create the most significant disturbance in the mean flow field, turbulence intensity, and bed shear stress. Above a plane bed, deflectors oriented upstream (135°) and downstream (45°) have the same mean velocity, turbulence intensity, and shear stress patterns, whereas the 135° orientation creates a turbulent flow field disturbance similar to the 90° design over a mobile bed.

Yu et al. (2007) performed an experimental investigation of the scour characteristics of a V-deflector. This study examined the effect of the angle of alignment, the opening width to the total channel width ratio, and the approach flow Froude number. It was found that the V-deflector angle of alignment that changed between (50°-130°) has a slight impact on the scour depth, while, the opening width to the total channel width ratio, and the approach flow Froude number particularly influence the maximum scour depth. The scour mechanism for a V-deflector was found to be similar to that of a dike. Generally, the volume of scour was observed to be proportional to the square of the maximum scour depth. Generally, scour holes take an elliptic shape.

Negm et al. (2008) investigated the effects of flow submergence, Froude number, and operation policy on the dimensions of scour in multi-vent regulator through a laboratory study. Their results showed that the implementation of a curved deflector was highly effective in reducing local scour of downstream multi-vent regulators, achieving a reduction of approximately 85%. They also observed that the relative maximum scour depth increased as the initial Froude number increased. However, an increase in the submergence ratio resulted in a decrease in the relative maximum scour depth. Based on their findings, they determined that the curved deflector's optimal location, which minimized scour dimensions and promoted symmetric flow, was at a distance of 6% of the stilling basin length from the sudden expansion.

Mostafa et al. (2009) conducted an experimental study focused on minimizing scouring operations at downstream (DS) heading-up structures. The study was conducted in a trapezoidal cross-section channel. It was observed that the presence of a guide wall deflector, fixed at 0.35 times the length of the basin, resulted in a significant reduction in the maximum relative scour depth and length. The study also revealed that the maximum relative scour depth increased as the initial Froude number increased.

Ibrahim and Negm (2009) investigated the influence of the height of the curved deflector on the maximum scour depth by conducting experiments under various factors, such as flow submergence, Froude number, and operational gate scenarios. The results of their study revealed a significant decrease of over 80% in the relative maximum scour depth as the deflector's height was increased. The researchers also found that optimal gate operation scenarios involved symmetrical regulation, either fully or partially. Furthermore, increasing the initial Froude numbers led to an increase in both the maximum relative scour depth and length.

Negm et al. (2009a) conducted an experimental study to examine the effects of different factors on the maximum scour dimensions (depth and length) in the stilling basin of multi-vent regulators. The factors investigated comprised the percentage waterway passage of the curved deflector, the Froude number, and the gate operation policy. The study's results demonstrated that a waterway passage of 28% resulted in minimized scour dimensions, with an average reduction of 86% in maximum scour depth when the deflector was optimally positioned. To achieve effective scour reduction, the researchers recommended symmetric gate operation and the use of a curved deflector with 28% opened area, placed optimally at a distance of 6% of the stilling basin length from the sudden expansion. Furthermore, it was observed that the relative maximum scour depth increased as the initial Froude number rose for all waterway passage values.

Negm et al. (2009b) conducted a study to assess the efficacy of a curved hollowed deflector in mitigating scour in multi-vents structures under submerged hydraulic jump conditions. The study specifically focused on experimentally testing the width and orientation angle of the curved deflector using various models and under different submerged flow conditions. The results indicated that the optimal width of the deflector should be limited to a maximum of 75% of the basin's width. Additionally, the investigation revealed that, across all tested cases and for different values of relative width and angle of the deflector, the relative maximum scour depth demonstrated an increase with higher initial Froude numbers. Nevertheless, it was determined that the ideal angle for the deflector was 0.5π (or 90°), as this particular configuration effectively minimized both the relative maximum scour depth and the relative distance to the maximum scour.

Samad et al. (2012) conducted 189 experimental runs to investigate the mitigation of scour downstream of control structures using semi-circular sills. Various sill heights and positions were considered under different flow conditions, including a case without a sill for comparison. The results revealed that all proposed sill arrangements effectively reduced the maximum scour hole depth and length, bringing the maximum scour depth closer to the floor. Sill height was found to have a significant influence on the scour hole characteristics compared to sill location. Additionally, increasing the tail Froude number led to slight reductions in maximum scour depth and length for all sill configurations, causing the maximum scour depth to shift further away from the floor in the flow direction. Additionally, the implementation of a single line of semi-circular sill resulted in the loss of less than half of the initial specific energy during the hydraulic jump.

Helal et al. (2013) tested the effect of using sill on scour downstream. So, 144 runs were conducted using different heights (2, 4, and 6 cm) and different positions (40%, 50%, 60%, and 70% from floor length) under different flow conditions. Three scenarios were investigated: no sill, single-line sill, and fully silled floor. The local scour parameters were found to be minimized when the height of the sill was 4% of the length of the stilling basin, while the maximum local scour occurred when the ratio of the height of the sill to the length of the stilling basin was 1.3%. The maximum scour depth was reduced as the kinetic flow factor ($1/Fr^2$) was increased. Also, it was found that the scenario of a fully silled floor has the minimum local scour downstream.

Abdelhaleem (2013) carried out an experimental investigation to address scour downstream using semi-circular baffle blocks. The study comprised 153 runs under different flow conditions, examining various baffle block heights and positions. The inclusion of baffle blocks had a notable influence on the scour hole, leading to smaller dimensions compared to cases with no baffles. All suggested baffle block arrangements effectively decreased the maximum scour depth and length and moved the maximum scour depth closer to the floor. The height of the baffles had a more prominent impact on scouring characteristics than their location. The best arrangement involved a baffle height equal to 133% of the outer baffle's diameter and a distance between the baffles line and the weir toe equal to 40% of the floor length, resulting in a maximum reduction in scour length ranging from 77.06% to 93.66%.

Pagliara et al. (2015) tested the effects of two types of deflectors, single-wing and double-wing log deflectors, on the scour morphology downstream. It was found that the tailwater and the deflector angle had an important effect on maximum scour depth. Scour morphology is classified into two types: Type C (the maximum scour occurs at the deflector's end towards the channel's center) and Type D (the maximal scour point occurs towards the channel bank).

Kurdistani and Pagliara (2015) conducted a comparison between two types of energy dissipators, namely log-deflectors and log-vanesو, to assess their impact on downstream scour. The study identified the height of the structure, drop height, and densiometric Froude number as crucial variables for classifying scour typology. Four distinct scour typologies were observed downstream of log-deflectors and log-vanes. When the densiometric Froude number is high, the installation of a log-deflector results in Type D typology, characterized by the development of a dune and maximum scour towards the channel bank. Conversely, the installation of a log-vane leads to Type A typology, where the dune forms near the channel bank adjacent to the scour hole. For low densiometric Froude numbers, a log-deflector induces Type C typology, with the maximum scour point occurring at the deflector's end towards the channel's center. On the other hand, a log-vane generates Type B typology, where the dune develops along the scour hole towards the channel's center.

Kang (2016) studied the effect of flow dissipation from various types of energy dissipator arrangements in various directions with fixed weirs and movable weirs on downstream scouring. It was found that, Because the maximum water level did not face flow resistance, the maximum flow velocity at the downstream of the weir was reduced, and the water level was higher than in Case 1 (no baffle installation), and the dissipation effect was 30% or higher (for cases 5, 6, 7, 8, and 9; case 9 had the highest dissipation effect). When comparing dissipation efficiency based on the number of baffles, case 6 (V-shaped arrangement) has the fewest baffles and the most significant flow velocity dissipation effect at the downstream.

Ashour et al. (2016) conducted an experimental study to assess the effectiveness of a novel curved dissipator, which had different angles of curvature and arrangements, in dissipating kinetic water energy and improving irrigation water quality by adding dissolved oxygen. The study involved conducting 660 runs at various discharge rates. The results indicated that using a maximum of three staggered-separate rows of the newly introduced curved dissipator, with a 120° curvature angle opposite to the flow direction, was recommended to achieve the highest percentage of water energy dissipation downstream of head structures and maximum dissolved oxygen content. This arrangement demonstrated the best hydraulic jump characteristics, along with reduced relative depth and length, compared to other tested dissipators.

Kang (2017) conducted an experimental study to analyze the dissipation effect of a baffle shape used to mitigate scour problems downstream of a weir. The study focused on investigating the flow dissipation effect caused by changes in the baffle shape through hydraulic experiments under a fixed bed condition. The study compared the flow dissipation effect achieved by five different baffle shapes, considering two flow rate conditions: when the water level in the super-critical flow area was lower than the baffle height and when it flowed over the baffle. The results indicated that a square baffle with a large flow blocking area exhibited the best flow dissipation effect, achieving approximately 65% flow dissipation. Additionally, when the front part of the baffle was inclined, it induced flow in the upward direction, facilitating hydraulic jumps.

Sohrabi et al. (2018) conducted a laboratory study to investigate the mitigation of bed and bank scouring in rivers. They examined the efficacy of six types of bed sills, including concave, convex, sine, butterfly, wing, and rectilinear shapes, in 18 different configurations. The main focus was to measure the pattern and depth of scouring downstream of these bed sills. Results showed that the sine-shaped bed sill outperformed the others in stabilizing both the centerline and bank of the channel. The study also revealed that the location and depth of scouring holes varied depending on the shape of the bed sills, with concave and convex shapes resulting in the maximum and minimum scour depths, respectively. Overall, using sine bed sills with a specific diameter ratio proved to be effective in stabilizing bed material and protecting both the centerline and bank of the channel from scouring.

Xie et al. (2020) presented a novel flexible deflector of flow to reduce the impacts of local scour that consequence from the variation of patterns of flow. This study was conducted experimentally to measure scour depth and flow field by considering a rigid flow deflector as a control. They concluded that the bed-scour generated at the toe edges of toe for both rigid and flexible deflectors, however, the measured average and maximum depths of scour are smaller for the flexible deflector. In addition, the flexible deflector dissipates much energy of turbulence due to the rise and fall waving movement, in which assist to reduce energy, on the other hand, the rigid type causes lower near-bed shear stress.

Zhang et al. (2021) conducted an experiment on scouring in clear water at a submerged weir. This study used the technique of particle tracking velocimetry for measuring the flow field in the generated hole of the scour. A presentation and discussion on the near-bed shear stress, turbulence intensities, and patterns of mean flow were performed at various stages of the scouring process. It was found that a significant variation in the patterns of mean flow was caused by the submerged weir that was developing zones of high velocity above the weir, and a system of vortex near the bed. As well, when the scour forms, both zones of high turbulence intensity and the high near-bed shear stress become closer to the upstream slope, and more apart from the downstream slope of the hole of scour. When reaching the equilibrium state, the near-bed shear stress exceeds the critical shear stress in the upstream slope of the hole of scour, while bed material transports in a reverse circular manner in which the hole of scouring no more enlarges.

Kumcu and Ispir (2022) conducted a study aiming to explore the energy dissipation ratios of baffle blocks within a Type III stilling basin, utilizing both physical and numerical modeling techniques. The investigation encompassed baffle blocks with uniform dimensions, sharing equal heights and widths, while their total lengths were tailored to be 50% of the width of the stilling basin. Four distinct geometric shapes of baffle blocks were examined across three layout variations: single row, two rows, and two rows without a threshold structure. This comprehensive approach led to the analysis of 12 diverse block designs under 7 different flow rates. To further validate their findings, the researchers employed the FLOW-3D software for experimental simulations, enabling a comparison between experimental and numerical results. The study revealed that the T-shaped energy-dissipating block exhibited the highest energy dissipation ratio. Notably, a close agreement was observed between the results obtained from the experimental studies and the FLOW-3D software, falling within a 5% range of similarity.

Dardeer (2022) conducted a research study at Al-Azhar University's Hydraulic Laboratory to examine the influence of semi-circular baffle blocks on scour downstream of sluice gates. Using a flume equipped with measurement instruments, 40 experiments were performed. The study considered three different ratios of the diameter to height of the baffle blocks and three ratios of their placement from the gate to the length of the apron downstream. Comparative runs were conducted without the semi-circular baffle blocks as a reference. The findings revealed that implementing a diameter-to-height ratio of 0.78 resulted in reduced scour length and depth, particularly at a placement ratio of 0.37.

Rashed et al. (2022) conducted a research study to investigate the impact of hollow semi-circular baffles on the dimensions of scour holes downstream of hydraulic heading-up structures. A total of fifty-four experiments were conducted under various flow conditions and geometrical parameters. The results indicated that the optimal position for the baffle was at the first one-third of the floor length, with a relative diameter of 0.74 to the initial water depth. This arrangement resulted in a 50% reduction in the maximum depth of scour compared to the case of a flat floor without baffles, and a 31% reduction in the extended length of the scour. Another baffle position, at two-thirds of the floor length, only reduced the relative scour length by approximately 57%. The dimensions of the scour hole increased significantly with higher downstream Froude numbers.

Khalifehei et al. (2022) presented an experimental investigation of the impact of triangular deflectors on energy dissipation in flip buckets, which are commonly used to discharge high-velocity flow from hydraulic structures. The study conducted experiments using different hydraulic conditions and measured the energy dissipation with and without a deflector.

The results revealed that the presence of a deflector increased energy dissipation by 8.2 to 22.7 percent compared to the absence of a deflector. However, increasing the deflector angle and side length had a mixed effect, initially increasing energy dissipation but decreasing it at larger angles and lengths. The study identified an optimal deflector angle range of 27° to 32°, along with a specific deflector length to Reynolds number ratio, for achieving the highest energy dissipation. Finally, a correlation was proposed using multivariate nonlinear regression to predict energy dissipation in flip buckets with triangular deflectors.

2.6 FLOW-3D Software

The FLOW-3D model has the ability to simulate diverse boundary conditions, including flow, turbulence, bed load, and suspended sediment. This model utilizes a finite difference technique to solve 3-dimensional Navier-Stokes equations under non-hydrostatic conditions, making it well-suited for modeling free surface flow and sediment transport. Moreover, it can involve a range of sediment types and bed sediment transport models, revealing its versatility **(Xie, 2011)**.

The Flow-3D software, recommended by **(Flow Science, 2009)**, is a powerful tool for solving complex fluid dynamics problems. It is capable of modeling a wide range of flows and finds applications in simulating unsteady three-dimensional free surface flows with intricate geometries. The software utilizes three-dimensional orthogonal elements to accurately represent flow behavior. Two numerical techniques are employed for geometry simulation within the software. Firstly, the volume of fluid (VOF) method is used for modeling free surface flows, enabling the accurate depiction of fluid interfaces. Secondly, the fraction of volume or barrier (FOVOR) method is employed when simulating rigid surfaces and volumes, such as geometric boundaries. These techniques make Flow-3D a versatile software for addressing various fluid dynamics challenges.

Numerical modeling of morphology, scouring, and sediment transport has a significant predictive value in various applications within river and reservoir engineering, as evidenced by numerous studies **(Pu and Lim, 2014, Pu et al., 2014, Pu et al., 2016)**. For example, the FLOW-3D model utilizes an advection-diffusion mechanism to forecast sediment transport, which encompasses sediment suspension, settling, entrainment, and bed load **(Wei et al., 2014)**.

CFD numerical modeling is an extremely effective method for calculating the characteristics of the flow's hydrodynamics and turbulence **(Duan and Nanda, 2006, Acharya and Duan, 2011, Ghaderi et al., 2020, Pu, 2015)**. In recent years, several software programs, both commercial and non-commercial, such as SSIIM 2.0, FLOW-3D, and Fluent, have been widely studied to solve engineering problems with oceans and rivers. As an example, the flow as well as hydraulic jumps occurring in energy dissipation structures and spillways have been successfully replicated by the FLOW-3D commercial software CFD code **(Bayon et al., 2016, Ho and Riddette, 2010, Sarfaraz and Attari, 2011)**, which is commonly used in hydraulic engineering. According to **Nasralla (2022)**, the Flow 3D program can be used to simulate the scour phenomenon. He studied the impact of the stepped spillway's contraction ratio on the maximum local scour depth downstream of the free hydraulic jump within the stepped spillway's stilling basin. It was found that, the simulated results and the measured data were in agreement.

This study combines both laboratory experiments and Computational Fluid Dynamics (CFD) simulations to provide a comprehensive analysis of the behavior of flow deflectors in various conditions. The research provides an understanding of the performance of flow deflectors and the factors that affect their efficiency in terms of scour depth and energy dissipation, which can help improve their design and enhance their functionality in real-world applications.

2.6.1 Governing Equations

2.6.1.1 Model for Fluid Dynamics

The continuity equation and momentum equation, which are known as the three-dimensional Navier-Stokes equations, are governed the research problem **(Pourshahbaz et al., 2022)**:

$$\frac{\partial}{\partial x}(uA_x)+\frac{\partial}{\partial x}\left(vA_y\right)+\frac{\partial}{\partial x}(wA_z)=0 \qquad (2.1)$$

$$\frac{\partial U_i}{\partial t}(uA_x)+\frac{1}{V_F}\left(U_iA_i\frac{\partial U_i}{\partial x_j}\right)=-\frac{1}{\rho}\frac{\partial P'}{dx_i}+g_i+f_I \qquad (2.2)$$

Where u, v, and w are velocity components in the x,y, and z directions, V_F is the volume fraction of fluid in each cell, A_x, A_y, and A_z are fractional areas open to flow in the subscripts direction, P′ is hydrostatic pressure, g_i is gravitational acceleration in the subscripts direction, and fi represents Reynolds stress, which the turbulence model requires for closure. In the model, A_j is equal to one in computational cells that are filled with fluid V_F. As a result, the equations are reduced to one-fluid, incompressible Reynolds-averaged Navier-Stokes (RANS) form.

2.6.1.2 Turbulence Modeling

One of the five turbulence models used by the program is used to simulate turbulence in FLOW-3D. FLOW-3D employs the following turbulence models: One Equation, Prandtl Mixing Length. Two Equation Model (k-ε), Large Eddy Simulation Model, Renormalized Group (RNG) model.

The most widely used of these models is the two-equation turbulence model, which uses two transport formulas for turbulent viscosity-related variables and can accurately describe turbulence on both a scale of time and space **(Pope, 2001)**. The RNG k-ε model is better at simulating flows with strong shear effects because it uses statistical techniques to derive averaged equations for the turbulence quantities used in the k-ε model **(Dong et al., 2019)**.

Furthermore, this turbulence model has been successfully used in the numerical modeling of hydraulic structures in recent years **(Li and Zhang, 2018, Zhang et al., 2018)**. As a result, this turbulence model was chosen for the current work. The transport of turbulent kinetic energy and its dissipation rate in the RNG k- model are modeled by the following equations **(Pourshahbaz et al., 2022)** :

$$\frac{\partial}{\partial t}(\rho k)+\frac{\partial}{\partial x_i}(\rho k u_i)=\frac{\partial}{\partial x_i}\left[\left(\mu+\frac{\mu_t}{\sigma_k}\right)\frac{\partial k}{\partial x_i}\right]+P_k-\rho\varepsilon \qquad (2.3)$$

$$\frac{\partial}{\partial t}(\rho\varepsilon)+\frac{\partial}{\partial x_i}(\rho\varepsilon u_i)=\frac{\partial}{\partial x_i}\left[\left(\mu+\frac{\mu_t}{\sigma_\varepsilon}\right)\frac{\partial\varepsilon}{\partial x_i}\right]+C_{1\varepsilon}\frac{\varepsilon}{k}P_k-C_{2\varepsilon}^{*}\rho_f\frac{\varepsilon^2}{k} \qquad (2.4a)$$

Where x_i denotes a coordinate along the i-axis, μ stands for dynamic viscosity, μ_t for turbulent dynamic viscosity, and P_k for the creation of turbulent kinetic energy. Last but not least, **Yakhot et al. (1992)** provides the values for the parameters as following: $\sigma_k=\sigma_\varepsilon=0.7149$, $C_{1\varepsilon}=1.42$.

$$C_{2\varepsilon}^{*}=C_{2\varepsilon}+\frac{C_\mu\eta^3(1-\eta/\eta_0)}{1+\beta\eta^3}, \qquad (2.4b)$$

$\beta = 0.012$, $C_\mu=0.0845$, $\eta_0=4.38$, $C_{2\varepsilon}=1.68$.

$$\eta=\frac{sk}{\varepsilon} \qquad (2.4c)$$

$$S=(2S_{ij}S_{ij})^{0.5} \qquad (2.4d)$$

$$S_{ij}=\frac{1}{2}\left(\frac{\partial U_i}{\partial x_j}+\frac{\partial U_j}{\partial x_i}\right) \qquad (2.4e)$$

2.6.1.3 Bed material Model

Bed-load transport is a method of transporting sediment by when moves along a packed bed surface, it can either roll or bounce. To determine the sediment's volumetric transport rate per unit width of the bed, three equations can be applied:

(1) Meyer, Peter and Müller (1948):

$$\Phi_i = \beta_{MBM,i}(\theta_i - \theta'_{cr,i})^{1.5} c_{b,i} \tag{2.5}$$

(2) Nielsen (1992):

$$\Phi_i = \beta_{Nie,i}\theta^{0.5}\left(\theta_i - \theta'_{cr,i}\right)c_{b,i} \tag{2.6}$$

(3) Van Rijn (1984):

$$\Phi_i = \beta_{VR,i} d_*^{-0.3}\left(\frac{\theta_i}{\theta'_{cr,i}} - 1\right)^{2.1} \tag{2.7}$$

In which;

$$\theta_i = \frac{\tau}{\| g \| \, d_i(\rho_i - \rho_f)} \tag{2.8}$$

$$q_{b,i} = \Phi_i \left[\|g\| \left(\frac{\rho_i - \rho_f}{\rho_f}\right) d_i^{3}\right]^{0.5} \tag{2.9}$$

$$\theta'_{cr,i} = \frac{0.3}{1 + 1.2d_{*,i}} + 0.055\left[1 - \exp\left(-0.02d_{*,i}\right)\right] \tag{2.10}$$

$$D_{*,i} = d_i \left[\| g \| \, \frac{\rho_f(\rho_i - \rho_f)}{\mu_f^2} d_i\right]^{\frac{1}{3}} \tag{2.11}$$

Where $\beta_{MPM,i}$, $\beta_{Nie,i}$, and $\beta_{VR,i}$ the coefficients usually take on values of 8.0, 12.0, and 0.053. In equations (2.5-2.7), an additional term, $c_{b,i}$, is included to consider the impact of multiple species. This term represents the volume fraction of species i within the bed material, which was not originally present in the equations. In other hand, the local Shields parameter for species i in the bed material is represented by θ_i and can be determined by calculating the local bed shear stress, τ, using the formula illustrated in equation (2.8). Additionally The dimensionless bed-load transport rate, represented by Φ_i, is linked to the volumetric bedload transport rate, $q_{b,i}$, as illustrated in equation (2.9).

Furthermore, the modification of $\theta_{cr,i}$ to account for sloping surfaces is represented by $\theta'_{cr,i}$ and includes the angle of repose. The critical Shields parameter of species i in the bed material, $\theta_{cr,i}$, can be determined using the Soulsby-Whitehouse equation outlined in equation (2.10). The dimensionless parameter $d_{*,i}$ required to calculate $\theta_{cr,i}$ can be computed using equation equation (2.11), which involves the sediment species i's density (ρ_i), diameter (d_i), fluid density (ρ_f), dynamic viscosity of the fluid (μ_f), and magnitude of the acceleration of gravity (g).

Numerous studies have demonstrated the superiority of the Meyer-Peter and Müller formula over other formulas in three-dimensional numerical models of scour, particularly regarding the shape and extent of the scour hole and the time it takes for scouring to occur **(Flow Science, 2009)**. As such, it is a reliable method for investigating these issues. As a result, equation (2.5) was used in this study to calculate bed-load transport.

2.7 Summary

The literature review survey indicates the following remarks:

1) Scouring is a complex phenomenon, and modeling it poses a significant challenge. As a result, researchers need to develop techniques and improve their skills to achieve a comprehensive understanding of this phenomenon and accurately assess its effects.
2) Scour depth prediction due to flow deflectors has not been enough addressed in the existing literature. Therefore, the present study emphasizes the need for investigation and the potential for insights and contributions to the field.
3) The proposed various relationships for scour depth for two geometric shapes of flow deflectors (semi-circular and triangular) with four cases (single perforated semi-circular and triangular) and (double solid semi-circular and triangular) will be investigated.
4) An optimization-based solution for the objective function of minimum scour depth for the different flow deflectors and cases will be formulated and solved. Validation for the optimization results will be carried out to ensure they are accurate and reliable.

Chapter Three

Experimental and Simulation Work

3.1 General

Flow deflectors and stilling basins are vital elements in hydraulic engineering. Flow deflectors help redirect the flow of water, while stilling basins slow down and dissipate the energy of flowing water. To reduce local scour around structures, engineers conduct experiments. They test various designs and configurations to find the most effective and cost-efficient solutions. These experiments help ensure the safety and longevity of hydraulic structures.

The scope of this research refers to its defined parameters and the extent to which it investigates the hydraulic flow deflectors in terms of energy dissipation and developed scour depth. The limitations of the research refer to the factors that may constrain the research, as they define what the study cannot accomplish or address.

3.2 Factors and Variables Influencing the Research Problem

This research will utilize several basic variables to determine the maximum local scour depth, including the type of flow deflector (such as single perforated triangular, double solid triangular, single perforated semi-circular, and double solid semi-circular), flow velocity, and position of the flow deflector across the direction of flow. The detailed explanation of these variables will be provided subsequently.

3.2.1 Definition of Basic Parameters and Variables

i- The various types of flow deflectors include a single perforated triangular, double solid triangular, single perforated semi-circular, and double solid semi-circular.

ii- Relative position of the flow deflector, that is denoted by ($L_0 = \frac{L}{L_B}$) as shown in Figure (3.1),

iii- For a triangular deflector, the apex angle is considered, while for a semicircular deflector, the oriented angle is taken into account, which was denoted by (θ) as shown in Figure (3.1),

iv- The proportion of the waterway passages, as denoted ($\alpha_0 = \frac{a_{opening}}{A_t}$) as shown in Figure (3.1), where A_t is the total solid area of any type of deflector. The center of the opening aligns with the midpoint of each quarter of either the single semi-circular or triangular deflector.

v- Flow regime type can have a significant impact on scour depth, such as the velocity, depth, and discharge of the water. The considered factor is expressed in terms of Froude Number ($Fr_1 = \frac{V_1}{\sqrt{g\,y_1}}$) as shown in Figure (3.1),

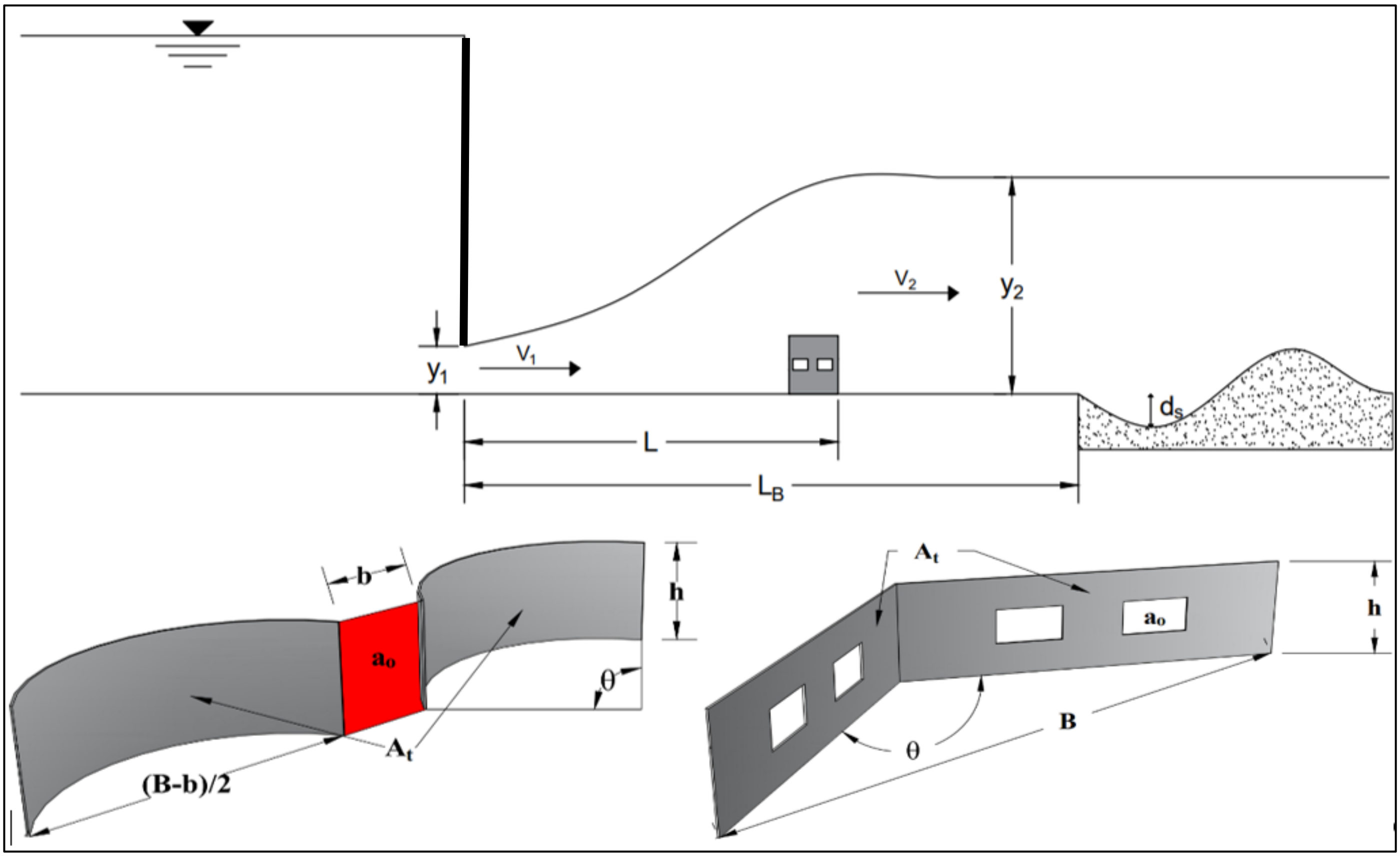

Figure (3.1): Definition sketch for the experimental and numerical model.

The experimental tests were carried out by preparing and manufacturing the flow deflectors to the specified dimensions, which are determined according to the following equations. Where all dimensions and variables involved in those equations were defined in Figure (3.2).

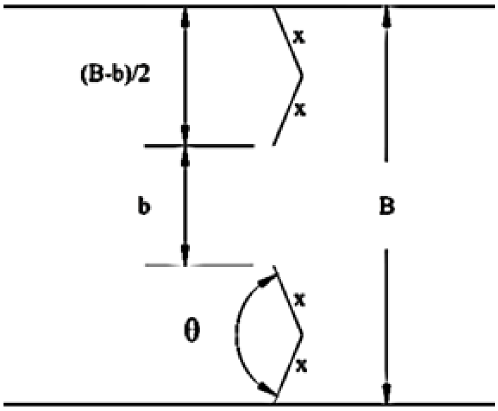

(a) Top view of double solid triangular flow deflector.

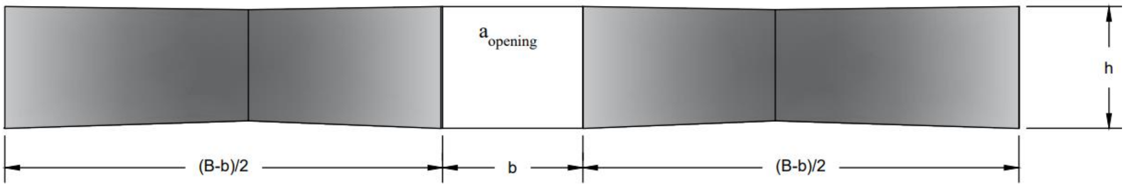

(b) Front view of double solid triangular flow deflector.

Figure (3.2): Schematic representation for the flow deflector of double solid triangular shape.

Where, x is the Length of one side of the triangular deflector.

From;

$$\left(\frac{B\text{-}b}{2}\right)=\sqrt{2}x\sqrt{1\text{-}\cos(\theta)} \qquad (3.\ 1a)$$

$$\because B=1 \qquad (3.\ 1b)$$

$$\therefore b=1\text{-}2\sqrt{2}x\sqrt{1\text{-}\cos(\theta)} \qquad (3.1c)$$

Since;

$$\alpha_0=\frac{a_{opening}}{S_{DT}} \qquad (3.\ 2a)$$

Or;

$$\alpha_0=\frac{h\ b}{h\ (4x)}=\frac{0.2\ b}{0.2(4x)}=\frac{b}{4x} \qquad (3.\ 2b)$$

Thus;

$$b=4\alpha_0 x \qquad (3.\ 2c)$$

$$4\alpha_o x=1\text{-}2\sqrt{2}x\sqrt{1\text{-}\cos(\theta)} \qquad (3.\ 3a)$$

Or;

$$x=\frac{1}{4\alpha_o+2\sqrt{2}\sqrt{1-\cos(\theta)}} \qquad (3.\ 3b)$$

Similarly, for the double solid semi-circular flow deflector shape, the following equations were used to determine the deflector dimensions. In Figure (3.3), all the dimensions and variables required in the equations were specified.

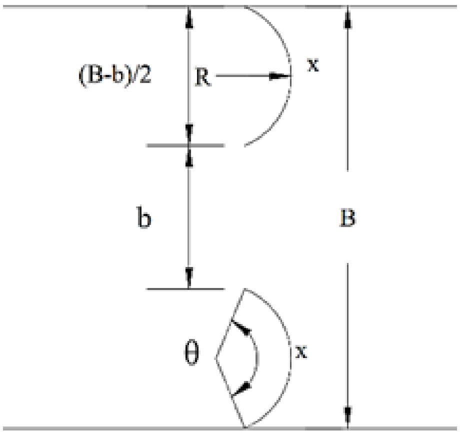

(a) Top view of double solid semi-circular flow deflector.

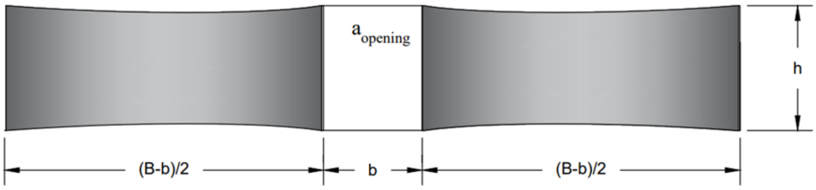

(b) Front view of double solid semi-circular flow deflector.

Figure (3.3): Schematic representation for the flow deflector of double solid semi-circular flow deflector.

Where, x is the length of perimeter of the semi-circular deflector.

From;

$$\left(\frac{B-b}{2}\right)=2R\sin\left(\frac{\theta}{2}\right) \qquad (3.\ 2a)$$

and;

$$R=\frac{x}{\theta} \qquad (3.\ 4b)$$

From;

$$\therefore\left(\frac{B-b}{2}\right)=2\frac{x}{\theta}\sin\left(\frac{\theta}{2}\right) \qquad (3.4c)$$

Since;

$$B=1 \tag{3. 4d}$$

Thus;

$$b=1-4\frac{x}{\theta}\sin\left(\frac{\theta}{2}\right) \tag{3.4e}$$

Since;

$$\alpha_0=\frac{a_{opening}}{S_{DT}} \tag{3.5a}$$

$$\alpha_o=\frac{h\ b}{h\ (2x)}=\frac{0.2b}{0.2(2x)}=\frac{b}{2x} \tag{3.5b}$$

$$\therefore\ b=2\alpha_0 x \tag{3.5c}$$

Or;

$$2\alpha_o x=1-4\frac{x}{\theta}\sin\left(\frac{\theta}{2}\right) \tag{3.6a}$$

$$\therefore\ x=\frac{1}{2\alpha_o+\frac{4}{\theta}\sin\left(\frac{\theta}{2}\right)} \tag{3.6b}$$

Detailed equations for determining the dimensions and shapes that were used in laboratory experiments for the remaining types of flow deflectors were provides in the appendix [A].

3.2.2 Reconnaissance of Hydraulic Structures along the Euphrates Reach

In order to determine the flow characteristics and median sediment particles of the movable bed, the Euphrates River and its flow characteristics will be analyzed, and the downstream movable bed's sediment size and the barrages and regulators on the Euphrates River will be studied to predict reliable ranges of parameters and variables involved in this study.

The most important river in southwest Asia with regards to length, catchment area, and historical significance is the Euphrates River. It is also the second-largest river in terms of volume. The majority of the Euphrates' water resources are located in Turkish Anatolia. The river stretches for 1160 kilometers through Iraq, starting from Hussaybah on the Syrian-Iraqi border until it meets with the Tigris River. While the primary basin of the Euphrates River is distributed among three countries, namely Iraq (47%), Turkey (28%), and Syria (22%), there are smaller portions in Jordan (0.03%) and

Saudi Arabia (2.97%) **(Al-Ansari et al., 2019).** Figure (3.4) illustrates that the upper course of the Euphrates River has a significant difference in elevation, which results in its rapid flow.

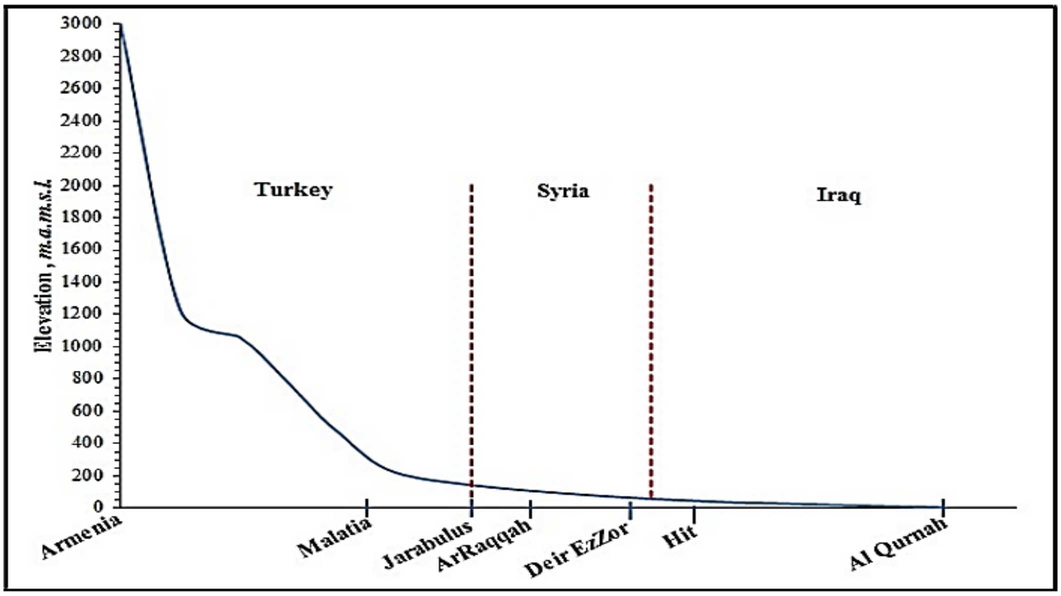

Figure (3.4): The longitudinal section along Euphrates River **(Al-thamiry et al., 2013)**.

According to Figure (3.5), the Euphrates River shows a predictable pattern on a yearly basis, with a peak discharge occurring during two consecutive months, specifically April and May. These two months account for approximately 42% of the river's total yearly flow. However, eight dry months occur between July and February, so the river's flow is reduced to reach the minimum values after June between September and October **(Bomola, 2011).**

The construction of barrages is an important part of Iraq's modern water resource infrastructure, with the main purpose of raising water levels to provide irrigation and diversion during floods. Some barrages are functioning well, while others, especially those in the lower Euphrates, have technical issues. The Hindiyah Barrage was constructed due to water scarcity in the Hilla branch, followed by additional barrages recommended by William Willcocks in 1911. Barrages were constructed after the 1950s, and the most significant ones are displayed in Figure (3.6).

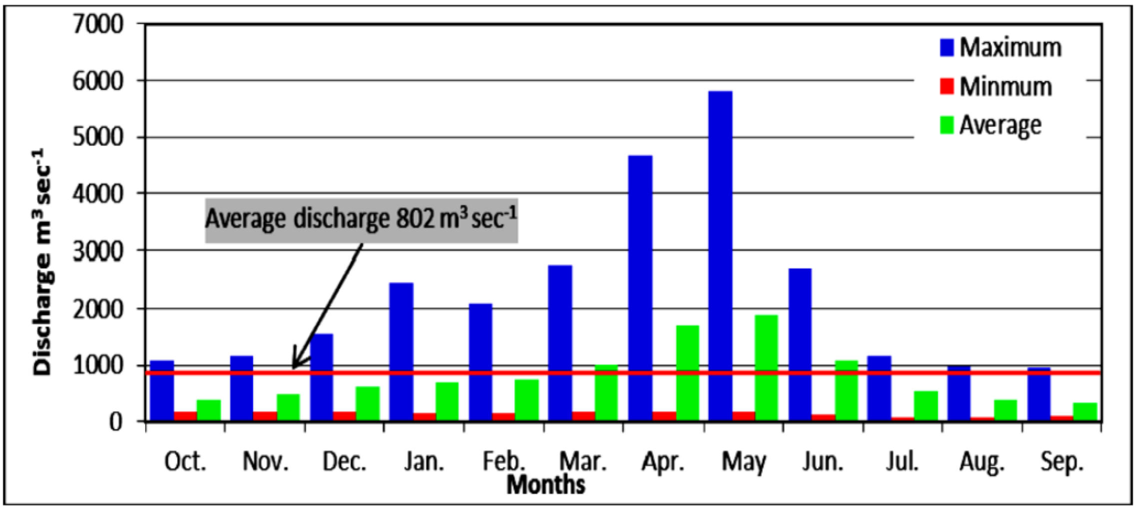

Figure (3.5): Monthly discharge of the Euphrates River (mean, maximum, and minimum) at the Hit site (1932-1997), **(Issa et al., 2014)**.

Tables 3.2 and 3.3 provide a summary of information regarding the primary barrages and regulators located on the Euphrates River. The data in the table is collected from various studies conducted by different researchers.

Based on the data presented in Tables (3.1) and (3.2), it is evident that the Froude number varies between 0.26 and 3.39, while the sediment grain size ranges from 0.015 to 4 mm. As a result, we can infer that the Froude number range for this study falls between 0.26 to 3.39, and the sediment grain size range falls between 0.015 to 4 mm.

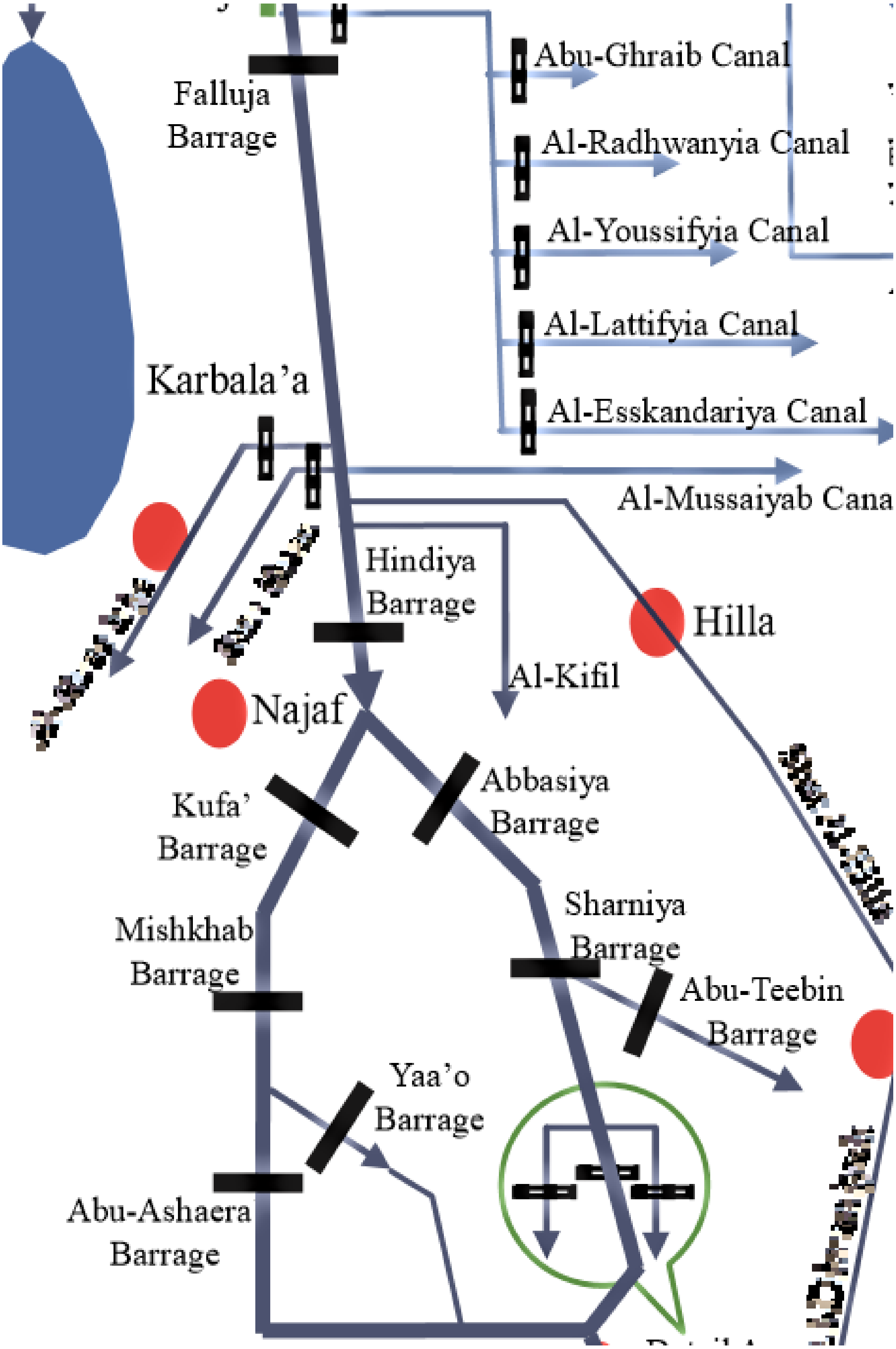

Figure (3.6): Main Control Structures Schematic Diagram along the part of Euphrates River **(JICA, 2016).**

Table (3.1): Characteristics of hydraulic structures on Euphrates River (Quoted from references)

The hydraulic structure				Ramadi Barrage	Falluja Barrage	Hindiya Barrage	Shamiya Branch regulators (40%)			Kufa Branch Barrages (60%)		
					Main	Main	Abbasiyah Regulator	Shamiya Regulator	Khawarnaq Regulator	Kufa Barrage	Abu-Sukhayr Barrage	Meshkhab Barrage
Opened	**year**			1956	1985	1911 (1989)*	1986	1986	1986	1986	2019	1959
Characteristics of gate	**Type of Gate**			vertical Gate	Radial Gate	Radial Gate	Radial Gate	Radial Gate	Radial Gate	Radial Gate	Radial Gate	vertical Gate
	Number of gates			24	10	6	6	6	5	7	7	7
	Dimensions of Gate	**Height**	**(m)**	6	8.5	6.75	6.3	6.3	8	6.3	6.5	7
		Width	**(m)**	8	16	16	12	12	8	12	12	13.5
Design discharge		**Q(design)**	**(m^3/s)**	3600	3600	2500	1100	1100	1100	1400	1400	1400
Design elevation	**Up stream**	**Elev. (design.u/s)**	**(m.a.s.l)**	51.5	44.79	32.55	------	22.5	------	25.7	------	------
	Down stream	**Elev. (design.d/s)**	**(m.a.s.l)**	------	------	25.4	23.8	19.5	------		------	25.7
Maximum discharge		**Q(max.)**	**(m^3/s)**	1279	634	2400	250	------	------	300	------	230
maximum elevation	**Up stream**	**Elev. (max.u/s)**	**(m.a.s.l)**	------	42.86	------	------	21	------	24.5	20	------
	Down stream	**Elev. (max.d/s)**	**(m.a.s.l)**	------	42.1	28	------	18	------	22.6	18	24.5

Table (3.1): Characteristics of hydraulic structures on Euphrates River (Quoted from references, continued).

The hydraulic structure				Ramadi Barrage	Falluja Barrage	Hindiya Barrage	Shamiya Branch regulators (40%)			Kufa Branch Barrages (60%)		
					Main	Main	Abbasiyah Regulator	Shamiya Regulator	Khawarnaq Regulator	Kufa Barrage	Abu-Sukhayr Barrage	Meshkhab Barrage
Normal discharge		**Q(normal)**	**(m^3/s)**	550	410	545	55	200	------	110	------	95.6
Normal elevation	**Up stream**	**Elev. (normal.u/s)**	**(m.a.s.l)**	------	42.65	31.9	------	------	------	23.5	------	------
	Down stream	**Elev. (normal.d/s)**	**(m.a.s.l)**	------	41	26.5	23.5	------	------	22	------	24.5
Minimum inflow		**Q(min.)**	**(m^3/s)**	237.94	268	200	50	50	------	50	------	50
minimum elevation	**Up stream**	**Elev. (max.u/s)**	**(m.a.s.l)**	------	42.6	------	------	------	------	23.35	18.8	------
	Down stream	**Elev. (min.d/s)**	**(m.a.s.l)**	------	40.4	25.95	------	------	------	21.6	17	18.8
Bed material characteristics	**specific gravity**	**Gs**	------	2.60–2.70	2.65	2.66	2.67	2.62	------	2.73	------	------
	median sediment size	**D_{50}**	**(mm)**	(0.09-0.15)	4	0.015	0.125	0.22	------	0.3	------	------

Table (3.2): Froude Number for flow through hydraulic structures.

The hydraulic structure		Ramadi Barrage	Falluja Barrage	Hindiya Barrage	Shamiya Branch Regulators (40%)			Kufa Branch Barrages (60%)		
			Main	Main	Abbasiyah Regulator	Shamiya Regulator	Khawarnaq Regulator	Kufa Barrage	Abu-Sukhayr Barrage	Meshkhab Barrage
n		24	10	6	6	6	5	7	7	7
B_g (m)		8	16	16	12	12	8	12	12	13.5
Q_{design} (m^3/s)		3600	3600	2500	1100	1200	1100	1400	1400	1400
$y_{1(max.)}$ (m)	**full opening of gate**	6	8.5	6.75	6.3	6.3	8	6.3	6.5	7
Fr_{1a}	**For Q_{design} and $y_{1(max.)}$**	0.41	0.29	0.47	0.31	0.34	0.39	0.34	0.32	0.26
$Q_{minimum}$		237.94	268	200	50	50	------	50	------	50
$y_{1(min.)}$ (m)	**assume 5% of full opening of gate**	0.3	0.425	0.3375	0.315	0.315	0.4	0.315	0.325	0.35
Fr_{1b}	**For Q_{min} and $y_{1(min.)}$**	2.41	2.06	3.39	1.25	1.25	------	1.07	------	0.82

Where;

Fr_1=Froude number at opening gate.

y_1=high of opening gate.

B_g=Width of opening gate.

n=Number of opening gates.

Q=Discharge of the hydraulic structure

$g=9.81\ m/sec^2$

3.2.3 Upper and Lower Range for Variables

During this study, a range of variables was being investigated as shown in Table (3.3). These variables were carefully examined to better understand their impact on scour depth in hydraulic engineering applications.

Table (3.3): The range of variables that will be used in this study.

The parameter	**Range of the parameter**	**According to**
L_0	**(25% –75%)**	**1)EL-masry and Sarhan (2000)** **2)Negm (2004)** **3)Abdelhaleem (2013)**
θ	**(45^o – 135^o)**	**1) EL-masry and Sarhan (2000)** **2) Biron et al. (2005)** **3) Ashour et al. (2016)**
α_0	**(10% – 40%)**	**1) Negm et al. (2009a)**
Fr_1	**(0. 26 – 3.39)**	**From Table (3.2)**
D_{50}	**(0.015 – 4) mm**	**From Table (3.1)**

3.3 Experimental Work

The experimental work has been conducted in the hydraulic laboratory in the water resources and structures, college of engineering, University of Kufa, Iraq as shown in Figures (3.7–3.10). The channel comprises the following components:

1. The experimental channel utilized in this study had specific dimensions, measuring 18 meters in length, 1.0 meter in width, and 1.1 meters in depth. Additionally, a head basin was incorporated, with dimensions of 2 meters in length, 3.6 meters in width, and 1.1 meters in depth.
2. The experimental setup included a lateral basin with specific dimensions of 19 meters in length, 1.5 meters in width, and 0.6 meters in depth.

3. In the experimental setup, a vertical sluice gate head measures 2 meters in depth and 1.0 meter in width. Moreover, there is a vertical sluice tailgate at the end of the flume, which is 1 meter wide and 1.25 meters deep.
4. In order to reduce the flow turbulence, the experimental setup uses 1meter deep and 1 meter wide stilling screens. The main water pump in the system has a power of 30 horsepower and a discharge rate of 70 liters per second. The depths of the scour hole and the water's surface are measured using a point gauge.
5. To facilitate of movement of the point gauge along the channel walls, two rails have been fitted onto the side walls of the flume.
6. A steel frame is being used to secure the weir structure, which will aid in measuring the discharge. In addition, a two-horsepower pump is connected to the water supply source on the side of the lateral basin.
7. The scour hole locations can be identified by using a BRC mesh with 5 cm c/c spacing. There is a bed material collection basket in the setup that measures 1 meter in length, 1 meter in width, and 0.5 meters in depth.
8. An outlet valve with a pipe of 10 cm diameter is used to maintain a constant water level in the head basin. Additionally, a similar pipe with a valve of 10 cm diameter has been installed at the lower end of the lateral basin for cleaning and drainage purposes.

The following steps outline the operation of the channel system both prior to and during the experimental work:

1. The water supplied and transported to the lateral basin by pumping, the main basin obtains water from the lateral basin through the main pump.
2. The channel is supplied with water by raising the main gate, allowing water to flow through it. In order to dissipate the energy of the water flow, three screens are placed 2.0 meters after the main gate.
3. Throughout the test program, water is returned to the lateral basin by the tailgate, which is positioned at the end of the flume.

4. Prior to the movable bed represented by sand layer, deflector models were attached to the flume's sidewall as shown in Figure (3.8).
5. A sticky rubber was used to prevent water leakage from the model's sides.

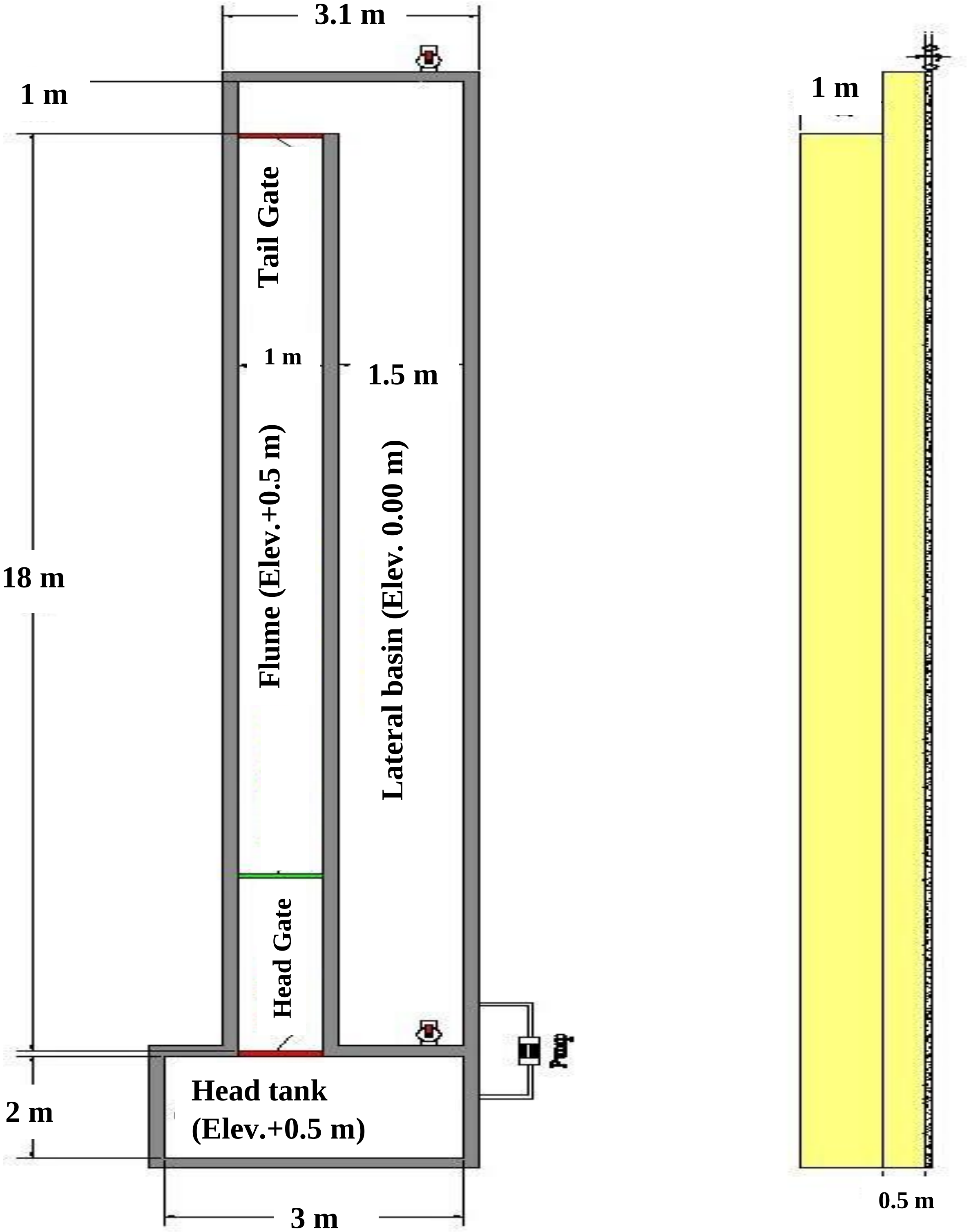

Figure (3.7): Schematic representation for channel system

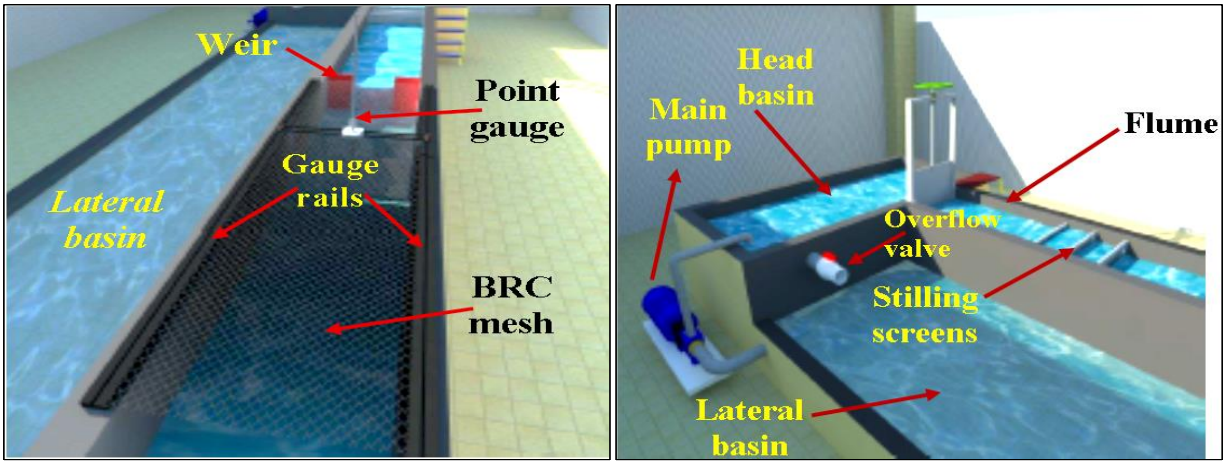

(a): Top view. (b): Front view.

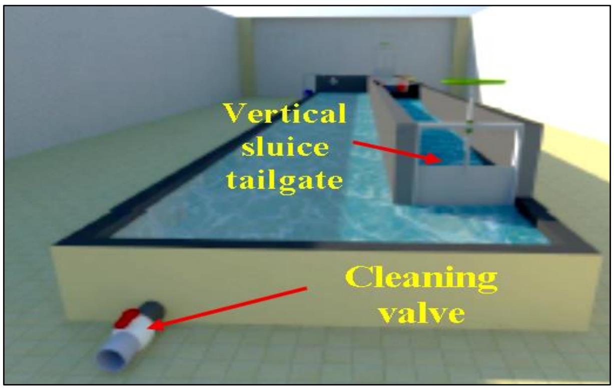

(c): Side view.

Figure (3.8): Schematic Representation of the experiment flume.

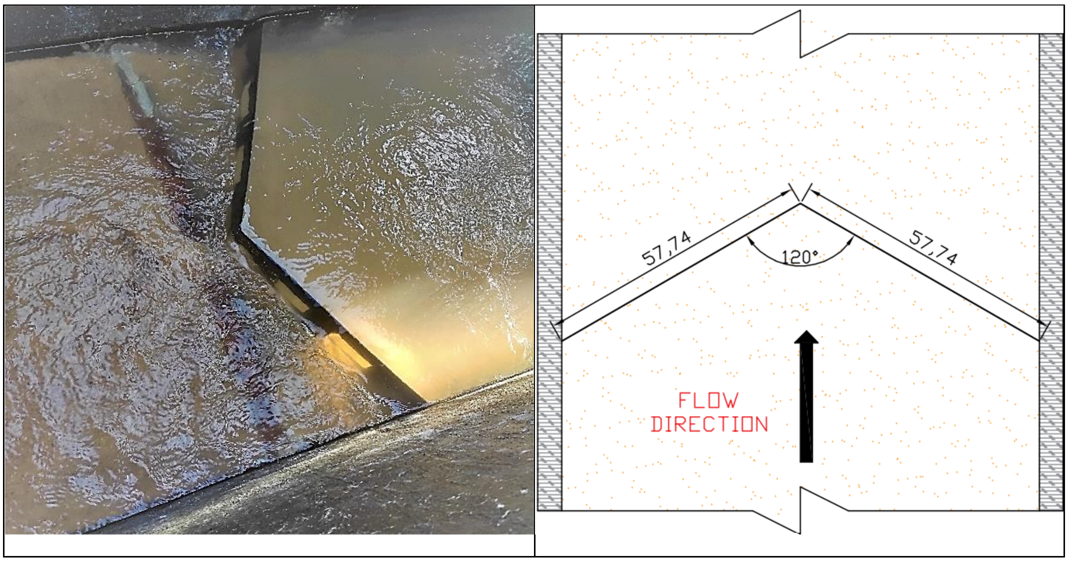

Figure (3.9): Fixing the deflector to the flume.

3.3.1 Calibrating Process of the Flume

To determine the required discharge, the head can be measured by using a partially contracted 90-degree triangular weir positioned at a distance of 7 meters from the head of the vertical sluice gate. This particular weir design is constructed in accordance with the specified limits governing the utilization of partially contracted triangular weirs, as depicted in Figure (3.9) and recommended by the **(USBR, 1997)**. These limits include the following requirements:

1. Ensuring that the ratio of head (h) over the distance (h_t) between the apex of the triangular weir and the flume bed is not greater than 1.2.
2. Maintaining a ratio of head (h) over the width (B) of the flume that does not exceed 0.4, applicable when the head (h) is less than or equal to 60.96 cm.
3. Ensuring that the distance (h_t) between the apex of the triangular weir and the flume bed is greater than or equal to 10.16 cm.
4. Ensuring that the width (B) of the flume is equal to or greater than 60.96 cm.
5. Maintaining the thickness (t) of the triangular weir within the range of 1-2 mm. These specifications and limitations contribute to the accurate determination of discharge through the triangular weir.

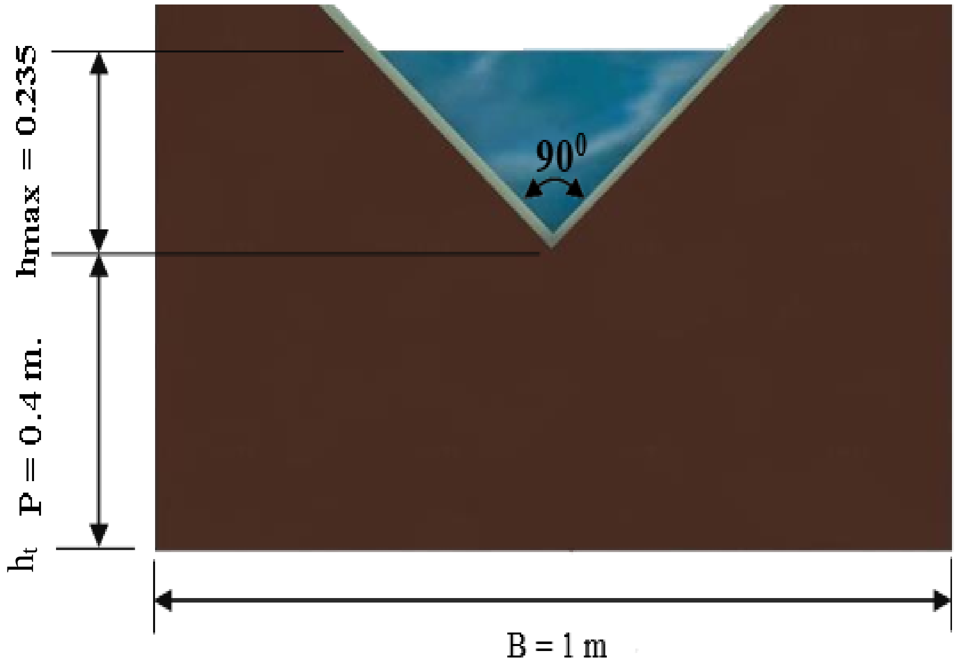

Figure (3.10):The dimensions of the standard calibration weir.

USBR (1997) suggested that if the crest edge thickness is greater than 2 mm, then by chamfering the crest's downstream edge by at least a 45° angle, the crest's edge thickness must be minimized to the desired thickness, which is between 1 mm and 2 mm.

To obtain accurate discharge values, the calibration process involves utilizing a tank with known volume to measure the accumulated water volume. The tank has dimensions of 1 meter in length, 1.6 meters in width, and 0.6 meters in height. To measure the time, a stopwatch is employed. This calibration technique is known as the volumetric method, which ensures precise measurements. For calibration purposes, seven distinct discharge values were utilized. Figure (3.11) visually illustrates the correlation between the water height (h) over the edge of the standard weir and the corresponding actual discharge values. This graphical representation provides valuable insights into the relationship between water height and discharge, aiding in accurate discharge determination during the experiment.

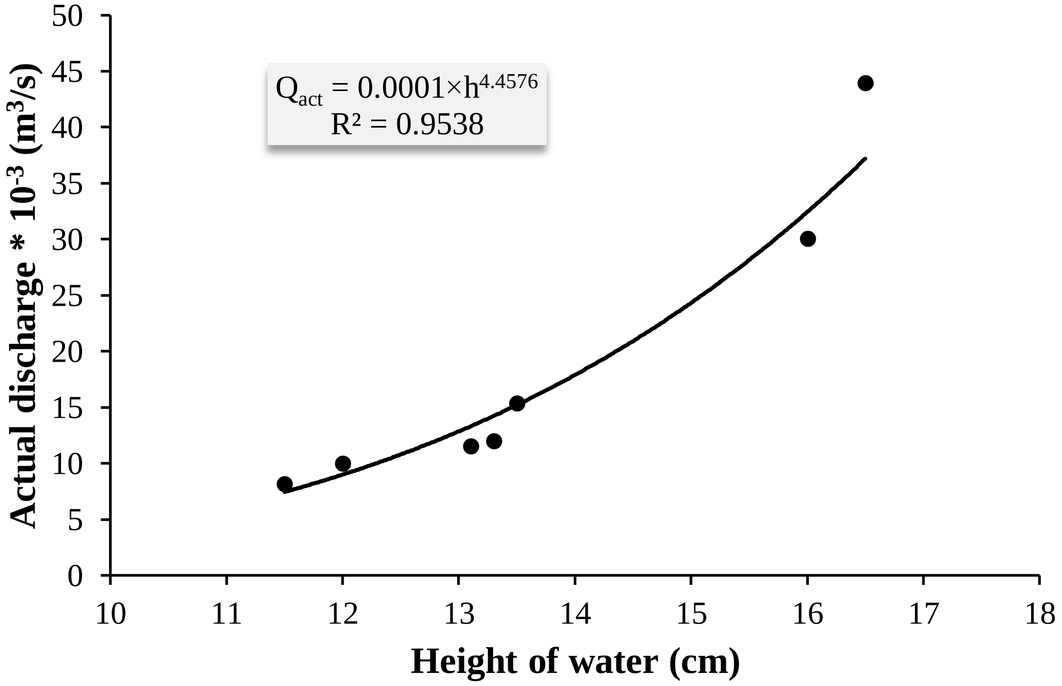

Figure (3.11):Actual discharge and the water height over the lower edge of the compound calibration weir.

3.3.2 Flow Deflector Models

A total of fifteen tests were conducted to study the effect of flow deflectors on bed form and local scour. Among these, three runs were performed without any flow deflectors, while the remaining twelve tests were specifically designed to investigate the impact of different types of deflectors on the form of local scour. The duration of each test was three hours, which was sufficient to achieve an equilibrium depth of the local scour. Table (3.4) presents a summary of the flow conditions, geometry characteristics, and configurations for the various flow deflectors. Additionally, Figure (3.12) provides a general definition sketch for the different deflector models.

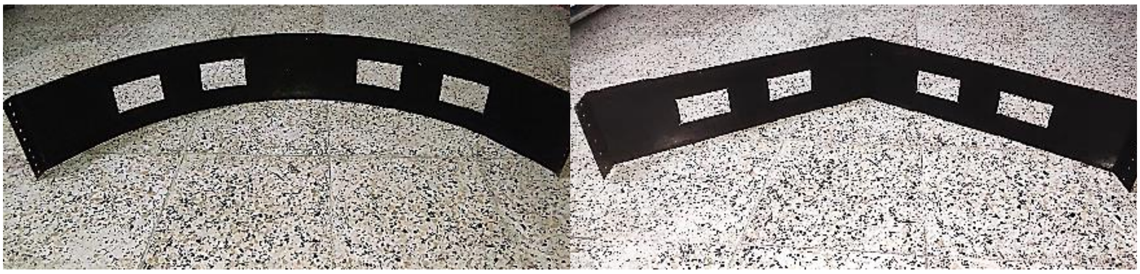

(a) Perforated single semicircular Flow deflector

(b) Perforated single triangular Flow deflector

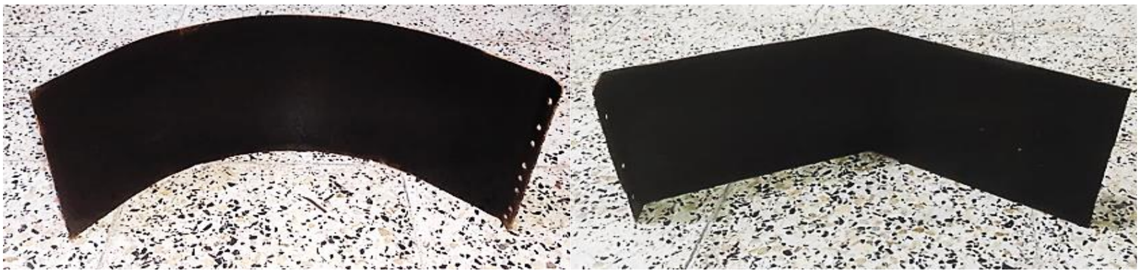

(c) Solid semicircular Flow deflector

(d) Solid triangular Flow deflector

Figure (3.12):Different types of investigated flow deflectors.

Table (3. 4): Summary of configurations for flow deflectors investigated in experimental study.

	Perforated Single		**Solid Double**	
Shape / **Parameter**	**Triangular**	**Semi-circle**	**Triangular**	**Semi-circle**
θ	120°	120°	120°	120°
A_t (cm^2)	1963.16	2055.64	1688.44	1764.26
$a_{opining}$ (cm^2)	240	240	238	238
b (cm)	0	0	14	14
h (cm)	17	17	17	17
α_o	14%	14%	14%	14%
L_0	90%	90%	90%	90%
Fr_1	Fr_1=0.3, Fr_1=0.52, Fr_1=0.68			

3.3.3 Calculations for the Depth and Length of the Scour Hole

The methodology for calculating the depth and length of the scour hole is as follows:

1. Spreading a 12 cm thick layer of sand with D_{50}= 1.0 mm for a distance of 4 m downstream of the flow deflector as shown in Figure (3.13a).
2. Filling both the head and lateral basins to their maximum capacity with water. After that, install the flow deflector before the sand layer as shown in Figure (3.13b).
3. Opening the main gate to an appropriate height, managed by a valve, to provide the desired actual discharge based on the pump's discharge. A certain amount of flow will pass over the weir.
4. Steady flow occurs when the upstream water level becomes constant. The measurements of water level above the sand layer are carried out by using a point gauge.
5. The run is terminated when it is ensured that the hole's depth does not change due to increased water flow duration over the sand layer. The

time between the start of the experiment and the hole's arrival at a fixed form is referred to as the time of equilibrium. Thereafter, turning off the pump and close the vertical gate to prevent water from flowing from the head basin after the equilibrium time has passed.

6. Using a gauge in accordance with the BRC mesh to measure the depth of every point on the surface of the hole. When the scour hole has been drained of water, use a measuring tape to determine its depth.
7. Repeating the above steps for each flow deflector with three different discharges.

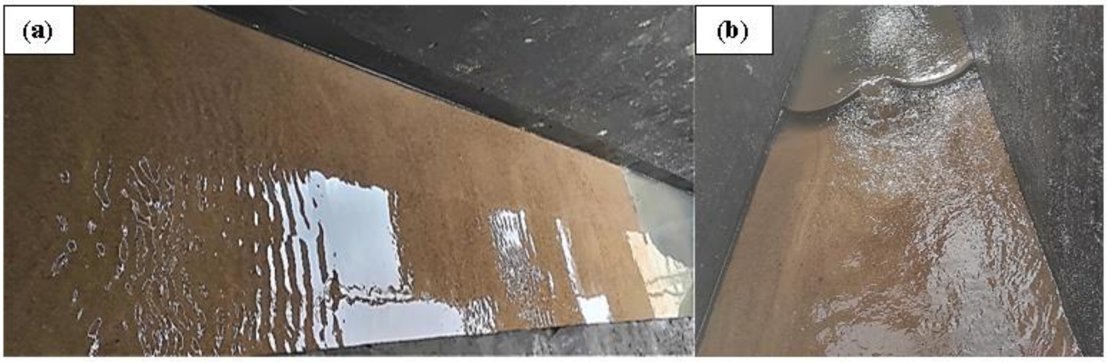

Figure (3.13): Photos for (a) Preparation of the sand layer before carrying out the experiments (b) Installation of flow deflector model during the scouring experiment.

3.3.4 Gradation of the Bed Material

In order to study the local scour downstream of the flow deflectors, a sample of sand soil was selected herein, and a dry weight sieve analysis test was conducted as per the **ASTM D422-63 (2007)**. The particles gradation curve for this test was shown in Figure (3.14).

The thickness of the sand layer is 12 cm, with a median diameter of 1.0 mm which falls within the specified range, accordingly; the values of critical shear velocity $u_{*,cr.}$were determined from Shield's chart **(Melville and Sutherland, 1988)** was 0.0233 m/sec. In this study, the tests were conducted for velocity lower than the initiation of motion of bed material undertaken. The critical velocities for the inception of bed movement were obtained based on the logarithmic velocity profile. The depth of flow corresponding to the investigated discharges and the relevant approach velocities as well as the hydraulic characteristics for the flow regime were shown in Table (3.5).

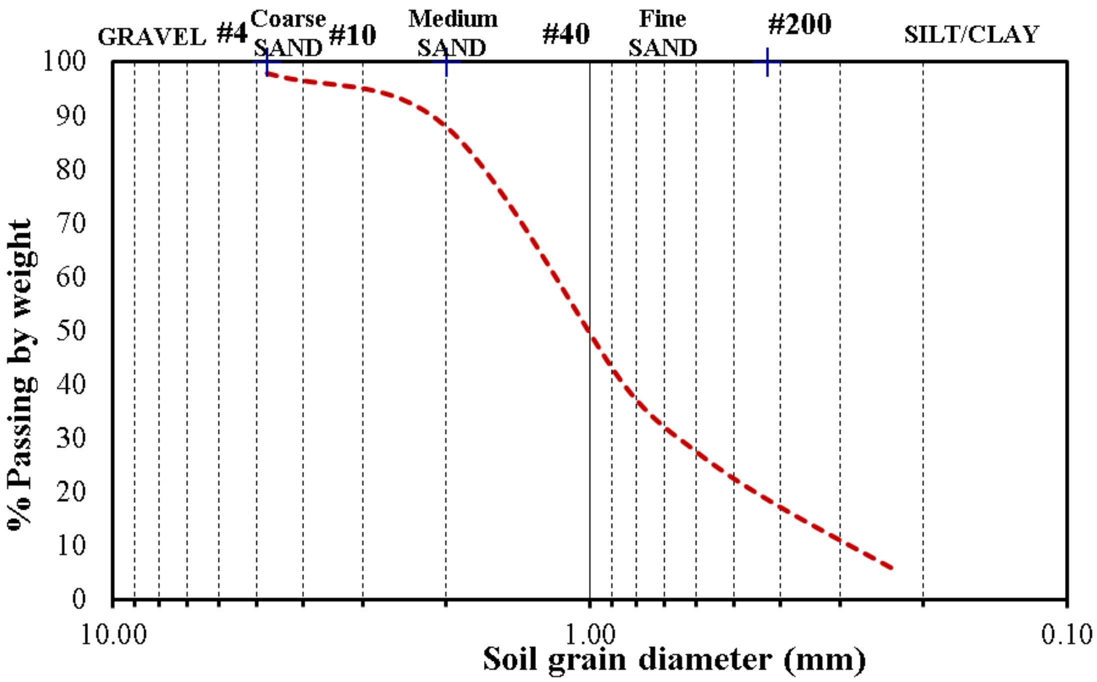

Figure (3.14):Particles gradation curve for the channel bed materials.

Where; $\rho_s = 2650 \frac{Kg}{m^3}, \ \varphi = 32°$

Table (3.5): Hydraulic characteristics for the flow regime.

Discharge (m^3/s)	**Depth of flow*10^{-2}(m)**	**Approach velocity, V_a (m/sec)**	**Critical velocity*, V_c (m/sec)**	**V_a/V_c**	**Flow regime**
0.0154	18.5	0.083	0.167	0.495 <1	Clear water scour
0.0331	19.0	0.174	0.169	1.031 >1	Live bed scour
0.044	19.5	0.226	0.171	1.322 >1	Live bed scour

3.4 Simulation work

This study utilized computational fluid dynamics (CFD) modeling to examine how the location, apex angle of flow deflectors and passageway percentage influenced the depth of scour across various flow conditions. Four types of deflectors were used, including two single perforated deflectors (semicircular and triangular) and two double solid deflectors (semicircular and triangular). The Navier-Stokes and continuity equations were discretized using a finite volume and finite difference approach to solve fluid motions, while the RNG κ-ε turbulence model was adopted to model turbulence. The excess bed shear stress resulting from the flowing water was used to determine the bed load model, and the Volume of Fluid (VOF) technique was used to model free surfaces.

3.4.1 Verification of CFD results by experimental work

In the context of verifying the accuracy of the FLOW 3D model, Figure (3.15) illustrates a comparison between the maximum scour depth observed in experimental studies and the corresponding depth simulated by the FLOW 3D model. Table (3.6) presents statistical measures, including the coefficient of determination (R^2), Nash Sutcliffe efficiency coefficient (NSE), and percent bias (PBIAS), to quantify the performance of the numerical model. These measures are expressed as equations (3.6), (3.7), and (3.8), respectively. The statistical measures are further reinforced by the performance classification presented in Table (3.6), which strengthens the validation of the numerical model. Analyzing the statistical performance indicators (PBIAS, NSE, and R^2) from Table (3.6), it can be concluded that the simulated scour results obtained from the numerical model align closely with the results obtained from the laboratory experiments. This demonstrates the effectiveness of FLOW 3D as a reliable tool for accurately estimating the maximum depth of scour and downstream flow depths in a stilling basin.

The values of deflectors angles (in degrees), passageway ratio, and the relative position of the flow deflectors that were being investigated are given in Table (3.7). These values would be replicated for every hydraulic condition and flow deflector type. The statistical performance indicators of numerical model are as follows: NSE=0.908, PBAIS=0.0432, R2=0.9095.

$$R^2=\left(\frac{\sum_{i=1}^{n}(ds_i-\bar{d}s_i)\left(ds_i-\overline{\hat{d}s_i}\right)}{\sum_{i=1}^{n}(ds_i-\hat{d}s_i)^2\sum_{i=1}^{n}\left(\hat{d}s_i-\overline{\hat{d}s_i}\right)^2}\right)^2 \tag{3.6}$$

$$NSE=1-\frac{\sum_{i=1}^{n}\left(\hat{d}s_i-ds_i\right)^2}{\sum_{i=1}^{n}\left(\bar{d}s_i-ds_i\right)^2} \tag{3.7}$$

$$PBIAS=\frac{\sum_{i=1}^{n}(ds_i-\hat{d}s_i)*100\%}{\sum_{i=1}^{n}(ds_i)} \tag{3.8}$$

Where; $\hat{d}s_i$ is the ith predicted depth of scour for the model to be evaluated, and ds_i is the ith measured depth of scour both for specified flow deflectors.

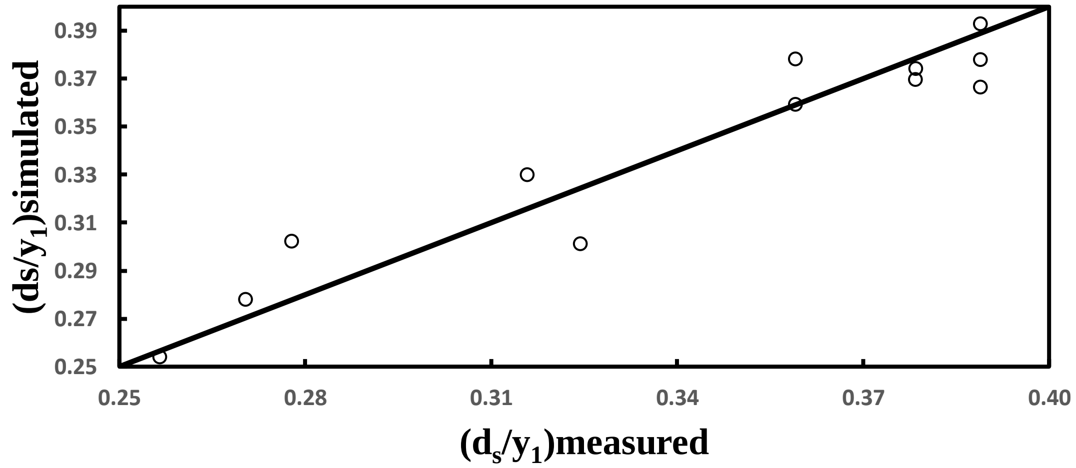

Figure (3.15):Comparison between the measured and simulated scour depth.

Table (3.6): Statistical performance indicators include NSE, R2, and PBIAS (Pradhan et al., 2020).

Classes	(NSE)	(R^2)	(PBIAS)%
Very good model	0.75─1	0.85─1	< ⎮5⎮
Good model	0.65─0.75	0.7─0.85	⎮5⎮─⎮10⎮
Satisfactory model	0.5─0.65	0.6─0.7	⎮10⎮─⎮15⎮
Acceptable model	0.4─0.5	0.4─0.6	------
Unsatisfactory model	≤ 0.4	≤ 0.4	≥ ⎮15⎮

Table (3. 7): summarizes variable ranges and scenarios for each flow deflector type and operational conditions in the simulation study

Case	Fr_1	θ	α_0	L_0
1	Repeated for each Fr_1 $Fr_1 = 0.30$ $Fr_1 = 1.73$ $Fr_1 = 3.01$	45^{o}	40%	25%
2				50%
3				75%
4			20%	25%
5				50%
6				75%
7			10%	25%
8				50%
9				75%
10		90^{o}	40%	25%
11				50%
12				75%
13			20%	25%
14				50%
15				75%
16			10%	25%
17				50%
18				75%
19		135^{o}	40%	25%
20				50%
21				75%
22			20%	25%
23				50%
24				75%
25			10%	25%
26				50%
27				75%

3.4.2 Meshing

A Mesh refers to a grid of blocks that encompasses various geometric shapes and fluid flows **(Flow Science, 2009)**. The software employs the FAVOR technique to eliminate the stair-step effect that can arise with a basic Cartesian grid system by smoothing out the fractional sections of grid cell faces and volumes **(Flow Science, 2009)**. To ensure that the simulation runs smoothly, the adequacy of the mesh cell size needs to be verified by clicking on the FAVOR button prior to running the simulation.

Several trials were conducted, and it was discovered that a uniform cell size of 0.025 m closely approximated the experimental outcomes while also requiring less time. The model has a total length of 10 m in the x-direction, 1 m in the y-direction, and 6 m in the z-direction, as shown in Figure (3.16). Additionally, a nested block mesh with a uniform cell size of 0.0125 m was utilized to cover the flow deflector's geometry since it yielded results that were closest to the experimental results while also taking less time. The model's length in the x-direction is determined by the flow deflector's dimensions, while it is 1 m in the y-direction and 0.2 m in the z-direction.

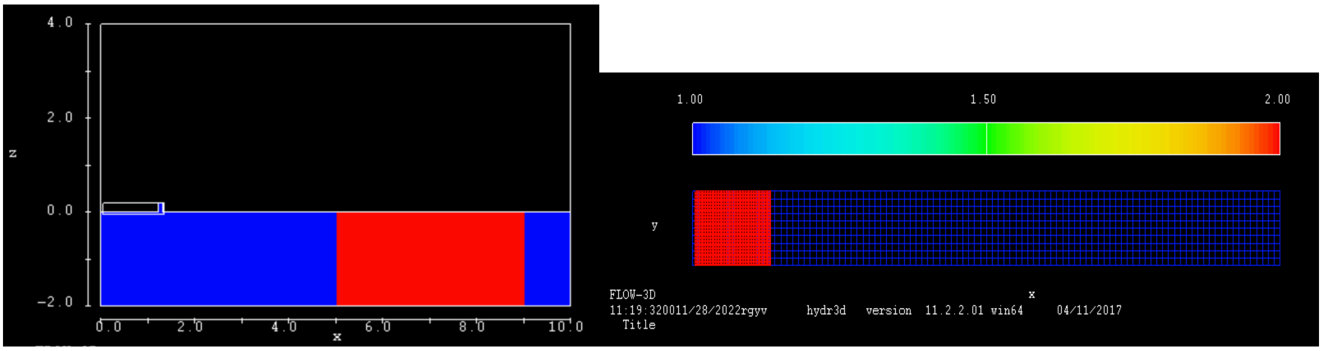

(a) (b)

Figure (3.16): The geometry of open channel for a) side view b) top view.

3.4.3 Boundary Condition

In 3D open channel flow, setting appropriate boundary conditions is crucial for accurate modeling. These boundary conditions define how the flow interacts with the channel's boundaries and help simulate real-world scenarios. In hydraulic engineering, common boundary conditions include specifying water inflow rates, velocities, or water levels at the channel's inlet. Similarly, conditions at the outlet, such as specifying outflow rates or water levels, are essential. Additionally, considering sidewall conditions to simulate the channel's lateral boundaries is essential. Properly defining these boundary conditions ensures that the 3D flow model behaves realistically, allowing engineers to predict flow patterns, velocities, and other critical parameters in open channel hydraulic systems accurately.

Figure (3.17) illustrates the boundary condition that will be used in this study. However, the fluid flow velocity, which varied from the rest of the velocities, determined the upstream boundary. On the other hand, the downstream boundary was defined by specific pressure with varying fluid elevations. The right, left, and bottom boundaries were all designated as walls. Finally, the top boundary was defined as having a specified pressure with a pressure value of zero.

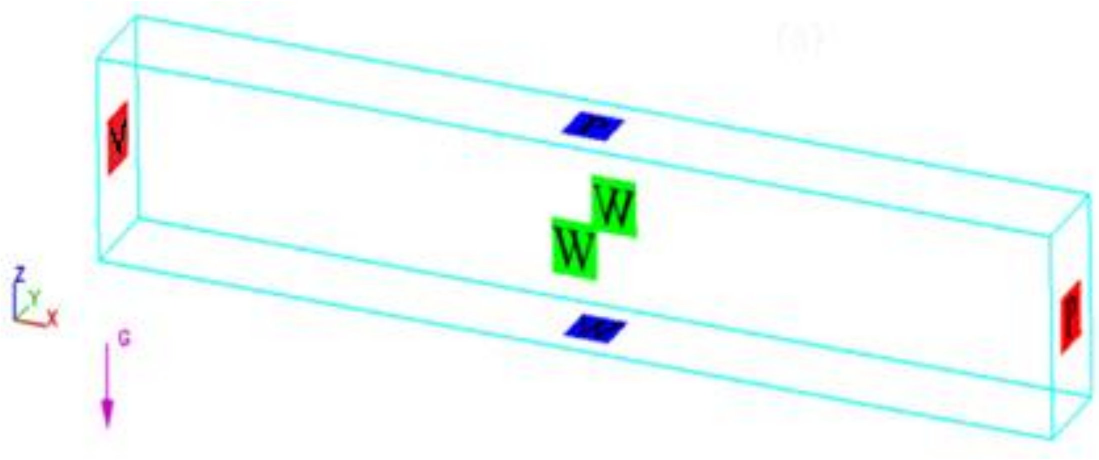

Figure (3.17):Boundary Conditions

Chapter Four

Results and Discussion

4.1 General

Analyzing both experimental and numerical results of flow deflector and stilling basin designs is crucial in reducing local scour around hydraulic structures. Engineers examine data from real-world experiments and computer simulations to assess the effectiveness of different configurations. This analysis guides the refinement of designs for optimal performance and cost-effectiveness, ensuring the protection and longevity of essential hydraulic infrastructure.

4.2 Analysis of experimental results

4.2.1 Local Scour Depth

Figure (4.1) shows the scour patterns in the flume bed for the case of use double solid triangular deflectors. On other hand, Figure (4.1a) illustrates the clear impact of using double solid triangular deflectors on the scouring near the deflectors, as compared to the scenario where no deflectors were employed. The maximum scour depth of 7.0 cm was concentrated at a distance of 0.40 m downstream from the deflectors along the channel's central axis. Conversely, in the absence of deflectors, a maximum scour depth of 1.0 cm occurred across the channel, approximately 6.0 m downstream from the channel's start. The absence of deflectors in this case provided economic advantages, as it reduced the required length of the floor of the stilling basin, protection blocks, and launching apron necessary to protect the channel bed.

Moving on to Figure (4.1b), it can be observed that for higher discharge rates, the scouring extended uniformly forward with deposition bars forming in the central region of the channel. The boundaries of the channel experienced higher scouring zones, reaching depths of 3.0 cm at a distance of 4.6 m from the channel's beginning.

For the scenario with the maximum discharge of 0.044 m^3/sec, as depicted in Figure (4.1c), the scour depths further advanced downstream, covering a distance between 2.5 m to 3.8 m. Scour zones near the channel boundary were repeated along the downstream direction, with a maximum scour depth of 2.0 cm.

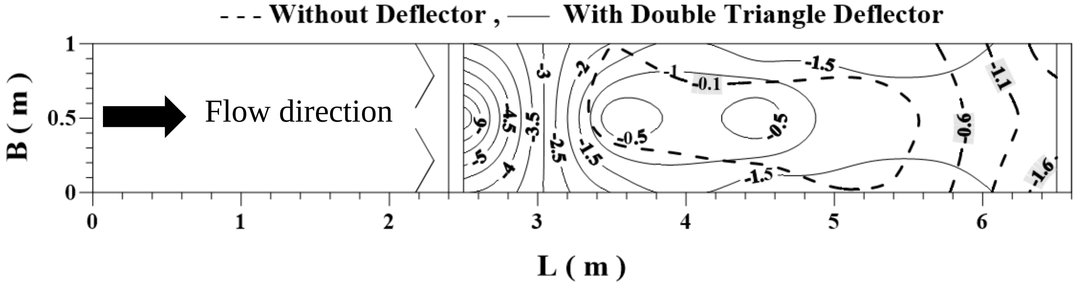

(a) For Q= 0.0154 m^3/sec and Fr_1=0.3, (ds in cm).

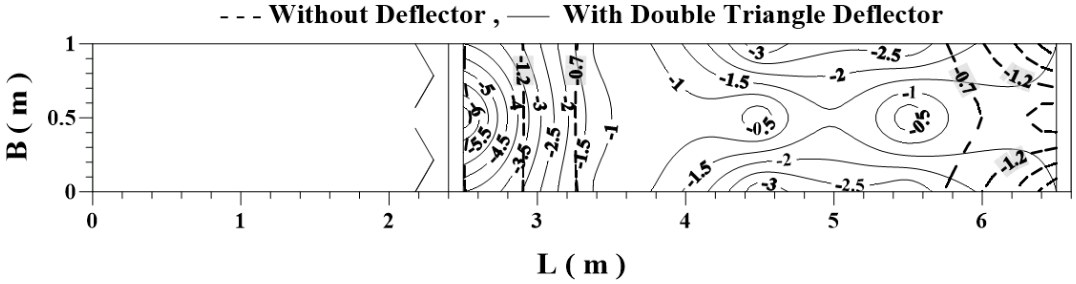

(b) For Q= 0.03 m^3/sec and Fr_1=0.52, (ds in cm).

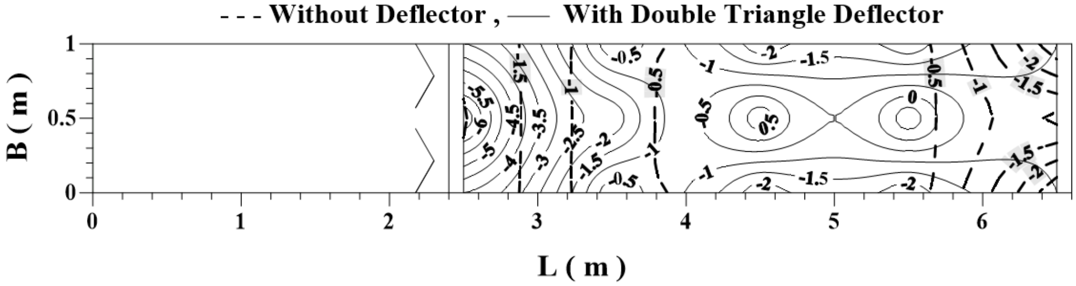

(c) For Q= 0.044 m^3/sec and Fr_1=0.68, (ds in cm).

Figure (4. 1): Morphology of the flume bed downstream the flow deflectors for double-solid triangular deflector with θ=120°.

Figure (4.2) presents the scour patterns observed in the channel bed when single perforated triangular deflectors were utilized. In Figure (4.2a), the scour depth distribution is depicted, indicating the presence of scour near the single triangular deflector on both sides, close to the channel boundaries, with the maximum scour depth reaching 7.0 cm. Along the central axis of the channel, lower values of scour depths were concentrated. As the channel discharge increased to Q=0.0301 m^3/sec, as shown in Figure (4.2b), the scour depth intensified to approximately 3.5 cm. Notably, there was an absence of scour development within the range of 3.4 m to 4.2 m from the deflector. Figure (4.3c) demonstrated a similar scour depth pattern near the deflector zones at the channel's sides, akin to Figure (4.2b), but with a uniform scour depth of 1.0 cm extending from 3.5 m to 4.8 m.

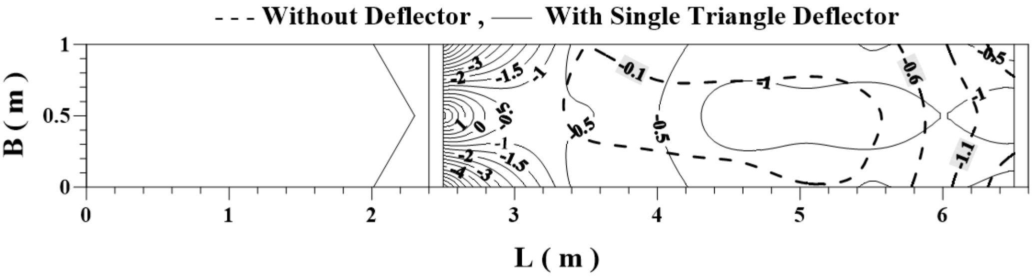

(a) For Q= 0.0154 m^3/sec and Fr_1=0.3, (ds in cm).

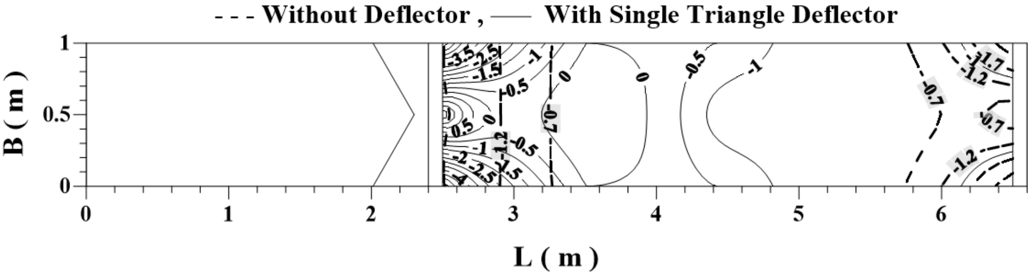

(b) For Q= 0.0301 m^3/sec and Fr_1=0.52, (ds in cm).

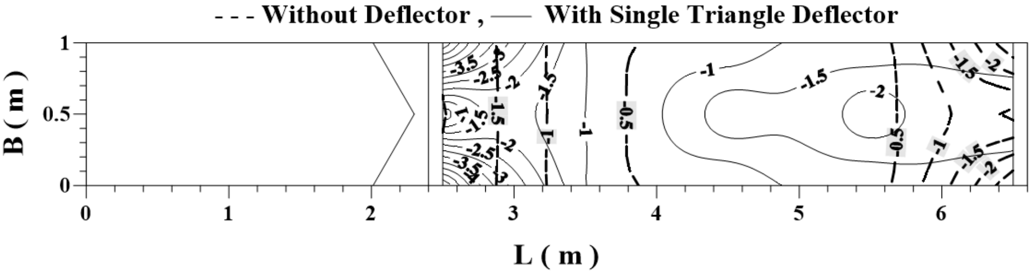

(c) For Q= 0.044 m^3/sec and Fr_1=0.68, (ds in cm).

Figure (4. 2): Morphology of the channel bed downstream flow deflectors for single-perforated triangular deflector with θ=120°.

Figure (4.3) shows the scour patterns in the channel bed for the case of use double solid semi-circle deflectors. The results of Figure (4.3a) indicate that the scouring starts directly near the channel's central axis with a maximum depth of 7.0 cm. The pattern of scour depths is propagated toward the downstream direction on both sides of the channel. For a higher flow rate (i.e., 0.0301 m^3/sec) as shown in Figure (4.3b), the same pattern of scour depths was developed, but more extended downstream of the deflectors.

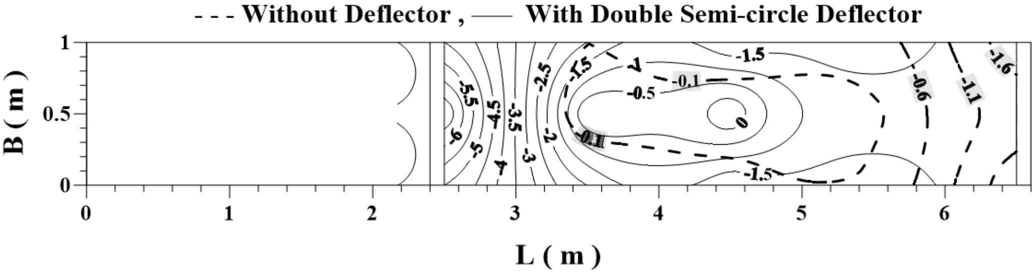

(a) For Q= 0.0154 m^3/sec and Fr$_1$=0.3, (ds in cm).

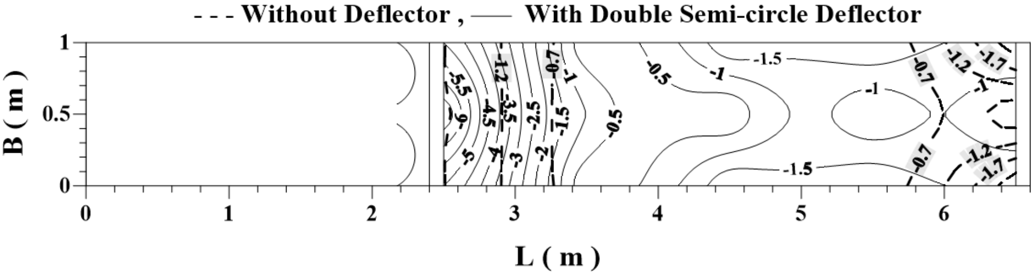

(b) For Q= 0.0301 m^3/sec and Fr$_1$=0.52, (ds in cm).

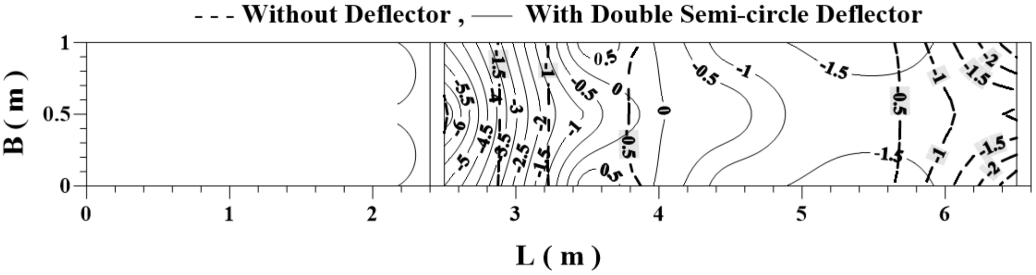

(c) For Q= 0.044 m^3/sec and Fr$_1$=0.68, (ds in cm).

Figure (4. 3): Morphology of the channel bed downstream flow deflectors for double-solid semi-circle deflectors.

Figure (4.3c) shows that as the flow rate increased to 0.044m^3/sec, the scour depths were decreased in the forwarded direction to be vanished at a distance of 4.0 m, beyond this zone, the scour depths pattern was developed slightly along the downstream direction.

Figure (4.4) shows the scour patterns in the channel bed for the case of use single perforated semi-circular deflectors.

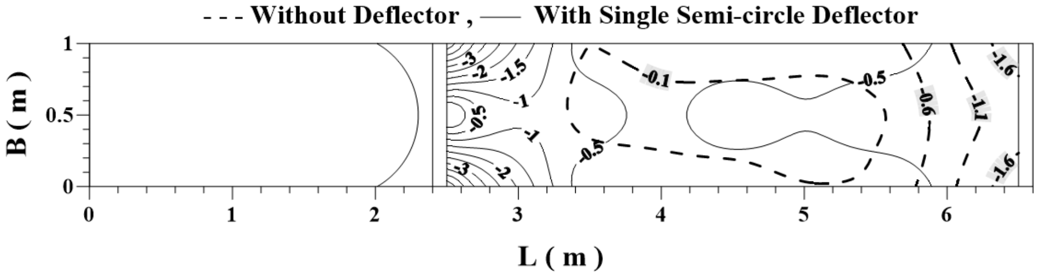

(a) For Q= 0.0154 m^3/sec and Fr_1=0.3, (ds in cm).

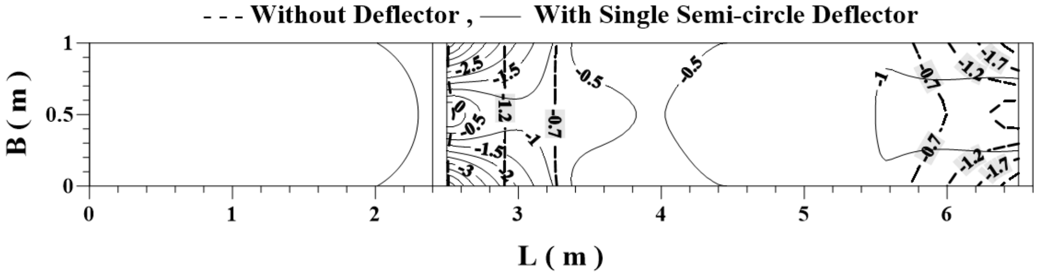

(b) For Q= 0.0301 m^3/sec and Fr_1=0.52, (ds in cm).

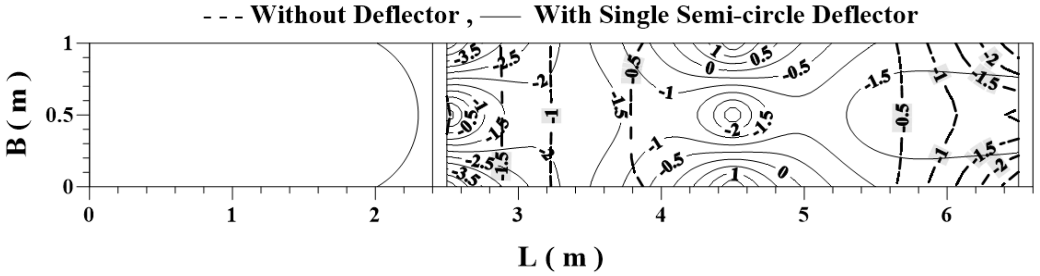

(c) For Q= 0.044 m^3/sec and Fr_1=0.68, (ds in cm).

Figure (4. 4): Morphology of the channel bed downstream flow deflectors for single perforated semi-circle deflectors.

In order, Figure (4.4a) shows that the pattern of scour depth distributed near the nose of the curved deflector on both sides close to the sides of the channel, the maximum scour depth was 5.0 cm. The scour depths of 0.5cm, were dominated the region from 3.4m to 4.4m. As the flow rate increased (see Figure 4.4b), the scour pattern changed obviously as in Figure (4.4c). The maximum scour depth was 3.5 cm symmetrically on the channel corners near the deflector. However, deposition of bed materials has occurred near the channel boundaries far away the distance of 4.0m downstream of the flow.

Table (4.1), summarize the flow conditions, geometry characteristics, and configurations for the flow deflectors, as well as the maximum, measured scour depth $\mathbf{d_s}$ in (cm) and its corresponding position **L** in (m) that was obtained in the present analysis.

Table (4. 1): Summary of Flow Conditions, Geometry Characteristics, and Configurations for Investigated Flow Deflector Types.

Geometric Characteristics and Configurations for Flow Deflectors	**Discharge Q in (m^3/sec)**	**Maximum Scour Depth d_s in(cm)**	**Corresponding Position L in (m)**
Single-perforated triangular deflector: θ= 120° A_t= 1,963.16cm^2 h=17 cm b=0 cm $a_{opining}$=240 cm^2	0.0154	7	2.5
	0.0301	7	2.5
	0.044	6	2.5
Double- solid triangular deflector: θ= 120° A_t= 1688.44 cm^2 h=17 cm b=14 cm $a_{opining}$=238 cm^2	0.0154	7	2.5
	0.0301	7	2.5
	0.044	7	2.5
Single-perforated semicircular deflector: θ = 120° A_t= 2,055.64 cm^2 h=17 cm b=0 cm $a_{opining}$=240 cm^2	0.0154	5	2.5
	0.0301	5	2.5
	0.044	5	2.5
Double- solid semicircular deflector: θ = 120° A_t= 1688.44 cm^2 h=17 cm b=14 cm $a_{opining}$=238 cm^2	0.0154	7	2.5
	0.0301	7	2.5
	0.044	6	2.5

Based on the findings of the experiments, it is obvious that the single-perforated semicircular deflector developed less scour depth in (cm) than other deflectors. The appendix [B] contains a set of pictures that demonstrate the experimental and numerical results for this research.

4.2.2 Energy Dissipation

The efficiency of energy dissipation can be expressed as **(Obaed et al., 2016)**:

$$E\% = \frac{E_2 - E_1}{E_1} \times 100 \qquad (4.\ 1)$$

Where; E_2 and E_1 are the specific energy of the flow at the downstream and upstream of the flow, respectively. The specific energy concept is well known in the analysis of flow in open channel and defined at any arbitrary section *i* in the flow as:

$$E_i = y_i + \alpha \frac{v_i^2}{2g} \qquad (4.2)$$

Where; E_i is specific energy of the flow, y_i is the depth of water, α is the correction coefficient of the kinetic energy (typically set equal to 1.0), and v_i is the mean velocity of the flow. Figure (4.5) shows the efficiency of energy dissipated by each type of deflectors.

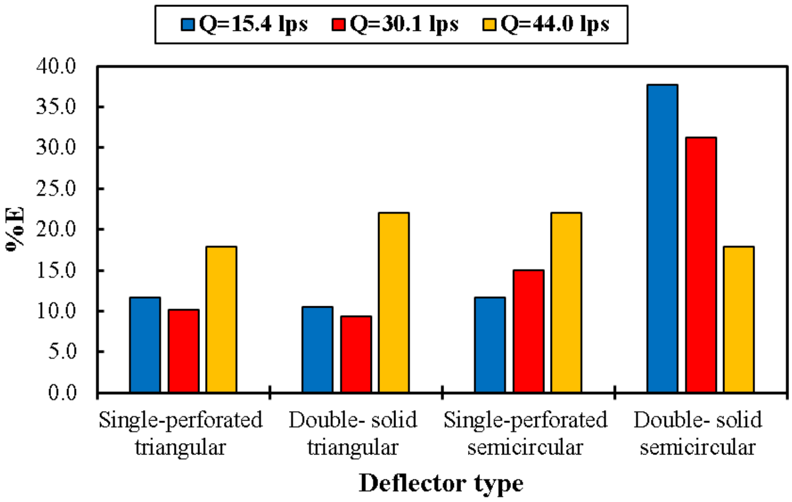

Figure (4. 5): Efficiency of energy dissipation versus different types of flow deflectors.

It was evident from Figure (4.5) that the double solid semi-circular flow deflectors record a high E% of 37.0 that corresponds to low discharge, thereby, this value decreased to 31.27% for Q=0.0311 m^3/sec and approached 18% for high discharge of 0.044 m^3/sec. Whilst, the single-perforated triangular deflector results in a low percentage of energy dissipation efficiency.

On the other hand, the single-perforated semi-circular deflector shows significant values of E% as follows: E= 11.73% corresponds Q=0.0154 m^3 /sec, E= 15.07% for Q=0.0301 m^3 /sec, and E= 22.01% for Q=0.044 m^3 /sec.

In view of the dangerous potentials of local scour in sand-bed channels and its predominant implications on cross-flow hydraulic structures, it was reasonable to consider the single-perforated semi-circular deflector as a successful structure in channels that provides the inhibition of scouring and dissipates the kinetic energy of flow, particularly for high discharges.

4.3 Analysis of numerical results

4.3.1 Parametric Analysis

The underlying association between the depth of scour and the Froude number is an essential aspect of fluid mechanics and hydraulic engineering. The scour depth refers to the excavation of bed material from the bed of a river, by flowing water. It is a measure of the extent of erosion caused by the flow of water and can be influenced by various factors, including the shape and size of flow deflectors, the velocity of the flow, and the grain size of the bed material. The relative importance of inertial and gravitational forces in a fluid flow referred to as the Froude Number is used to determine the flow regime. Therefore, the depth of scour can vary significantly depending on the Froude number of the flow.

Figures (4.6 and 4.9) show the variation of depth of scour with Froude Number, deflector location, deflector angle and openings area for different types of flow deflectors.

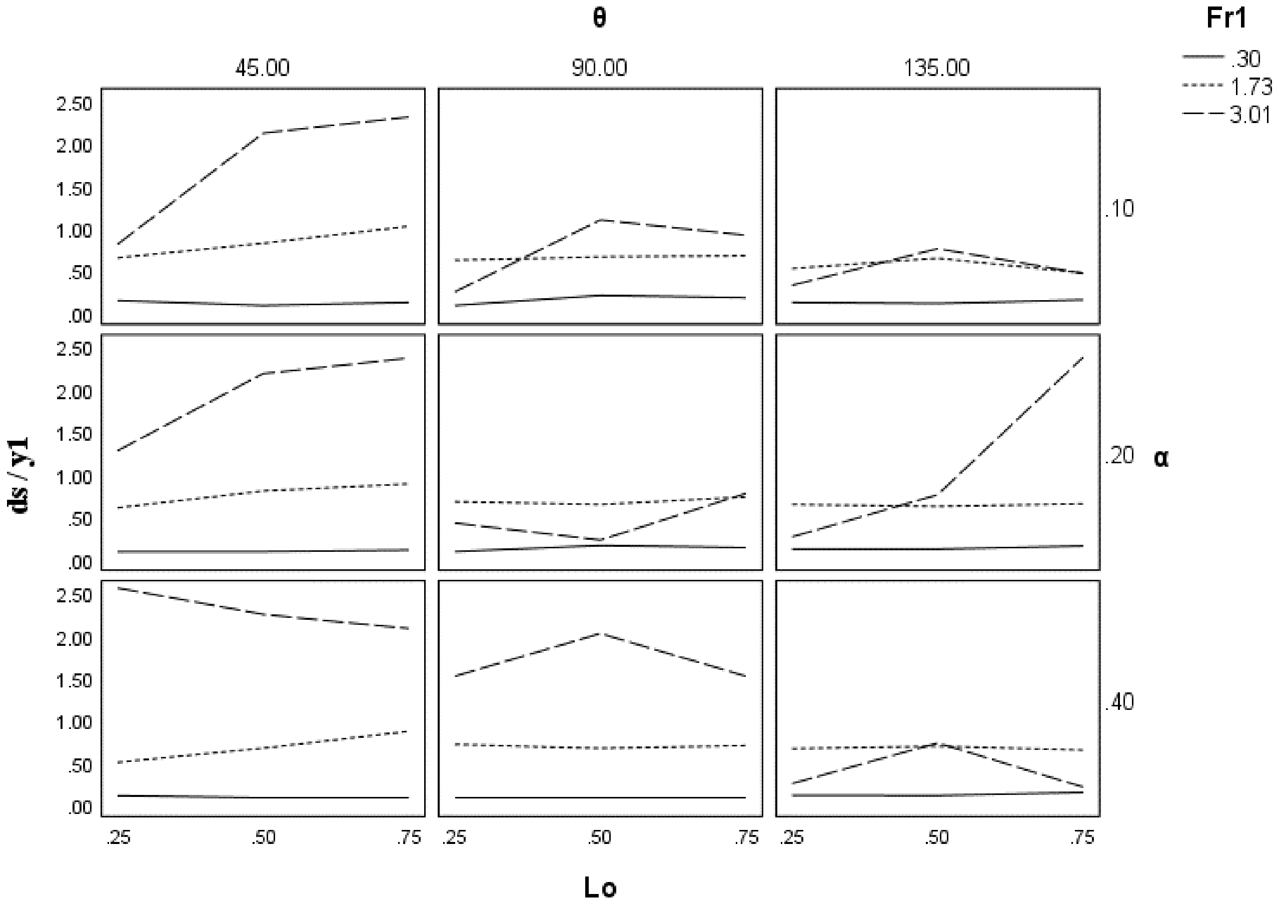

Figure (4. 6): Relationship of depth of scour (d_s/y_1) versus Froude number, deflector location, deflector angle and openings area for single perforated triangular flow deflectors.

In the realm of hydraulic engineering, understanding the relationship between scour depth and the Froude number is pivotal. Scour depth signifies the erosion of sediment from a riverbed by flowing water and depends on factors like deflector shape, flow velocity, and sediment size. The Froude number, which relates inertial and gravitational forces in fluid flow, dictates the flow regime and significantly influences scour depth. When it comes to single perforated triangular flow deflectors, lower Froude numbers (indicating subcritical flow with lower velocity) result in reduced scour depth as shown in Figure (4.6). Conversely, higher Froude numbers (representing supercritical flow) lead to increased scour depth. The deflector angle (θ) also plays a crucial role, with increased θ causing a decrease in scour depth as it slows down the flow near the deflector. The location of the deflector along the flow direction impacts scour depth, with upstream positioning decreasing scour due to flow divergence and slowdown. However, the depth of scour eventually reaches a maximum value dependent on various factors. The opening area (α_o) also affects scour, with larger openings potentially increasing scour.

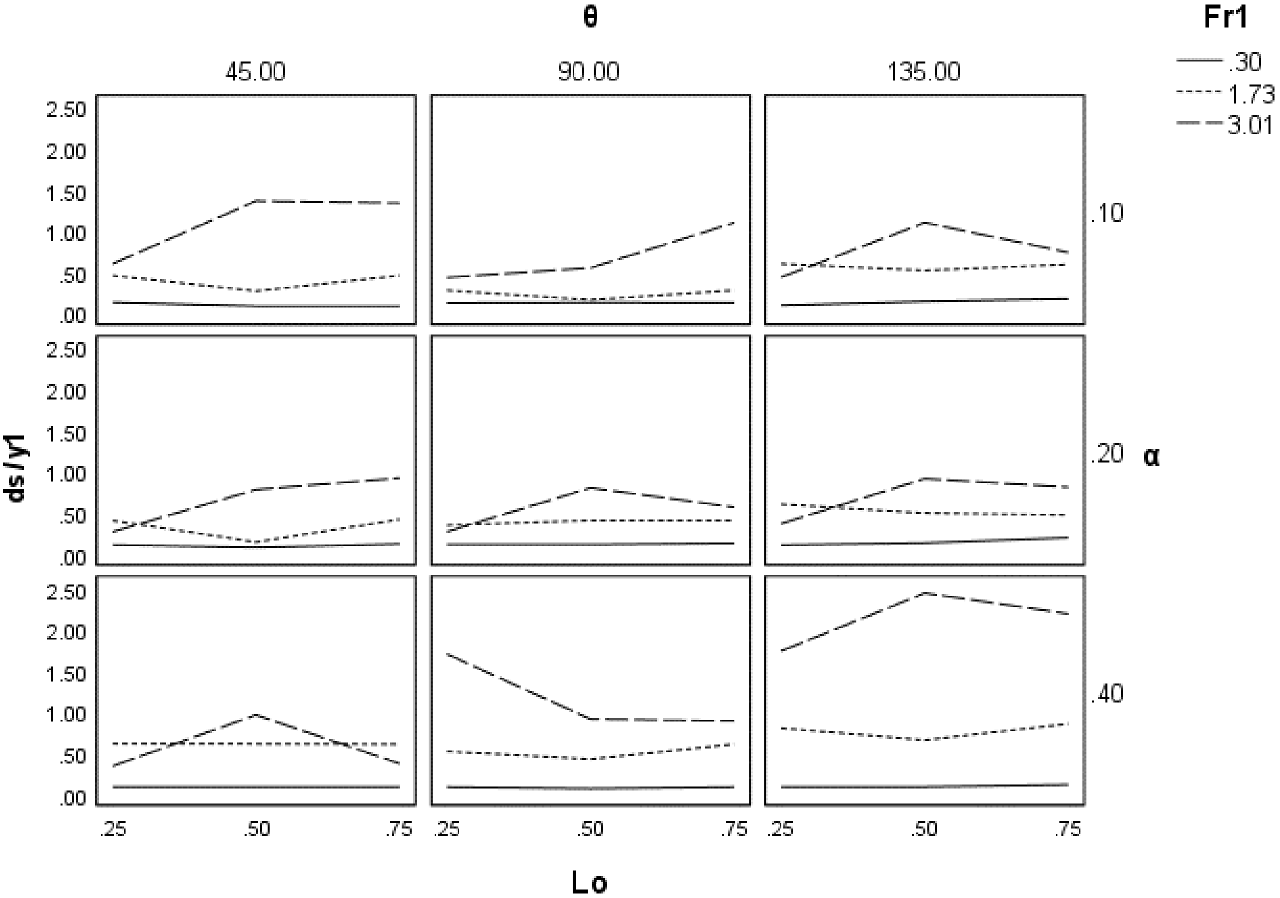

Figure (4. 7): Relationship of depth of scour (d_s/y_1) versus Froude number, deflector location, deflector angle and openings area for single perforated semi-circular flow deflectors.

Focusing on single perforated semi-circular flow deflectors, lower Froude numbers (indicating slower, subcritical flow) tend to result in reduced scour depth. As the Froude number rises and the flow becomes faster and supercritical, scour depth increases as shown in Figure (4.7). The deflector angle (θ) plays a significant role, with greater θ causing increased scour depth as it slows the flow near the deflector. The deflector's location along the flow direction also matters, as upstream positioning decreases scour due to flow divergence and slowdown, until it reaches a maximum value influenced by various factors. Opening area (α_o) affects scour, with larger openings potentially increasing scour. However, the semi-circular deflector's triangular shape can dissipate energy while increasing scour depth, compared to less angular deflectors. These findings underscore the complexity of scour depth and its dependence on multiple factors in hydraulic engineering. Factors such as flow velocity, deflector shape, perforation type and size, and deflector location along the flow direction all interact to influence scour depth, making its prediction and management crucial for effective hydraulic design.

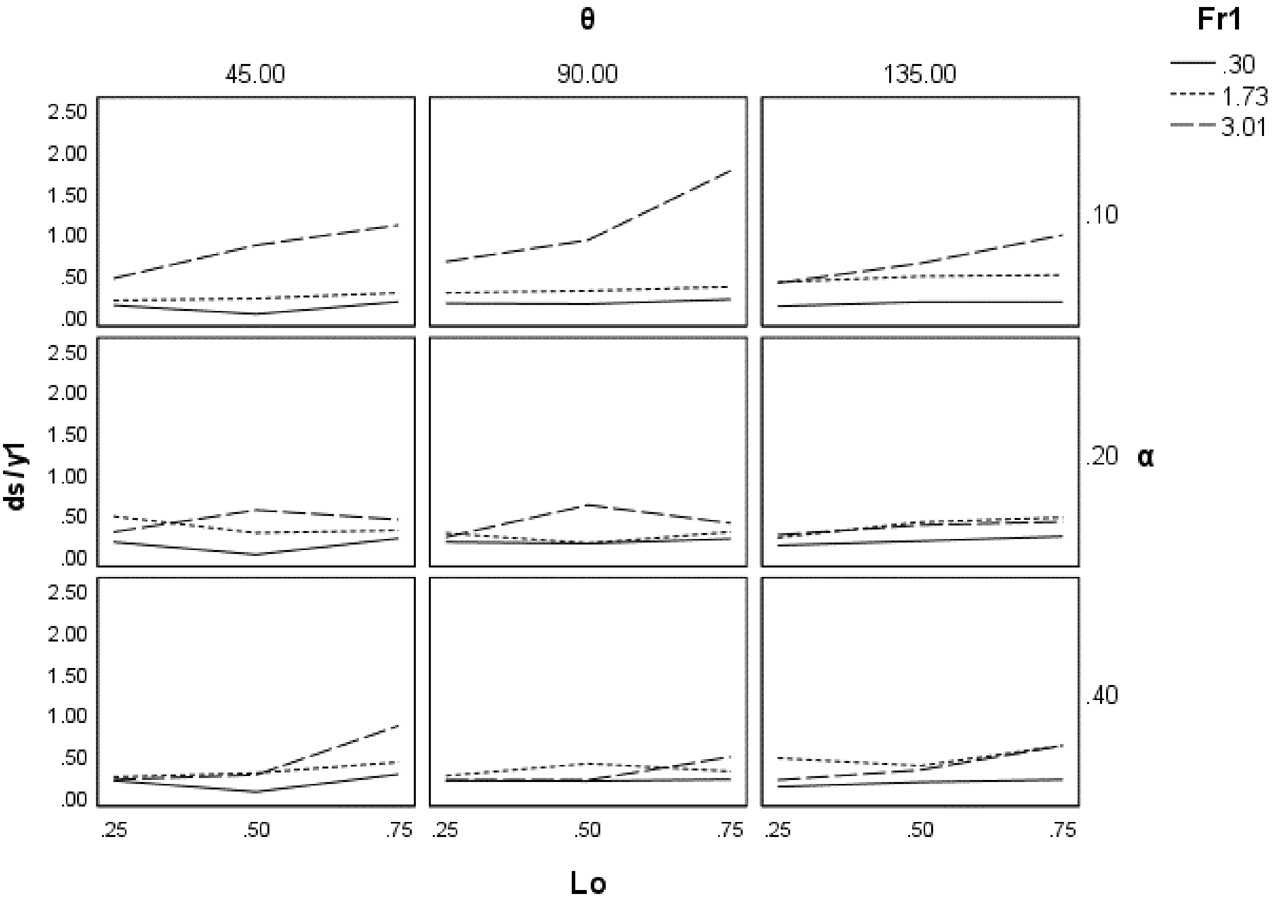

Figure (4. 8): Relationship of depth of scour (d_s/y_1) versus Froude number, deflector location, deflector angle and openings area for double solid semi-circular flow deflectors.

For double solid semi-circular flow deflectors, as the Froude number increases, indicating more active flow, it leads to increased scouring around these deflectors due to higher flow energy causing more bed material erosion as shown in Figure (4.8). Additionally, deflector angle plays a role, with scour depth increasing as the angle increases up to about 90 degrees, beyond which scour depth starts to decrease. Furthermore, the location of the deflector along the flow direction influences scour depth, with upstream placement causing reduced sediment erosion due to flow divergence. Finally, the opening area of the deflector affects scour depth, with smaller openings potentially leading to increased scour. Overall, these findings provide insights into how flow velocity, deflector shape, perforation type and size, and deflector location impact scour depth for double solid semi-circular flow deflectors in hydraulic engineering.

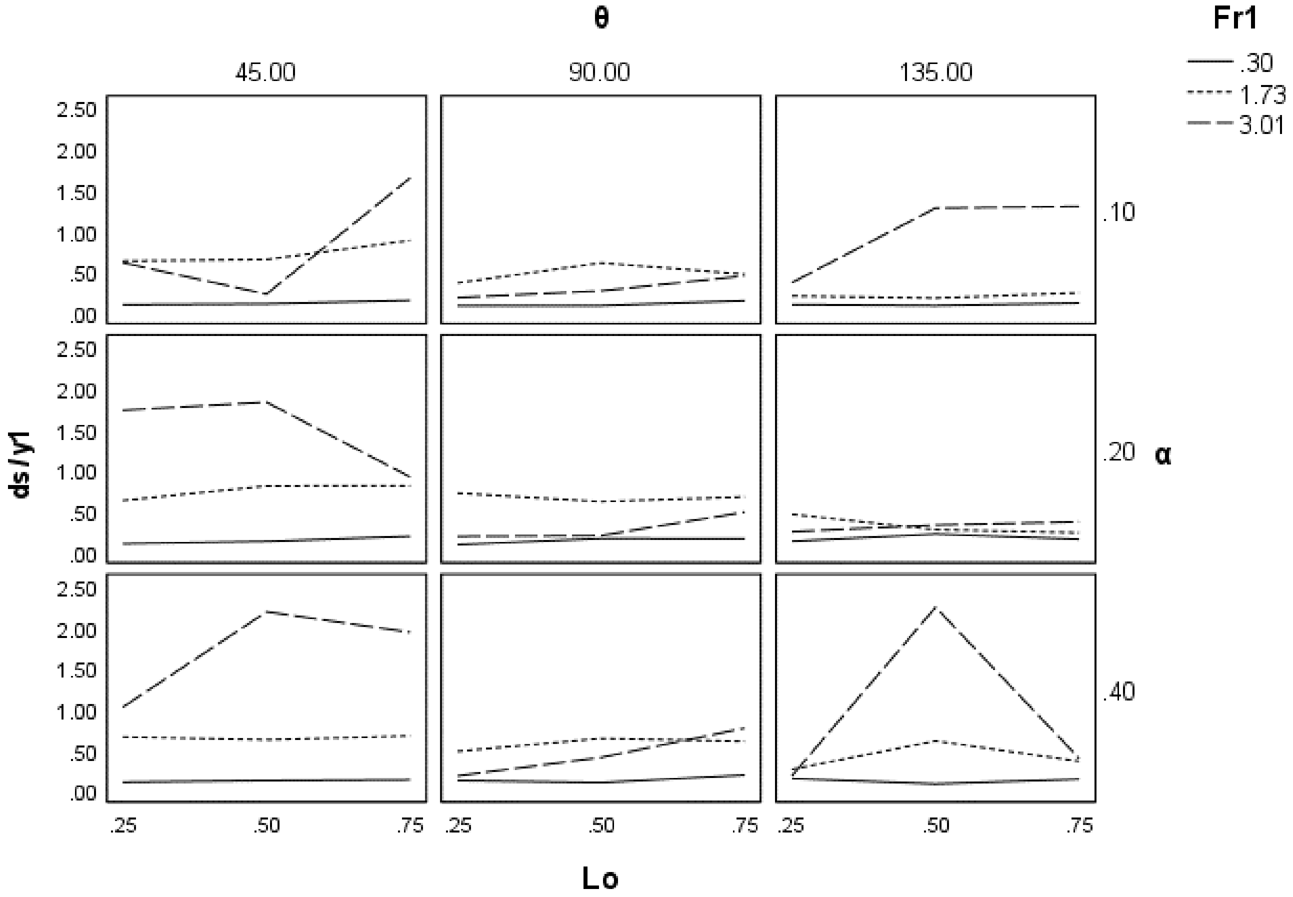

Figure (4. 9): Relationship of depth of scour (d_s/y_1) versus Froude number, deflector location, deflector angle and openings area for double solid triangular flow deflectors.

Scour depth refers to the erosion of sediment on a riverbed by flowing water, influenced by factors like the shape of flow deflectors, flow velocity, and sediment characteristics. The Froude number helps determine the flow regime by considering inertial and gravitational forces in fluid flow. For double solid triangular flow deflectors, we observe that at lower Froude numbers, indicating slower subcritical flow, the scour depth tends to be lower as shown in Figure (4.9). As the Froude number increases, signifying faster supercritical flow, the scour depth increases. This relationship can be attributed to increased flow energy leading to more sediment erosion. The scour depth is also influenced by the deflector angle (θ), with higher angles reducing scour depth due to decreased flow velocity near the deflector. Furthermore, the location of the deflector along the flow direction plays a role, as placing the deflector further upstream decreases scour depth, thanks to flow divergence and reduced sediment erosion. Finally, the opening area of the deflector affects scour depth, with larger openings potentially leading to increased scour. In essence, these findings highlight how flow velocity, deflector shape, perforation type, and size, and deflector location affect scour depth for double solid triangular flow deflectors in hydraulic engineering.

The results that are shown in Table (4.2) evidently indicate that, at $Fr_1=0.3029$ which corresponds to the low flow regime, the minimum scour depth (d_s/y_1) of 0.0025 was observed with solid double semi-circular flow deflectors. This was believed to be associated with the low velocity of flow around the curved boundaries of the deflector in the low flow regime. Alternatively, it can be said that for a high flow regime of $Fr_1=3.0136$, the minimum (d_s/y_1) was recorded by both solid double triangular and semi-circular flow deflectors.

In summary, the relationship between the factors discussed and the scour depth (d_s/y_1) for both single-perforated and double-solid triangular and semi-circular flow deflectors are depending on the flow velocity, deflector shape, perforation type and size, and deflector location along the flow direction. Considering the previous discussion, the influence of each of these factors in more detail is as follows.

Flow velocity is a significant factor that influences scour depth around flow deflectors. As velocity increases, the scour depth also increases due to increased turbulence and shear forces that erode the riverbed. Higher velocities may also cause deflector vibration, leading to more scouring.

Table (4. 2): Summary of scour depths as a function of various flow deflectors and their corresponding affecting variables.

Affecting variables				**Minimum (d_s/y_1)**			
				Perforated Single		**Solid Double**	
Fr_1	**ϕ**	**L_o**	**α_0**	**Triangular**	**Semi-circle**	**Triangular**	**Semi-circle**
0.3029	45	50	0.2	--	--	--	0.0025
0.3029	90	50	0.4	--	0.065	--	--
0.3029	135	50	0.4	--	--	0.0825	--
1.7338	45	50	0.2	--	0.138	--	--
1.7338	90	50	0.2	--	--	--	0.142
1.7338	135	50	0.1	--	--	0.174	--
1.7338	135	75	0.1	0.466	--	--	--
3.0136	45	25	0.2	--	0.262	--	--
3.0136	135	25	0.4	--	--	0.18	0.18
3.0136	135	75	0.4	0.209	--	--	--

The shape of the flow deflector can also have an impact on scour depth. Triangular deflectors cause more scouring than semi-circular deflectors due to their sharp edges creating more turbulence and flow disruption. In contrast, the smooth curves of semi-circular deflectors generate less turbulence and are less likely to cause scouring.

Perforation type and size affect scour depth. Single-perforated deflectors cause more scouring than double-solid deflectors, as the perforation creates a concentrated flow of water that can erode the riverbed. Larger perforations generate more turbulence and flow disturbance than smaller perforations.

Finally, deflector location along the flow impacts scour depth. Closer location to the riverbank causes more scouring due to restricted water flow being forced to move more rapidly around the deflector. In contrast, further location from the bank generates less turbulence and is less likely to cause scouring.

4.3.2 Regression Models for Scour Depth

Statistical analysis establishes relationships between dependent and independent variables that are correlated. This research used IBM SPSS Statistics 25 for data analysis and mathematical modeling of numerical data related to scour depth variables. Scour depth data caused by flow deflectors were used as a dataset to derive a model for scour depths. Descriptive statistics for depth of scour characteristics caused by flow deflectors are presented in Table (4.3). The method of dimensional analysis was used to establish a correlation between the major parameters and the independent variables in the follows:

$$d_s = f\left(Fr_1, \theta, L_0, \alpha_0, k_g\right) \tag{4.3}$$

Where; K_g is the function of geometric shape of the flow deflector. The explicit expression of the user-defined model in Eq. (4.3) is applicable to both single perforated and double solid semi-circular deflectors. For single perforated or double solid semi-circular deflectors, the user-defined model of Eq. (4.3) can be expressed explicitly as:

$$\frac{d_s}{y_1} = b_0 + b_1 (Fr_1)^{b_2} (L_0)^{b_3} \left((\theta)^{b_4} (\alpha_0)^{b_5} K_g + b_1\right) \tag{4.4}$$

In which;

$$K_g = N^{c_1} \tag{4.5}$$

Where; *N* is the number of the semi-circular flow deflectors across the flow. Table (4.4) shows the parameter estimates obtained from conducting nonlinear regression analysis using IBM SPSS statistics 25.0 software. The ANOVA results obtained from the regression analysis is presented in Table (4.5).

Table (4. 3): Descriptive Statistics for Parameters of Scour Depth

Variables / **Statistic**	**Minimum**	**Maximum**	**Mean**	**Standard deviation**	**Skewness**	**Kurtosis**
d_s/y_1	0.003	2.555	0.497	0.506	2.058	4.300
Fr	0.303	3.014	1.683	1.109	-0.068	-1.500
θ (rad.)	0.785	2.356	1.571	0.642	0.000	-1.500
L_0	0.250	0.750	0.500	0.204	0.000	-1.500
α_0	0.096	0.409	0.233	0.123	0.374	-1.491

Table (4. 4): Parameter estimates for Eq. (4.4).

Parameter	**Estimate**	**Std. Error**	**95% Confidence Interval**	
			Lower Bound	**Upper Bound**
b_0	0.121	0.033	0.056	0.186
b_1	0.314	0.051	0.214	0.414
b_2	1.735	0.259	1.223	2.248
b_3	0.390	0.100	0.193	0.586
b_4	2.967	0.600	1.782	4.153
b_5	2.899	0.570	1.773	4.024

Table (4. 5): Results of ANOVA analysis for Eq. (4.4).

Source	**Sum of Squares**	**df**	**Mean Squares**
Regression	45.279	21	2.156
Residual	7.114	141	0.050
Uncorrected Total	52.393	162	--
Corrected Total	25.057	161	--
R^2 =0.716			

Thus, the final form of Eq. (4.4) is as follows:

$$\frac{d_s}{y_1}=0.121+0.314(Fr_1)^{1.735}(L_0)^{0.39}\left((\theta)^{2.967}(\alpha_0)^{2.899}K_g+0.314\right) \quad (4.6)$$

In which;

$$K_g = N^{-34} \quad (4.7)$$

Likewise, the user-defined model of Eq. (4.3) can be explicitly expressed for single perforated or double triangular deflectors as follows:

$$\frac{d_s}{y_1}=c_0+c_1(Fr_1)^{c_2}(L_0)^{c_3}(\theta)^{c_4}(\alpha_0)^{c_5}\left(K_g\right) \quad (4.8)$$

In which;

$$K_g = N^{d_1} \quad (4.9)$$

In Table (4.6), the estimates for the parameters resulting from a nonlinear regression analysis carried out using IBM SPSS Statistics 25.0 software are presented. Table (4.7) presents the ANOVA outcomes obtained from the same regression analysis.

Table (4. 6): Parameter estimates for Eq. (4.6).

Parameter	**Estimate**	**Std. Error**	**95% Confidence Interval**	
			Lower Bound	**Upper Bound**
c_0	0.126	0.056	0.017	0.236
c_1	0.528	0.157	0.219	0.838
c_2	1.490	0.250	0.996	1.984
c_3	0.367	0.103	0.162	0.571
c_4	-0.960	0.128	-1.213	-0.707
c_5	0.243	0.077	0.090	0.396

Table (4. 7): Results of ANOVA analysis for Eq. (4.6).

Source	**Sum of Squares**	**df**	**Mean Squares**
Regression	92.172	21	4.389
Residual	17.552	141	0.124
Uncorrected Total	109.724	162	
Corrected Total	55.780	161	
R^2 =0.685			

Therefore, the final form of Eq. (4.8) can be expressed as follows:

$$\frac{d_s}{y_1}=0.126+0.528{Fr_1}^{1.49}{L_0}^{0.367}\theta^{-0.96}{\alpha_0}^{0.243}k_g \quad (4.10)$$

In which;

$$K_g = N^{-0.609} \quad (4.11)$$

4.3.3 Evaluation of Regression Models

Evaluation of regression models involves assessing how well the model fits the data and how accurate its predictions are. A good model will produce a plot where the data points closely follow a straight line, indicating that the model accurately predicts the result. Other types of plots, such as residual plots, can also be used to evaluate the model's performance by examining the distribution and pattern of the residuals, which are the differences between the actual data and the predicted values from the model. Plot evaluation is useful for statistical measures, as it provides a more intuitive and accessible way of assessing the model's performance. In addition, there are various statistical measures such as the coefficient of determination (R^2), mean squared error (MSE), and root mean squared error (RMSE). The evaluation process helps determine the reliability and practicality of the regression model for predicting future results. Figure(4.14) shows the verification plots for $(d_s/y_1)_{Pred.}$ regression model for semi-circular deflectors.

Results of Figure (4.14) can provide valuable insights into the accuracy of the predictions and the effectiveness of the deflectors in reducing scour. However, scattered plot shows a dependable and moderate positive correlation between the predicted and calculated scour depths. This may indicate that the deflectors are relatively effective in reducing scour. For the residuals plot, there is a pattern in the residuals plot such as a cluster of points that do not regularly fall above or below the zero line, particularly concentrated for lower scour depths (for a range between 0 to 0.9). This would indicate that the predictive model is reasonably representing the relationship between the design parameters and the resulting scour depth. From the probability plot, as indicated the calculated scour depth values are not falling closely along the diagonal line for a large part of the data points. Thus, deviations may indicate that the predictive model was little accuracy in estimating scour depth.

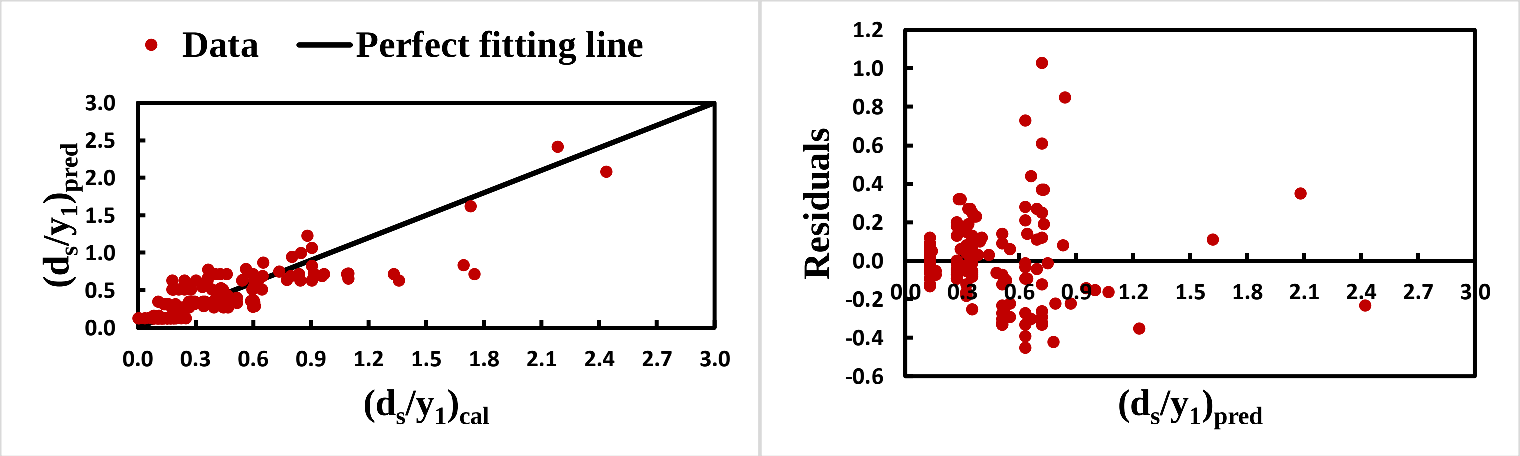

(a) Scattered plot for $(d_s/y_1)_{Pred.}$ versus $(d_s/y_1)_{cal.}$

(b) Residuals versus $(d_s/y_1)_{Pred.}$ plot.

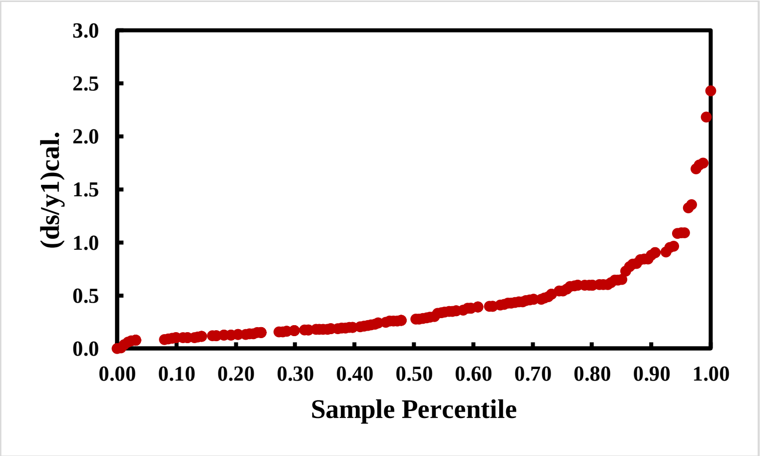

(c) Probability versus $(d_s/y_1)_{cal.}$ Plot.

Figure (4.10): Graphical validation of the $(d_s/y_1)_{Pred.}$ regression model applied to semi-circular deflectors.

Results of Figure (4.10) can provide valuable insights into the accuracy of the predictions and the effectiveness of the deflectors in reducing scour. However, scattered plot shows a dependable and moderate positive correlation between the predicted and calculated scour depths. This may indicate that the deflectors are relatively effective in reducing scour. For the residuals plot, there is a pattern in the residuals plot such as a cluster of points that do not regularly fall above or below the zero line, particularly concentrated for lower scour depths (for a range between 0 to 0.9). This would indicate that the predictive model is reasonably representing the relationship between the design parameters and the resulting scour depth. From the probability plot, as indicated the calculated scour depth values are not falling closely along the diagonal line for a large part of the data points. Thus, deviations may indicate that the predictive model was little accuracy in estimating scour depth.

The plot for verifying the $(d_s/y_1)_{Pred.}$ regression model for triangular deflectors is displayed in Figure (4.11). The verification plots shown in Figure (4.11) show the scour depth predictions and the effectiveness of triangular deflectors in reducing scour. A scatter plot of predicted versus calculated scour depths reveals a reasonable positive correlation between the two variables. This finding suggests that triangular deflectors may be active in reducing scour, particularly for design parameters associated with lower scour depths. A residuals plot of the predicted versus calculated scour depths shows a real pattern, with a collection of points focused below the zero line, particularly for lower scour depths in the range of 0.25 to 1.5. This collect suggests that the predictive model is adequately capturing the relationship between design parameters and resulting scour depth.

Finally, a probability plot of the calculated scour depth values compared to the theoretical quantiles of a standard normal distribution reveals deviations from the diagonal line, particularly for a portion of the data points. This finding indicates that the predictive model may have acceptable accuracy in estimating scour depth.

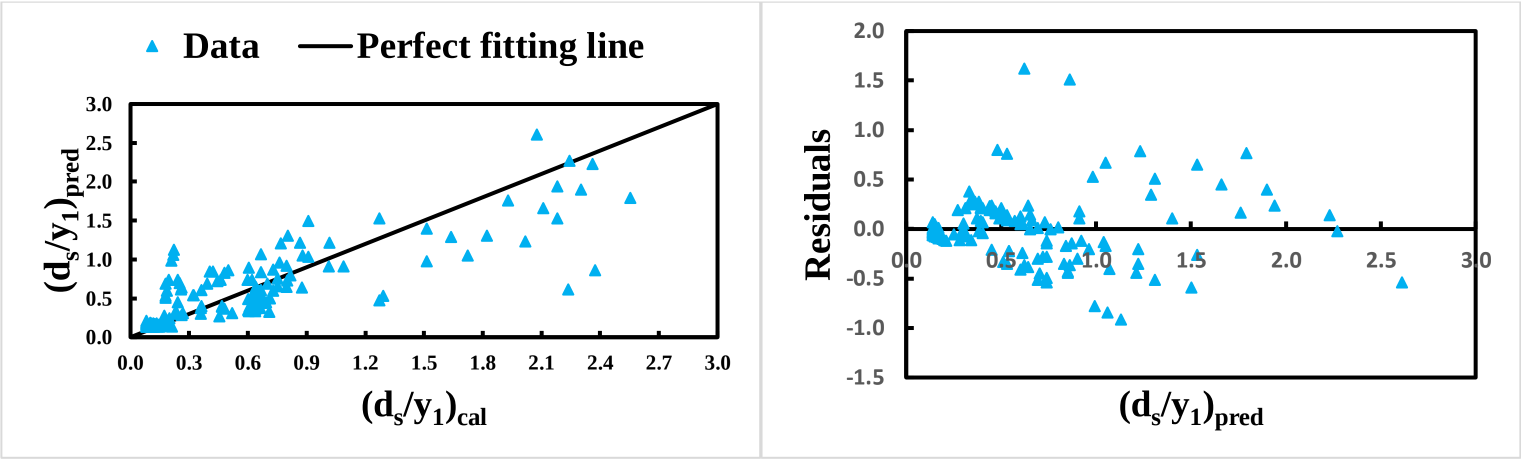

(a) Scattered plot for $(d_s/y_1)_{Pred.}$ versus $(d_s/y_1)_{cal.}$ (b) Residuals versus $(d_s/y_1)_{Pred.}$ plot.

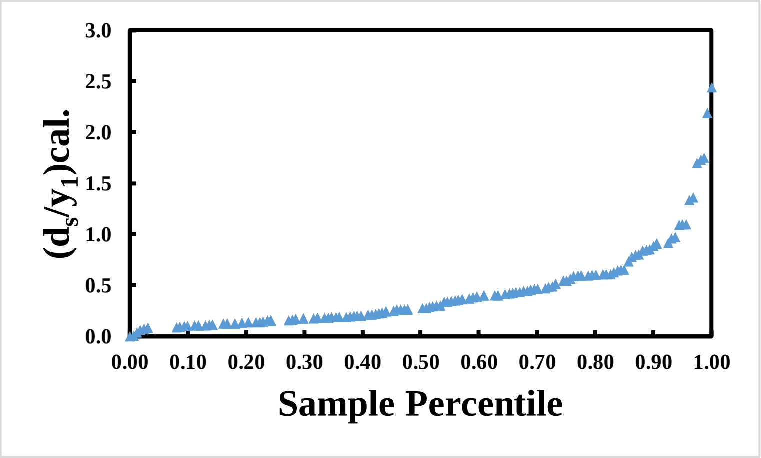

(c) Probability versus $(d_s/y_1)_{cal.}$ Plot.

Figure (4. 11): Graphical validation of the $(d_s/y_1)_{Pred.}$ regression model applied to triangular deflectors.

Furthermore, Table (4.8) presents statistical measures such as the mean squared error (MSE) and root mean squared error (RMSE) for single perforated as well as double solid triangular and semi-circular flow deflectors. The inclusion of these statistical measures serves to strengthen the validation of the regression models. The MSE and RMSE are expressed as:

$$\mathrm{MSE}=\frac{1}{n}\sum_{i=1}^{n}\left(\hat{d}s_i-ds_i\right)^2 \qquad (4.12)$$

$$\mathrm{RMSE}=\sqrt{\frac{1}{n}\sum_{i=1}^{n}\left(\hat{d}s_i-ds_i\right)^2} \qquad (4.13)$$

Where; $\hat{d}s_i$ is the ith predicted depth of scour for the model to be evaluated, and ds_i is the ith measured depth of scour both for specified flow deflectors.

Table (4. 8): Evaluation statistics for prediction models.

Predictive Model	**MSE**	**RMSE**
Eq. (4.6)	0.0439	0.2095
Eq.(4.10)	0.1083	0.3291

It is commonly agreed that a lower value of RMSE indicates a higher performance of the model, while large values, an error in the predictions.

Chapter Five

Optimization-Based Approach in Design of Flow Deflectors.

5.1 General

In hydraulic engineering, we often encounter situations where we need to address two critical challenges simultaneously: preventing local scour to protect our structures and minimizing the surface area of flow deflectors to save costs. It's like trying to achieve two important goals at once. Local scour can damage our infrastructure, which we definitely want to avoid, but we also want to be smart about our resources and not spend too much on flow deflectors. So, we use advanced engineering techniques to find the perfect balance between these two objectives. This means we're looking for solutions that keep our structures safe while using the least amount of materials, which saves money. These multi-objective problems require careful analysis and clever design to ensure our hydraulic systems are both effective and cost-efficient.

The optimization-based approach involves analyzing various characteristics of flow deflectors, such as their shape, size, and material, and using mathematical models and simulations to determine the optimal design dimensions for reaching the desired objectives. This approach enables engineers to construct more efficient and effective flow deflectors that can enhance the hydraulic performance of hydraulic structures.

5.2 Formulation of Optimization Problem

This study has incorporated four different types of flow deflectors. A comprehensive set of 324 CFD simulations was conducted to analyze the performance of flow deflectors under varying operational conditions, dimensions, and configurations in the flow field. In order to determine the applicable ranges of hydraulic design variables for this problem, several control and regulating hydraulic structures were surveyed along the Euphrates River in the Middle Euphrates region, as part of the practical approach being taken as reported in Tables (3.1) and (3.2), respectively.

5.3 Optimization Functions with Multiple Objectives

This study deals with a multi-objective optimization problem that focuses on minimizing the construction material used for the flow deflectors and the depth of scour holes developed downstream deflectors. The multi-objective optimization vector of this problem is formulated as follows:

Find $var. = \begin{Bmatrix} \theta \\ a_0 \\ L_0 \\ h \end{Bmatrix}$

In which; var.is the vector of design variables that are involved in objective functions and constraints. The general mathematical form of the present optimization problem is:

$$\text{Minimize: } f=\{f_1\ (var.),\ f_2\ (var.)\} \quad (5.1)$$

Subject to:

$$\begin{aligned} c &= \{C_1\,(var.), C_2\,(var.)\} \\ var._l &\le var. \le var._u \end{aligned} \quad (5.2)$$

Where; $var._l$ and $var._u$ are the lower and upper bounds for design variables.

Multi-Objective Optimization Problems (MOP) aim to find the best solution that meets all objectives as much as possible. There are several methods for solving multi-objective optimization problems. One of the methods for solving MOP is the Weighted Summation approach, which involves assigning weights to each objective and then combining them into a single function.

The general form of a MOP problem using the weighted summation method can be written as follows:

$$Minimiz\ \mathcal{F} = w_1 f_1\,(var.) + w_2 f_2\,(var.) + \cdots + w_n f_n\,(var.) \tag{5.3}$$

Where; $w_1 + w_2 + \cdots + w_n = 1$

Subjected to:

$$gi(var.)\ \leq\ 0, i = 1, \ldots, m \tag{5.4}$$

$$hj(var.)\ \leq\ 0, i = 1, \ldots, p \tag{5.5}$$

In which; n is the number of objective functions, w_1, w_2, ..., w_n are the weights assigned to each objective, *gi(var.)* are the *m* inequality constraints, and *hj(var.)* are the *p* equality constraints.

5.3.1 Mathematical Formulating for Objective Functions

The formulation of objective functions for flow deflectors is dependent on the particularities of the problem and the optimization objectives. As a result, four functions were derived with the goal of minimizing the amount of construction materials used, based on the concept that the volume is equal to the product of the flow deflector's surface area and its unit thickness. Therefore, in this section, the surface areas of the flow deflectors will be determined based on their type.

5.3.1.1 The objective functions of a single-perforated triangular deflector:

Figure (5.1) presents a schematic layout for the flow deflector of type single perforated triangular shape.

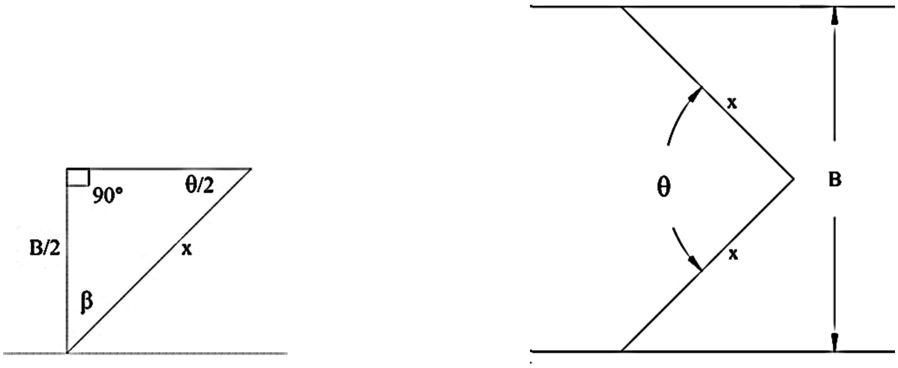

a) Top view

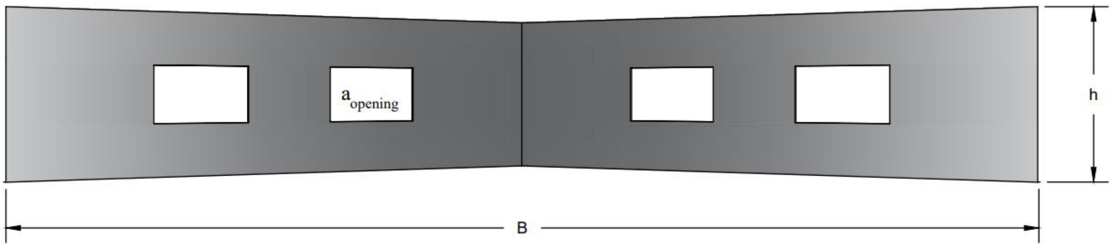

a) Front view

Figure (5. 1): Single perforated triangular deflector

Obj. (ST) =Surface area of flow deflector =S_{ST}

Obj.$_{Scour}$ (ST) = Maximum relative depth of local scour (d_s/y_1).

For a given height of flow deflector, denoted as (h). Thus; the minimum surface area of flow deflector can be expressed as:

$$S_{st}=2(x\,h-2\,a_{opening}) \tag{5.6}$$

In which; $a_{opening}$ is the area of perforation within the deflector surface area (in this study we considered four perforation area in the deflector). Referring to Figure (5.1).

$$\beta=180°-\left(90°+\frac{\theta}{2}\right)=90°-\frac{\theta}{2} \tag{5.7a}$$

$$\because \cos\beta=\frac{B/2}{x} \tag{5.7b}$$

$$\therefore x = \frac{B}{2\cos\beta} \tag{5.8a}$$

By sub. eq.(5.7b) into eq.(5.8a);

$$\therefore x = \frac{B}{2\cos\left(90° - \frac{\theta}{2}\right)} \tag{5.8b}$$

Or;

$$\cos\left(90° - \frac{\theta}{2}\right) = \sin\left(\frac{\theta}{2}\right) \tag{5.8c}$$

$$\therefore x = \frac{B}{2\sin\left(\frac{\theta}{2}\right)} \tag{5.9}$$

By sub. eq.(5.9) into eq.(5.6);

$$S_{st} = \frac{B\,h}{\sin\frac{\theta}{2}} - 4\,a_{opening} \tag{5.10a}$$

$$\because \alpha_0 = \frac{4\,a_{opening}}{S_{st}} \tag{5.10b}$$

$$\therefore 4\,a_{opening} = \alpha_0\,S_{st} \tag{5.11a}$$

Sub. eq.(5.11a) into eq.(5.10b); we get:

$$S_{st} = \frac{B\,h}{\sin\frac{\theta}{2}} - \alpha_0\,S_{st} \tag{5.11b}$$

Or;

$$S_{st} = \frac{B\,h}{(1+\alpha_0)\sin\frac{\theta}{2}} \tag{5.11c}$$

Thus;

$$\therefore \text{Obj.(ST)} = \frac{B\,h}{(1+\alpha_0)\sin\frac{\theta}{2}} \tag{5.12}$$

$$\text{Obj.}_{\text{Scour}}\,\text{(ST)} = \frac{d_s}{y_1} = 0.126 + 0.528\left(Fr_1^{1.49}\right)\left(L_0^{0.367}\right)\left(\theta^{-0.96}\right)\left(\alpha_0^{0.243}\right) \tag{5.13}$$

5.3.1.2 The objective functions of a double-solid triangular deflector

Figure (5.2) shows a schematic layout for the flow deflector of type double solid triangular shape.

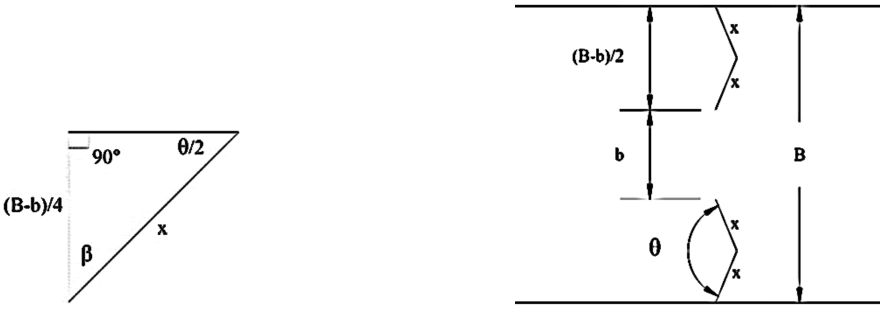

a) Top view

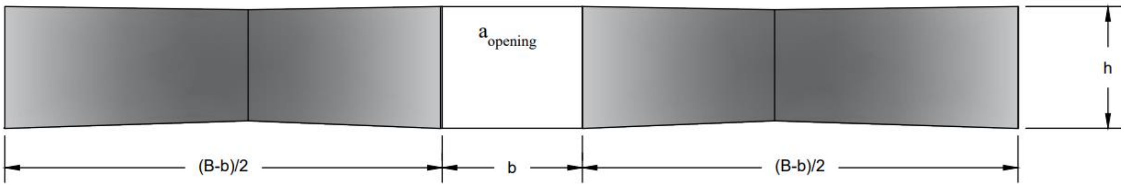

a) Front view

Figure (5. 2): Double solid triangular deflector

Obj. (DT) =Surface area of flow deflector =S_{DT}

Obj.$_{\text{Scour}}$ (DT) = Maximum relative depth of local scour (d_s/y_1).

∴ The minimum surface area of deflector is :

$$S_{dt}=2(2\,x\,h) \tag{5.14}$$

From Figure (5.2)

$$\beta=180°-\left(90°+\frac{\theta}{2}\right)=90°-\frac{\theta}{2} \tag{5.15a}$$

$$\because \cos\beta=\frac{(B-b)/2}{2\,x} \tag{5.15b}$$

$$\therefore x=\frac{(B-b)}{4\cos\beta} \tag{5.16a}$$

By sub. eq.(5.15b) into eq.(5.16a);

$$\therefore x = \frac{(B-b)}{2\cos\left(90° - \frac{\theta}{2}\right)} \tag{5.16b}$$

Or;

$$\cos\left(90° - \frac{\theta}{2}\right) = \sin\left(\frac{\theta}{2}\right) \tag{5.16c}$$

$$\therefore x = \frac{(B-b)}{2\sin\left(\frac{\theta}{2}\right)} \tag{5.17}$$

By sub. eq.(5.17) into eq.(5.14);

$$S_{dt} = \frac{(B-b)\ h}{\sin\frac{\theta}{2}} \tag{5.18a}$$

Or;

$$S_{dt} = \frac{B\ h}{\sin\frac{\theta}{2}} - \frac{1}{\sin\frac{\theta}{2}}(b\ h) \tag{5.18b}$$

$$\because \alpha_0 = \frac{b\ h}{S_{dt}} \tag{5.19a}$$

$$\therefore b\ h = \alpha_0\ S_{dt} \tag{5.19b}$$

Sub. eq.(5.19b) into eq.(5.18b); we get:

$$S_{dt} = \frac{B\ h}{\sin\frac{\theta}{2}} - \frac{1}{\sin\frac{\theta}{2}}(\alpha_0\ S_{dt}) \tag{5.20a}$$

Or;

$$S_{dt} = \frac{B\ h}{\left(\alpha_0 + \sin\frac{\theta}{2}\right)} \tag{5.20b}$$

Thus;

$$\therefore \text{Obj.(DT)} = \frac{B\ h}{\left(\alpha_0 + \sin\frac{\theta}{2}\right)} \tag{5.20c}$$

$$\text{Obj.}_{\text{Scour}}\text{(DT)} = \frac{d_s}{y_1} = 0.126 + 0.528\left({Fr_1}^{1.49}\right)\left({L_0}^{0.367}\right)(\theta^{-0.96})({\alpha_0}^{0.243})(2^{-0.609}) \tag{5.21}$$

5.3.1.3 The objective functions of a single-perforated semi-circular deflector

Figure (5.3) presents a schematic layout for the flow deflector of type single perforated semicircular shape.

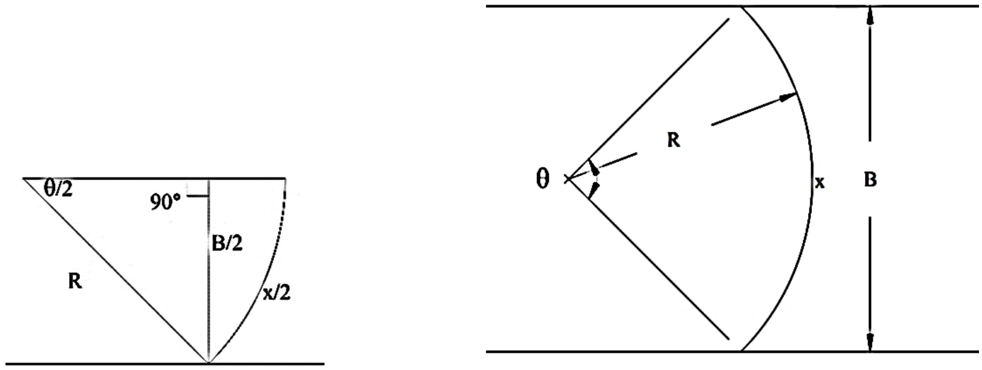

a) Top view.

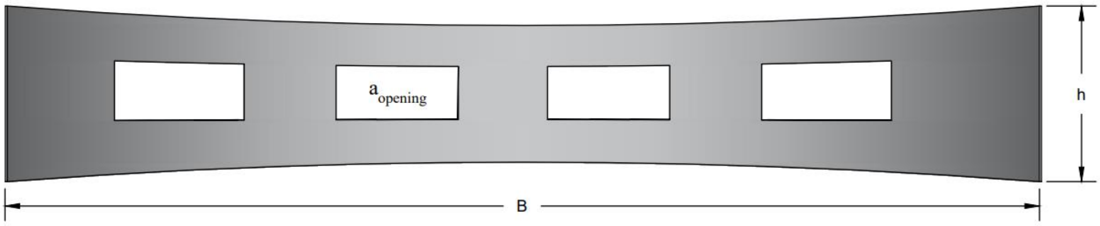

a) Front view

Figure (5. 3): Single perforated semicircular deflector

Obj. (SC) =Surface area of flow deflector =S_{SC}

Obj.$_{Scour}$ (SC) = Maximum relative depth of local scour (d_s/y_1).

∴ The minimum surface area of deflector is :

$$S_{sc} = x\,h - 4\,a_{opening} \tag{5.22a}$$

Since; $x = R\,\theta$

$$\therefore S_{sc} = R\,\theta\,h - 4\,a_{opening} \tag{5.22b}$$

$$\because \sin\frac{\theta}{2} = \frac{B/2}{R} \tag{5.23a}$$

$$\therefore R = \frac{B}{2\sin\frac{\theta}{2}} \tag{5.23b}$$

By sub. eq.(5.23b) into eq.(5.22b);

$$S_{sc} = \frac{B\ \theta\ h}{2\ \sin\frac{\theta}{2}} - 4\ a_{opening} \tag{5.24}$$

$$\because\ \alpha_0 = \frac{4\ a_{opening}}{S_{sc}} \tag{5.25a}$$

$$\therefore 4\ a_{opening} = \alpha_0\ S_{sc} \tag{5.25b}$$

Sub. eq.(5.25b) into eq.(5.24); we get:

$$S_{sc} = \frac{B\ \theta\ h}{2\ \sin\frac{\theta}{2}} - \alpha_0\ S_{sc} \tag{5.26a}$$

Or;

$$S_{sc} = \frac{B\ \theta\ h}{2\ (1+\alpha_0)\sin\frac{\theta}{2}} \tag{5.26b}$$

Thus;

$$\therefore\ \text{Obj.}(SC) = \frac{B\ \theta\ h}{2\ (1+\alpha_0)\sin\frac{\theta}{2}} \tag{5.26c}$$

$$\text{Obj.}_{\text{Scour}}(SC) = \frac{d_s}{y_1} = 0.121 + 0.314 (Fr_1)^{1.735} (L_0)^{0.39} ((\theta)^{2.967} (\alpha_0)^{2.899} + 0.314) \tag{5.27}$$

5.3.1.4 The objective functions of a double-solid semi-circular deflector

Figure (5.4) presents a schematic layout for the flow deflector of type Double solid semicircular shape.

a) Top view

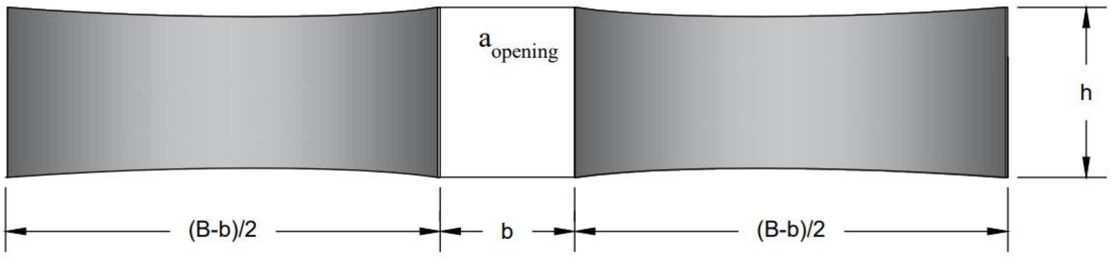

a) Front view

Figure (5. 4):Double solid semicircular deflector

Obj. (DC) =Surface area of flow deflector $=S_{st}$

$Obj._{Scour}$ (DC) = Maximum relative depth of local scour (d_s/y_1).

∴ The minimum surface area of deflector is :

$$S_{dc}=2x\,h \tag{5.28a}$$

Since; $x=R\,\theta$

$$\therefore S_{dc}=2\,R\,\theta\,h \tag{5.28b}$$

$$\because \sin\frac{\theta}{2}=\frac{(B-b)/4}{2^{*}R} \tag{5.29a}$$

$$\therefore R=\frac{(B-b)}{4\sin\frac{\theta}{2}} \tag{5.29b}$$

By sub. eq.(5.29b) into eq.(5.28b);

$$S_{dc}=\frac{(B-b)\,\theta\,h}{2\sin\frac{\theta}{2}} \tag{5.30a}$$

Or;

$$S_{dc}=\frac{B\,\theta\,h}{2\sin\frac{\theta}{2}}-\frac{\theta}{2\sin\frac{\theta}{2}}(b\,h) \tag{5.30b}$$

$$\because \alpha_0=\frac{b\,h}{S_{dc}} \tag{5.31a}$$

$$\therefore b\,h=\alpha_0\,S_{dc} \tag{5.31b}$$

Sub. eq.(5.31b) into eq.(5.30b); we get:

$$S_{dc}=\frac{B\,\theta\,h}{2\sin\frac{\theta}{2}}-\frac{\theta}{2\sin\frac{\theta}{2}}(\alpha_0\,S_{dc}) \tag{5.32a}$$

Or;

$$S_{dc}=\frac{B\,h}{\left(\alpha_0+\frac{2}{\theta}\sin\frac{\theta}{2}\right)} \tag{5.32b}$$

Thus;

$$\therefore \text{Obj.}(DC)=\frac{B\,h}{\left(\alpha_0+\frac{2}{\theta}\sin\frac{\theta}{2}\right)} \tag{5.33}$$

$$\text{Obj.}_{\text{Scour}}(DC)=\frac{d_s}{y_1}=0.121+0.314(Fr_1)^{1.735}(L_0)^{0.39}\left((\theta)^{2.967}(\alpha_0)^{2.899}(2)^{-34}+0.314\right) \tag{5.34}$$

5.3.2 Mathematical Formulating for Constraints

i) The length of stilling basin:

The sufficient stilling basin length constrain is denoted by:

$$L_B=6(y_2-y_1) \tag{5.35}$$

Where y_2 and $y_1$are pre-jump and post-jump depths, respectively.

ii) The upper and lower bonds of design variables

a) $0.3\leq Fr_1\leq 3$

b) $45^{\circ}\leq\theta\leq 135^{\circ}$

c) $0.25\leq L_0\leq 0.75$

d) $0.1\leq\alpha_0\leq 0.4$

e) $0\text{ m}\leq L_B\leq 5\text{ m}$

f) $0.4\text{ m}\leq y_1\leq 0.55\text{ m}$

g) $0.4\text{ m}\leq y_2\leq 2\text{ m}$

h) $Fr_1,\theta,L_0,\alpha_0,L,y_1,y_2,h\geq 0$

iii) The constant variables:

a) h=0.2m

b) B=1m

5.4 Algorithm for Solving Optimization Problem with Multiple Objectives

Weighted summation (WSM) is a well-established and widely used method for solving multi-objective optimization problems (MOPs). The fundamental principle of WSM is to combine the objectives of a MOP into a single weighted sum, where each objective is assigned a weight that reflects its relative importance. The weights are typically determined based on user preferences or problem requirements, and they can be adjusted to achieve different trade-offs between the objectives. WSM is a flexible and efficient approach that has been successfully applied in various fields of engineering. The underlying solution for optimization problem by WSM is presented by the flowchart shown in Figure (5.5). In this study, the MOP's were solved using a MATLAB software R2015a.

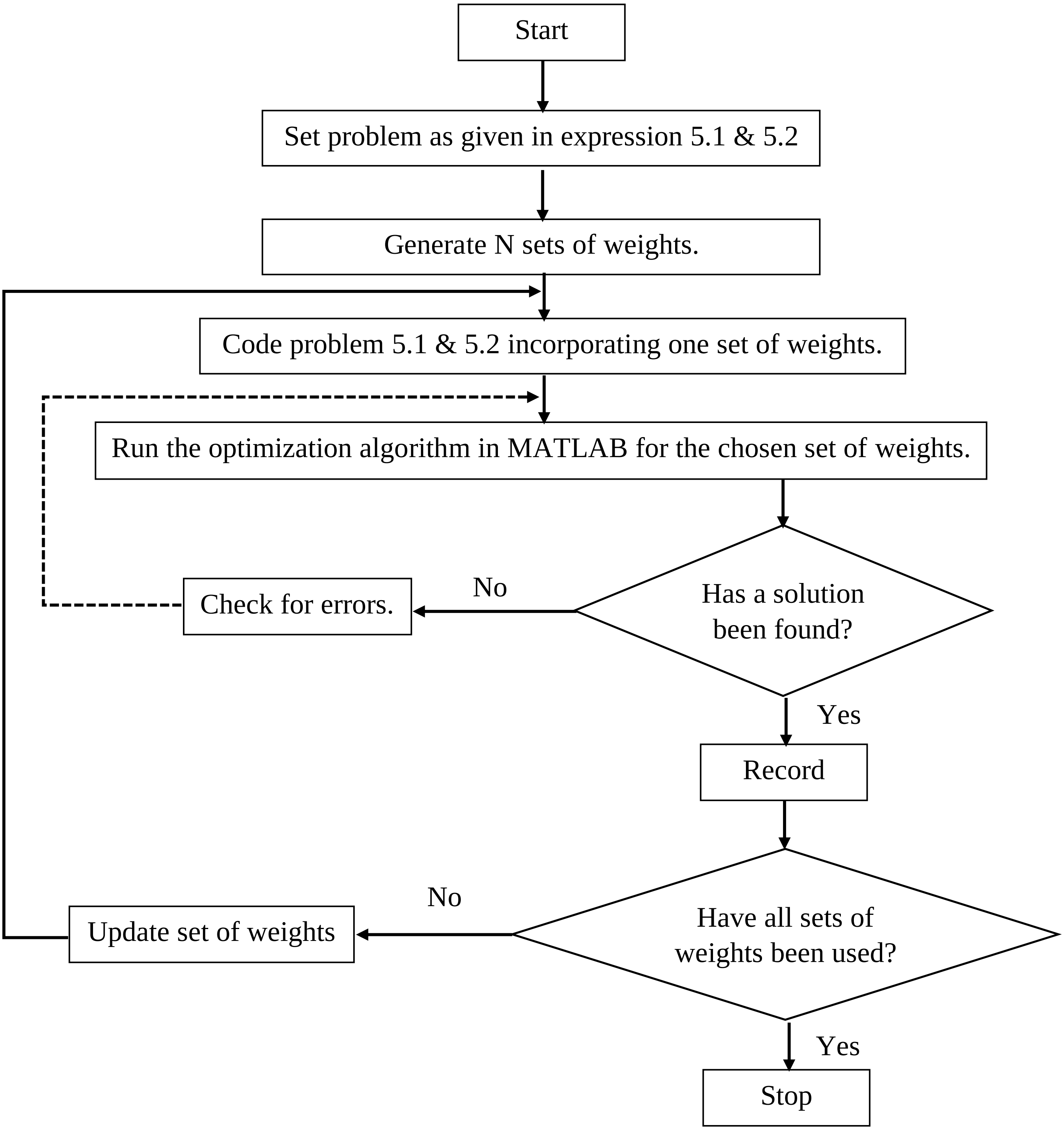

Figure (5. 5): Flowchart for the weighted sum optimization problem.

The MATLAB script for solving the multi-objective problem for single-perforated triangular deflector by using weighted sum method (WSM) is:

```
%Clear the variables from any value
clearvars

%Reduce the number of decimals
format short

% Define the step value of changing weights
k=0.1;

% Create array of all zeros to reduce time of calculations.
w = zeros(1,1/k+1);
fa = zeros(1,1/k+1);
fb = zeros(1,1/k+1);
fab = zeros(1,1/k+1);
xa = zeros(1,1/k+1);
xb = zeros(1,1/k+1);
xc = zeros(1,1/k+1);
xd = zeros(1,1/k+1);
xe = zeros(1,1/k+1);
xf = zeros(1,1/k+1);
xg = zeros(1,1/k+1);

% Create loop.
for i=0:k:1

% Define the weights.
w1= i;
w2= 1-i;
```

```
% Define the objective functions.
%f1 =w1 * Obj. (ST)
%f2 = w2 * Obj.Scour (ST)
f1 = @(x) w1*0.2/((1+x(1))*sin(x(2)/2));
f2 = @(x) w2*(0.126+0.528*x(4)^1.49*x(3)^0.367*x(2)^-0.96*x(1)^0.243);

% Define the constraints
lb = [0.1  0.25*pi  0.25  0.3  0.4    0.4  0 ];
ub = [0.4  0.75*pi  0.75  3    0.55   2    5 ];
A = [];
b = [];
Aeq = [0 0 0 0 -6 6 -1 ];
beq = (0);

% Define the optimization problem
f = @(x) f1(x) + f2(x);
options = optimoptions("fmincon",'Algorithm','interior-point');
[x, fval] = fmincon(f,ub,A,b,Aeq,beq,lb,ub,[],options);

% Display the results within table
j=round(i/k);
w(j+1)=w1;
fa(j+1)=f1(x);
fb(j+1)=f2(x);
fab(j+1)=fval;
xa(j+1)=x(1);
xb(j+1)=x(2);
xc(j+1)=x(3);
xd(j+1)=x(4);
xe(j+1)=x(5);
xf(j+1)=x(6);
```

```
xg(j+1)=x(7);
end
a0=xa';
phi_degree=xb'*180/pi;
L0=xc';
Fr=xd';
y1=xe';
y2=xf';
L=xg';
w1=w';
w2=1-w1;
objective1=fa';            % objective1 = w1*Obj. (ST)
objective2=fb';            % objective2 = w2*Obj.Scour (ST)
objective_total=fab';   % objective_total = w1* Obj. (ST)+ w2*Obj.Scour (ST)
TS = table(w1,w2,objective1,objective2,objective_total,a0,phi_degree
              ,L0,Fr,y1,y2,L)

% Extract the table in excel format
writetable(TS,'optimization_single_triangular_deflector.xlsx','Sheet',1)
```

Repeat the above code for other types of deflectors by changing the surface area of flow deflector equation (Obj. (ST)) and maximum relative depth of local scour ($\text{Obj.}_{\text{Scour}}$ (ST)).

5.5 Optimization-Based Solutions for the Research Problem

The investigation revealed that the single perforated semi-circular flow deflector is the best type regarding most of the research problem objectives and constraints. Consequently, the forthcoming discussion will focus on determining the optimal solution for the design variables associated with this particular type. In order to simplify and make the design of the flow deflectors more applicable, design charts were introduced in s (5.6) to (5.11). These charts incorporate the optimal design variables.

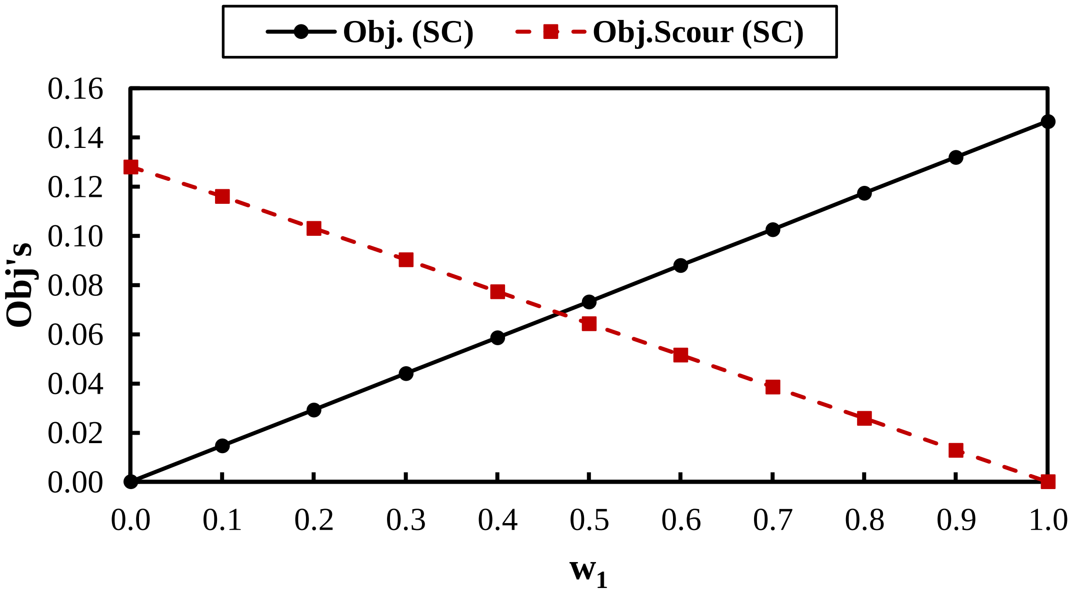

Figure (5. 6): Objective functions vs different values of cost weight for a single perforated semicircle deflector.

Figure (5.6) illustrates the changes in both surface area and relative maximum local scour depth concerning a single perforated semi-circle deflector with respect to the cost weighting factors. As depicted in this , the surface area function Obj. (SC) exhibited an upward trend with increasing w_1, implying higher construction material costs for the flow deflector. Conversely, the Obj.Scour (SC) decreased linearly with rising w_1 until it reached its minimum value when w_1 approached unity. Therefore, this reduces the interaction between cost considerations and design objectives for a perforated semi-circle deflector. It emphasizes the importance of carefully weighing different factors to find an optimal balance between deflector efficiency, material costs, and scour depth for various engineering applications.

Figure (5.7) shows comparison of objective functions at various local scour weight values for a single perforated semicircle deflector. It is evident that this finding reveals identical behavior, as illustrated in Figure (5.7).

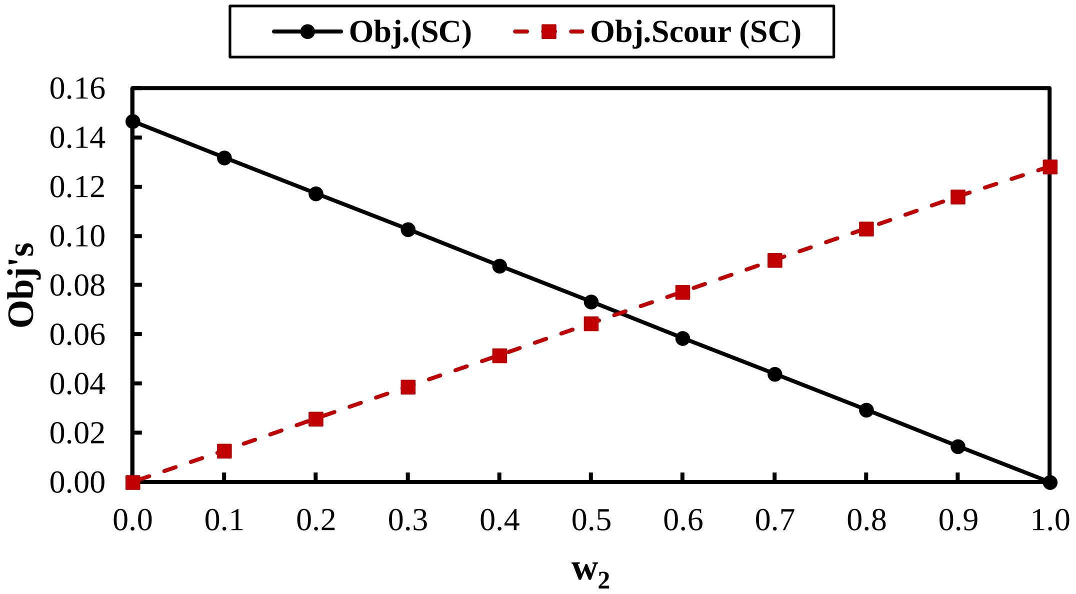

Figure (5. 7): Objective functions vs different values of local scour weight for a single perforated semicircle deflector.

Figures (5.8) and (5.9) show the variations in aspect angle (θ) in (degrees) and passageway ratio (a_0) with different cost weight values for a single perforated semicircle deflector. Based on the findings in Figure (5.8), it becomes evident that initially, with the increase of w_1 up to around 0.25, the aspect angle decreased rapidly, reaching its minimum value. Subsequently, as w_1 continued to rise, the aspect angle exhibited minor fluctuations. An important observation is that the aspect angle range was confined within 44.90° to 45.40°, indicating the sensitivity of the objective function concerning variations in θ's values and its connection to the cost weight factor.

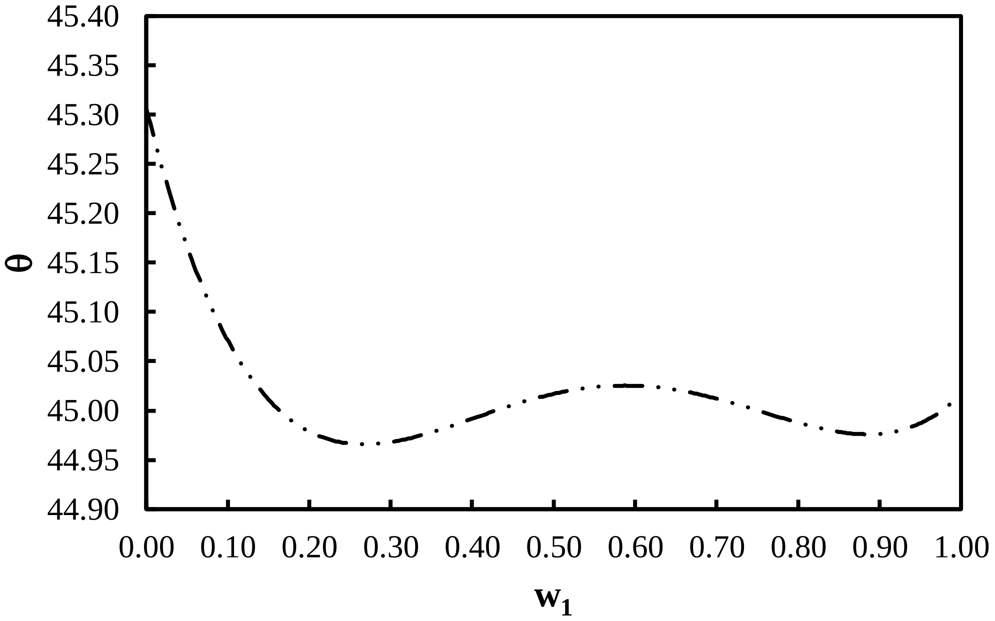

Figure (5. 8): Aspect angle (in degree) vs different values of cost weight for a single perforated semicircle deflector.

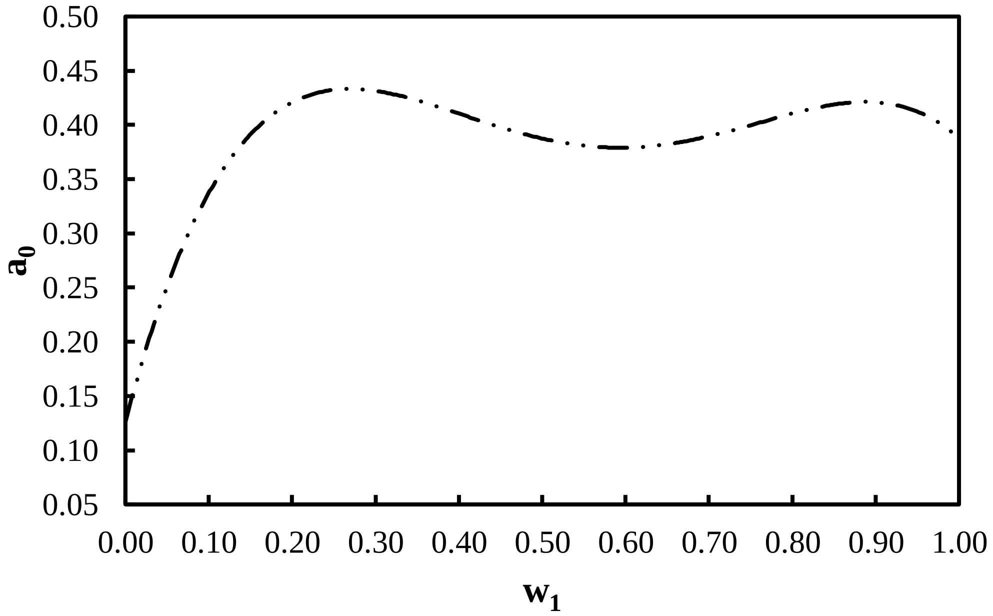

Figure (5. 9): Passageway ratio vs different values of cost weight for a single perforated semicircle deflector.

According to Figure (5.9), the passageway ratio (a_0) showed a rising trend as w_1 increased up to 0.3. Afterward, it exhibited fluctuations with varying w_1, showing both decreases and increases. This observation suggests that when the weight value of the objective function reaches 30%, the area of flow openings within the body of the flow deflector can be expanded by approximately 0.4 to less than 0.45. Essentially, this means that the surface area of the deflector can be reduced, leading to cost savings.

Figures (5.10) and (5.11) present a design chart for the ratio of position (L_0) and Length of stilling basin (L_B) against the cost weight factor for a single perforated semi-circle flow deflector. From results presented in (4.9), as the weight factor values increased, the position ratio (L_0) exhibited fluctuations, ranging from slightly over L_0=0.2 to just above L_0=0.25, until it reached the value w_1 of 0.75. At this point, the position ratio reached its minimum value. Beyond this point, the position ratio increased rapidly, reaching approximately L_0=0.45. This observation can be attributed to the fact that maximizing the importance of the cost function allows for a greater shift in the position of the flow deflector from the regulator. This shift enables a more interaction between hydraulic performance and cost considerations in the problem. Thus, increasing the weight factor values provides better control over the flow deflector's position, leading to improved optimization of both hydraulic performance and cost aspects.

According to the data presented in Figure (5.11), the function representing the length of the stilling basin exhibits a non-linear decrease in the range of 2.7 to 3.5 times the original length (L). This trend can be attributed to the increased significance (weight) assigned to the surface area objective function. The higher weight given to this objective function aims to achieve two main goals: first, to reduce the length of the stilling basin to accommodate the hydraulic jump efficiently, and second, to prevent excessive scour depth beyond the stilling basin. By selecting the surface area objective, the design optimization process emphasizes the importance of achieving these specific hydraulic performance objectives while minimizing the length of the basin.

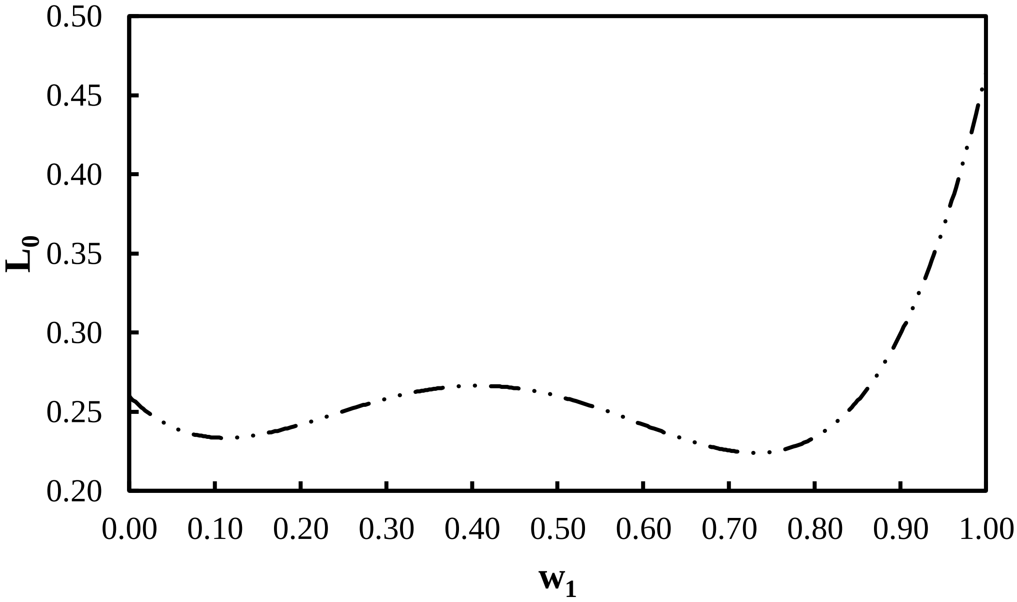

Figure (5. 10): Ratio of position of single perforated semicircle deflector vs different values of cost weight.

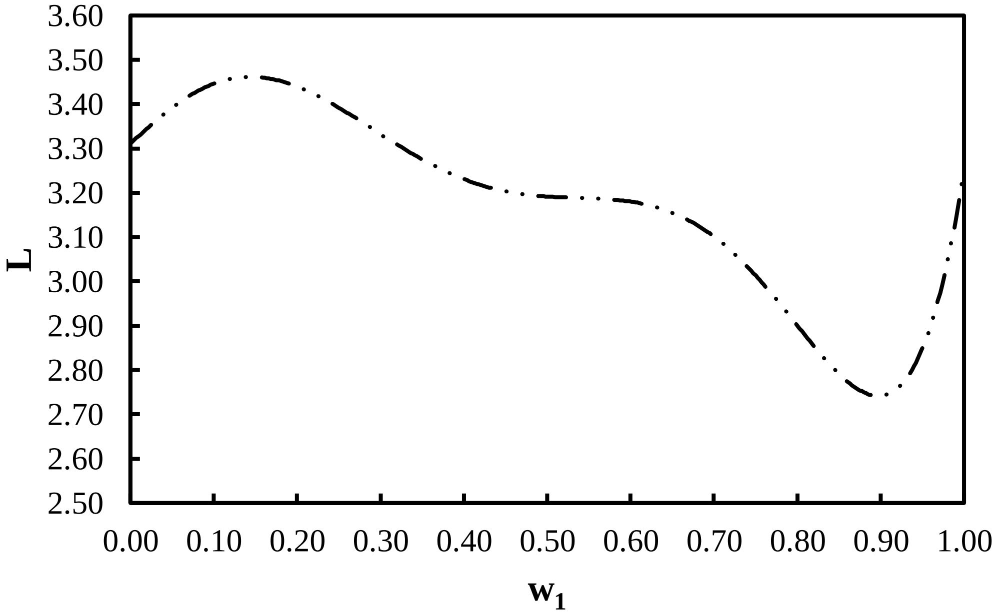

Figure (5. 11): Length of stilling basin vs different values of cost weight for a single perforated semicircle deflector.

The design charts for other types of flow deflectors will be presented in Appendix [C].

5.5.1 Design Problem for Application

Given the following data

Parameter	Unit	Value
discharge, (Q)	m^3/sec	3.85
channel width (B)	m	1.0
inlet water depth, y_1	m	0.55
Froude Number, Fr_1	--	3.014
length of stilling basin, L_B	m	5.0
specific energy for upstream side of the channel, E_1	m	3.05

In Figure (5.12), the stilling basin with a flow deflector is shown, along with the mentioned parameters.

The task involves evaluating the energy dissipation (ΔE) in a conventional stilling basin and various flow deflector shapes. To identify the optimal design for the specific flow conditions, factors such as material, cost, labor, time, and energy dissipation level must be taken into account.

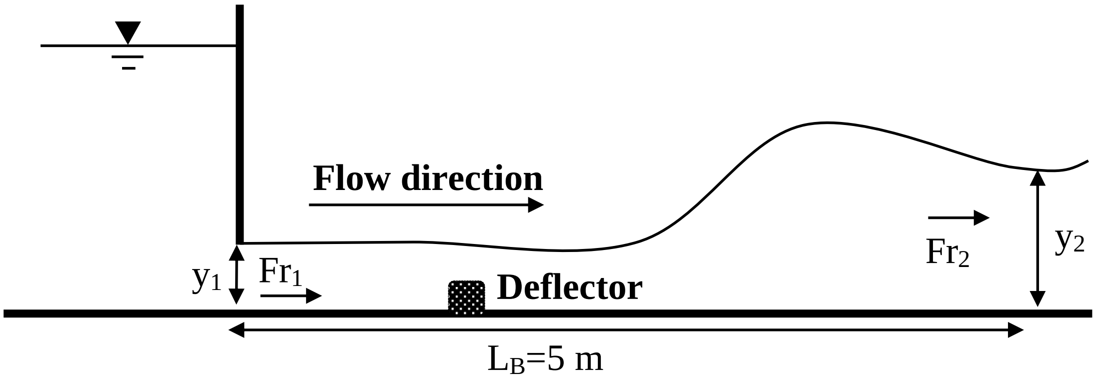

Figure (5. 12): A diagram illustrating a stilling basin equipped with a flow deflector.

Solution Procedure:

In the case of the standard stilling basin

1) For Froude numbers ranging from 2.5 to 4.5, it is advised to utilize Type IV basins, with a specific Froude number of 3.014 ($Fr_1 = 3.014$).
2) From the Figure (5.12), based on $Fr_1 = 3.014$, the ratio of L_B/y_2 is 5.24. Consequently, y_2 can be calculated as 0.95 by dividing 5 by 5.24.
3) The specific energy at downstream portion of channel (E_2) in which:
4) $E_2 = y_2 + v^2/2g$

By substituting the values of (y_1) and (v), we get:

E_2=1.787 m.

5) The expression for ΔE for (IV) stilling basin type is obtained as:

   $\Delta E = E_1 - E_2 = 1.263$ m.

Now, concerning the stilling basin using recommended flow deflectors that minimize the local scour depth.

A) For Single Perforated Triangular Flow Deflector:

1) Based on the results of numerical analysis performed by Flow-3D software, the value of y_2 was obtained to be 1.939 m.
2) The corresponding value for E_2 was determined to be 2.139 m. Consequently, ΔE in the ST model is to be ΔE = 0.91 m.

B) For Double solid Triangular Flow Deflector:

1) Based on the results of numerical analysis performed by Flow-3D software, the value of y_2 was obtained to be 1.848 m.
2) The corresponding value for E_2 was determined to be 2.07 m, accordingly, ΔE = 0.98 m.

C) For Single Perforated Semicircular Flow Deflector:

1) Based on the results of numerical analysis performed by Flow-3D software, the value of y_2 was calculated to be 1.638 m.
2) The resultant value for E_2 was determined to be 1.919 m, therefore, ΔE = 1.13 m.

D) For Double solid Semicircular Flow Deflector:

1) Based on the results of numerical analysis performed by Flow-3D software, the value of y_2 was calculated to be 1.865 m.
2) The resultant value for E_2 was determined to be 2.08 m, consequently, $\Delta E = 0.968$ m.

According to the results presented above, the single perforated semicircular flow deflector proves to be the most satisfactory choice in terms of energy dissipation (ΔE) among the four models. This choice demonstrates the highest level of energy dissipation. To calculate the difference ratio for the IV-type stilling basin;

$$\Delta E\% = \frac{\Delta E_{IV} - \Delta E_{SC}}{\Delta E_{IV}} = \frac{1.263-1.13}{1.263} = 10.5\%$$

The comparison between the IV stilling basin and the stilling basin featuring a single perforated semicircular flow deflector leads to the conclusion that based on the performance of the stilling basin with a single perforated semicircular flow deflector was dissipate energy with an decrease of 10.5%.in addition, it offers cost advantages as it requires construction without the need for complex details like dumping, chute blocks, and end sills. Moreover, without the exclusive concrete required for the IV stilling basin, and no restrictions for location configurations.

Optimal Dimensions of Flow Deflector:

In order to achieve a balance between the economic considerations and hydraulic performance of the stilling basin, the cost-weight factor is predicted through the definition of the intersection point between objective functions Obj.(SC) and Obj.Scour (SC), we can project the coordinates of this point onto the horizontal and vertical axes of Figure (5.6),as shown in Figure (5.13) we get:

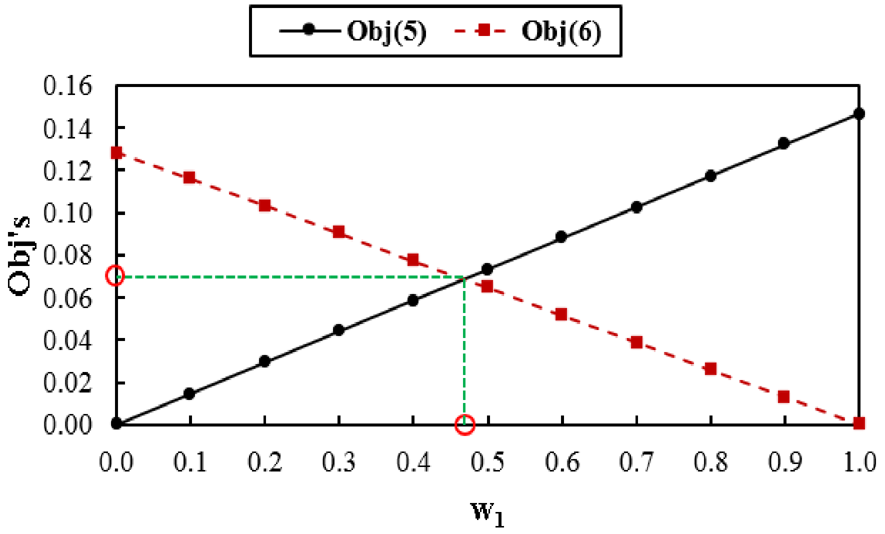

Figure (5. 13): The coordinates of optimal point.

w_1=0.476, and Obj's=0.0645. Thus; from s (4.7) to (4.10), the optimal dimensions (i.e.,θ, a_0, L_0, and L) for single perforated semi-circular flow deflector can be determined for w_1=0.476 as:

$\theta=45.02^o$, $a_0=0.38$, $L_0=0.265$, and $L=3.2$.

From Equations (4.26) and (4.27), respectively; we get:

$$S_{sc}=\frac{B\,\theta\,h}{2\,(1+\alpha_0)\sin\frac{\theta}{2}}$$

$$\frac{d_s}{y_1}=[0.121+0.314(Fr_1)^{1.735}(L_0)^{0.39}((\theta)^{2.967}(\alpha_0)^{2.899}+0.314)]$$

When considering a one-meter width of the stilling basin and substituting the determined values of design variables, the required deflector height is:

$$h=\frac{\left[2\,(1+\alpha_0)\sin\frac{\theta}{2}\right]\times S_{sc}}{(B\,\theta)}=\frac{\left[2\,(1+0.38)\sin\left(\frac{45.02}{2}\right)\right]\times(0.0645)}{\left(1\times\frac{\pi}{180}\times45.02\right)}$$

h=0.087 m

∴ Use h=0.10 m =10.0 cm

The predicted scour depth for these flow conditions is:

$$d_s=y_1\times\left[0.121+0.314(Fr_1)^{1.735}(L_0)^{0.39}\left((\theta)^{2.967}(\alpha_0)^{2.899}+0.314\right)\right]$$

$$\mathbf{d_s=0.55\times\left[0.121+0.314(3.014)^{1.735}(0.265)^{0.39}\left((0.786^{2.967})(0.38^{2.899})+0.314\right)\right]}$$

$$\mathbf{=0.24\ m}$$

The results obtained clearly indicate the optimal length of the stilling basin (L_B) =3.2 m, which was less than the original length (L_B=5.0 m) by 1.8 m. This aspect enhances effectively cost reduction through the optimal hydraulic design of the research problem.

Chapter Six

Conclusions and Recommendations

6.1 Conclusions

This CFD study investigated four flow deflector types and their impact on scour depth and passageway percentage. According to the result of the present study, the conclusion can be summarized as follows:

1. The validation of Flow-3D's ability was carried out by simulating previous laboratory experiments on local scour downstream of a hydraulic structure with a stilling basin, with and without a flow deflector, and comparing the numerical results with the experimental ones. The comparison between the two models reveals that the prediction error range for scour depth was 4.63%.
2. The position and magnitude of maximum local scour depth are significantly affected by the type of flow deflector used. For a single perforated triangular flow deflector with specific parameters (aspect angle of 135 degrees, passageway ratio of 10%, and relative location at 75% of the stilling basin length), the minimum local scour depth is achieved, reducing the maximum scour depth by about 22% and shifting its position away from the channel center. Similarly, when employing a double solid triangular flow deflector with specific parameters (aspect angle of 135 degrees, passageway ratio of 40%, and relative location at 50% of the stilling basin length), the minimum local scour depth is obtained, resulting in a substantial reduction of approximately 71.1% in maximum scour depth, with its position also shifted away from the channel center.
3. Using a single perforated semi-circle flow deflector with specific parameters (aspect angle of 45 degrees, passageway ratio of 20%, and relative location at 50% of the stilling basin length) led to the minimum

local scour depth under these flow conditions. Installing this deflector configuration reduced the maximum local scour depth by around 76.8%, and the primary scour position remained centered in the channel, with less scour near the channel's sides. Similarly, employing a double solid semi-circle flow deflector with specific parameters (passageway ratio of 40% and relative location at 50% of the stilling basin length) resulted in minimal local scour depth. This configuration reduced the maximum local scour depth by approximately 75.7%, with the main scour concentrated along the side of the channel.

4. Weighted Summation (WSM) is a widely-used method in multi-objective optimization. It combines objectives into a weighted sum, allowing trade-offs. The study used MATLAB R2015a for MOPs. Specific parameters for flow deflectors minimized local scour depth. For a single perforated semi-circle deflector, it reduced maximum scour depth by about 76.8%. Design charts simplify flow deflector design, accounting for cost weight factors. As cost weight increased, position and length of the stilling basin changed, optimizing hydraulic performance and cost-efficiency. The optimal length of the stilling basin was 3.2 m, reducing costs while meeting hydraulic objectives.
5. The single perforated semi-circular flow deflector was highly effective in terms of minimizing local scour depth and improving the safety of hydraulic structures. in addition to maximizing the energy dissipation efficiency, the semi-circular deflectors provide a smooth flow transition and reduce turbulence eddies.

6.2 Recommendations

Based on the findings of this study, some key recommendations for further research in this area include:

1. Investigating the effect of other types of flow deflectors on the depth of scour and passageway percentage.
2. Exploring the impact of different bed materials and bed forms on the performance of flow deflectors.
3. Conducting experiments to validate the CFD simulation results and optimize the simulation models.
4. Analyzing the influence of flow conditions, such as flow velocity and water depth, on the effectiveness of flow deflectors.
5. Considering the environmental impact of flow deflectors, such as their effect on aquatic organisms and their ability to trap bed material and pollutants.

These recommendations can help to improve our understanding of flow deflector performance and guide the development of more effective and sustainable designs.

References

AAMIR, M. & AHMAD, Z. 2016. Review of literature on local scour under plane turbulent wall jets. *American Institute of Physics,* 28.

AAMIR, M., AHMAD, Z., PANDEY, M., KHAN, M. A., ALDREES, A. & MOHAMED, A. 2022. The Effect of Rough Rigid Apron on Scour Downstream of Sluice Gates. *Water,* 14**,** 2223.

ABDELHALEEM, F. S. F. 2013. Effect of semi-circular baffle blocks on local scour downstream clear-overfall weirs. *Ain Shams Engineering Journal,* 4**,** 675-684.

ABDULLAH, M., AL-ANSARI, N., ADAMO, N., SISSAKIAN, V. K. & LAUE, J. Floods and Flood Protection in Mesopotamia. 2020a.

ABDULLAH, M., AL-ANSARI, N., ADAMO, N., SISSAKIAN, V. K. & LAUE, J. Irrigation Major Systems on Euphrates River within Mesopotamia. 2020b.

ABDULLAH, M., AL-ANSARI, N. & LAUE, A. J. 2019. Water Resources Projects in Iraq : Barrages. *Journal of Earth Sciences and Geotechnical Engineering,* 9**,** 153-167.

ACHARYA, A. & DUAN, J. G. Three dimensional simulation of flow field around series of spur dikes. World Environmental and Water Resources Congress 2011: Bearing Knowledge for Sustainability, 2011. 2085-2094.

ADDAB, H. F. & AL-SAADI, S. Estimation of Sediment Quantity of the Al-Meshkab Regulator Channel. 2015.

AKAN, A. O. 2006. *Open Channel Hydraulics,* Canada, Elsevier.

AL-ANSARI, N., ADAMO, N. & SISSAKIAN, V. K. Hydrological Characteristics of the Tigris and Euphrates Rivers. 2019.

AL-ANSARI, N., ADAMO, N., SISSAKIAN, V. K., KNUTSSON, S. & LAUE, J. Water Resources of the Euphrates River Catchment. 2018.

AL-HUSSEINI, T. R., JANNA, H. & HAMZA, W. M. 2018. Experimental Study and ANFIS Modeling for Scour Behind Al-Shamiya Barrage. *International Journal of Engineering & Technology*.

AL-SAADI, S., AAL-KHALAF, D. S. K. H. & SHARBA, N. M. 2014. Optimal formula to estimate the quantity of sediment transport upstream of Al- Shamia Barrage. *International journal of engineering research and technology,* 2.

AL-SAADI, S. & ADDAB, H. F. 2011. Development of Empirical Formula for Computing Sediment Loads in Al-Meshkab Regulator Channel. *Jordan Journal of Civil Engineering,* 5.

AL-SAADI, S., AL-MURSHIDI, K. R. & JASEM, H. M. 2013. Investigation of performance of sediment transport formulas based on measured data in Euphrates river, up stream of AL – Abassiya Barrage. *Kufa journal of Engineering,* 4.

AL-THAMIRY, H. A. K., HAIDER, F. A. & AL-SAADI, A. J. J. 2013. Salinity Variation of Euphrates River between Ashshinnafiyah and Assamawa Cities. *The Journal of Engineering,* 19**,** 1442-1466.

AL-ANSARI, N., ALI, A. A. & KNUTSSON, S. 2014. Present Conditions and Future Challenges of Water Resources Problems in Iraq. *Journal of Water Resource and Protection,* 06**,** 1066-1098.

ALI, H. M., GENDY, M. A. E., MIRDAN, A., ALI, A.-A. M. & ABDELHALEEM, F. S. F. 2014. Minimizing downstream scour due to submerged hydraulic jump using corrugated aprons. *Ain Shams Engineering Journal,* 5**,** 1059-1069.

ALSHAMI, A. H. & HUSSEIN, H. A. 2021. Feasibility analysis of mini hydropower and thermal power plants at Hindiya barrage in Iraq. *Ain Shams Engineering Journal*.

ALWAN, H. H. & AL-QAZWINI, M. J. 2011. Operation of Hindiya Barrage Irrigation Using Expert System. *Engineering and Technology Journal,* 29.

ASHOUR, M. A., ALY, T. E. & ABUZAID, T. S. 2016. A NEW EFFICIENT WATER ENERGY DISSIPATOR FOR IMPROVING THE IRRIGATION WATER QUALITY. *International Water Technology Journal* 6**,** 195-205.

ASTM D422-63 2007. Standard Test Method for Particle-Size Analysis of Soils.

BAJKOWSKI, S. 2007. Proste kryteria oceny bezpieczeństwa jazów na rzekach nizinnych. *Infrastruktura i Ekologia Terenów Wiejskich*.

BAYON, A., VALERO, D., GARCÍA-BARTUAL, R. & LÓPEZ-JIMÉNEZ, P. A. 2016. Performance assessment of OpenFOAM and

FLOW-3D in the numerical modeling of a low Reynolds number hydraulic jump. *Environmental modelling & software,* 80**,** 322-335.

BIRON, P. M., ROBSON, C., LAPOINTE, M. F. & GASKIN, S. J. 2005. Three-dimensional flow dynamics around deflectors. *River Research and Applications,* 21.

BLAISDELL, F. W. 1948. Development and hydraulic design, Saint Anthony Falls stilling basin. *Transactions of the American Society of Civil Engineers,* 113**,** 483-520.

BOMOLA, A. A. Temporal and spatial changes in water quality of the Euphrates river - Iraq. 2011.

BREUSERS, H. N. C. 1966. Conformity and time scale in two-dimensional local scour. Poona, India: Hydraulic Research Laboratory.

CHANSON, H. 2015. *Energy dissipation in hydraulic structures*, CRC Press.

DARDEER, M. A. 2022. ASSESSING THE IMPACT OF SEMI-CIRCULAR BAFFLE BLOCKS ON SCOUR DOWNSTREAM SLUICE GATES *Journal of Al-Azhar University Engineering Sector,* 17**,** 172 -188.

DONG, Z., WANG, J., VETSCH, D. F., BOES, R. M. & TAN, G. 2019. Numerical Simulation of Air-Water Two-Phase Flow on Stepped Spillways behind X-Shaped Flaring Gate Piers under Very High Unit Discharge. *Water,* 11**,** 1956.

DUAN, J. G. & NANDA, S. 2006. Two-dimensional depth-averaged model simulation of suspended sediment concentration distribution in a groyne field. *Journal of Hydrology,* 327**,** 426-437.

EL-MASRY & SARHAN 2000. MINIMIZATION OF SCOUR DOWNSTREAM HEADING-UP STRUCTURES USING A SINGLE LINE OF ANGLE BAFFLES. *Engng. Res. Jour*

Helwan University, Faculty ofEngng , Mataria Cairo, 69**,** 192 - 207.

EVANS, R., SOPPE, R., SALEH, R. O. & ABBAS, A. 2013. Report B1. 4 : Water and salt trends and balances for the Mesopotamian plain. Beirut, Lebanon: International Center for Agricultural Research in the Dry Areas (ICARDA).

FLOW SCIENCE, I. 2009. *FLOW-3D, V11.2,* USA, Flow Science, Inc.

GHADERI, A., ABBASI, S., ABRAHAM, J. & AZAMATHULLA, H. M. 2020. Efficiency of trapezoidal labyrinth shaped stepped spillways. *Flow measurement and instrumentation,* 72**,** 101711.

HADI, Z. N. & ALMANSORI, N. J. H. 2021. Estimation of Manning coefficient for the section between Al-Hindiya barrage and Al-Kufa barrage utilizing HEC-RAS. *Materials Today: Proceedings*.

HELAL, E. E.-D. Y. E.-A. 2014. Minimizing scour downstream of hydraulic structures using single line of floor water jets. *Ain Shams Engineering Journal,* 5**,** 17-28.

HELAL, E. Y., NASSRALLA, T. H. & ABDELAZIZ, A. A. 2013. Minimizing of scour downstream hydraulic structures using sills *NTERNATIONAL JOURNAL OF CIVIL AND STRUCTURAL ENGINEERING* 3.

HO, D. & RIDDETTE, K. 2010. Application of computational fluid dynamics to evaluate hydraulic performance of spillways in Australia. *Australian Journal of Civil Engineering,* 6**,** 81-104.

HOBI, M. H. 2014. PREDICATION OF SEDIMENT TRANSPORT In Al-ABBASYIA BARRAGE USING THE INVERSE MONITORING METHOD. *Kufa journal of Engineering,* 5.

HOFFMANS, G. J. C. M. 1990. Concentration and fow velocity measurements in a local scour hole. Faculty of Civil Engineering, Hydraulic and Geotechnical Engineering Division, Delft University of Technology: Delft.

HOFFMANS, G. J. C. M. & VERHEIJ, H. J. 2022. *Scour Manual : Current-Related Erosion,* London, Taylor and Francis,.

HOMMADI, A. H. & DAHIR, F. M. 2018. Predicting Sediment Accumulation in Euphrates River: A Case Study of the Upstream of Al-Hindiya Barrage, Iraq. *Indian Journal of Natural Sciences,* 9.

HOMMADI, A. H., DAHIR, F. M. & AL-HEETIMI, O. T. 2018. Evaluation of Discharge Coefficient in Hilla Head Regulator by Using Multi Parameters. *Indian Journal of Natural Sciences,* 9.

IBRAHIM, A. A. & NEGM, A. M. EFFECT OF HEIGHT OF CURVED DEFLECTOR WALL ON MAXIMUM NEAR-BED-VELOCITY DOWNSTREAM OF MULTI-VENTS REGULATORS. 7th ISE & 8th HIC 2009 Chile.

INAD, R. S., KAMEL, A. H. & ALBORESHA, R. S. 2022. Sediment transport treatment upstream barrages. *Design Engineering***,** 3898-3913.

ISSA, I. E., AL-ANSARI, N., SHERWANY, G. & KNUTSSON, S. 2014. Expected Future of Water Resources within Tigris-Euphrates Rivers Basin, Iraq. *Journal of Water Resource and Protection,* 6**,** 421-432.

JASI, N. 2020. ESTIMATION OF SEDIMENTS TRANSPORT OF EUPHRATES RIVER BRANCHES WITHIN BABYLON CITY USING A MATHEMATICAL MODEL. *Journal of Engineering Science and Technology,* 14**,** 2163 - 2177.

JICA 2016. Data collection survey on water resource management and agriculture irrigation in the Republic of Iraq : final report.

KAMEL, A. H., KHALIL, W. H. & AL-DAMOOK, A. 2022. Estimation of Hydropower Harvesting from the Hydraulic Structures on Rivers: Ramadi Barrage, Iraq as a Case Study. *Iraqi Journal of Civil Engineering*.

KANG, J.-G. 2016. Effective Analysis by Arrangement of Multi-Baffle at Weir Downstream. *Engineering,* 08**,** 720-726.

KANG, J.-G. 2017. An Experimental Study on the Dissipation Effect of a Baffle Downstream of a Weir. *Engineering,* 9**,** 937-949.

KHALIFEHEI, K., SADEGHI ASKARI, M. & AZAMATHULLA, H. 2022. Experimental investigation of energy dissipation on flip buckets with triangular deflectors. *ISH Journal of Hydraulic Engineering,* 28**,** 292-298.

KHASSAF, S. I. 2014. A STUDY OF SCOUR AROUND AL-KUFA BRIDGE PIERS. *Kufa journal of Engineering,* 1.

KHAYYUN, T. S. 2020. Prediction of the Suspended Transport Rate of River Reach. *Journal of Southwest Jiaotong University*.

KHLIF, T. H., AL-SAHAF, N. A. H. & JASSIM, H. M. EVALUATION THE HYDRAULIC CHARACTERISTIC OF AL-KUFA DAM. Proceedings of The IIER International Conference, 24th-25th August 2018 Cape Town, South Africa.

KUMCU, S. Y. & ISPIR, K. 2022. Experimental and numerical modeling of various energy dissipater designs in chute channels. *Applied Water Science,* 12**,** 266.

KURDISTANI, S. M. & PAGLIARA, S. 2015, Scour Characteristics Downstream of Grade-Control Structures: Log-Vane and Log-Deflectors Comparison.

LI, S. & ZHANG, J. 2018. Numerical Investigation on the Hydraulic Properties of the Skimming Flow over Pooled Stepped Spillway. *Water,* 10.

MELVILLE, B. W. & SUTHERLAND, A. J. 1988. DESIGN METHOD FOR LOCAL SCOUR AT BRIDGE PIERS. *Journal of Hydraulic Engineering,* 114**,** 1210-1226.

MOSTAFA, G. M., NEGM, A. M., OWAIS, T. M. & SHAHEEN, M. EFFECT OF GUIDEWALL POSITION ON LOCAL SCOUR DOWNSTREAM O STILLING BASINS IN TRAPEZOIDAL CHANNELS Proc. of 6th Int. Conference on Environmental Hydrology and 1st symp. on Coastal and Port Engineering, 28-30 Sep. 2009 Cairo. ASCE-ES.

NASRALLA, T. H. 2022. Experimental and numerical investigation of scour downstream contracted spillways. *Journal of Water and Land Development***,** 53-59-53-59.

NEGM, A. M., ABDEL-AAL, G. M., ELFIKY, M. M., MOHAMED, Y. A.-R. I. & PROFESSORS. OPTIMAL POSITION OF CURVED DEFLECTOR TO MINIMIZE SCOUR DOWNSTREAM MULTI-VENTS REGULATORS. 2008.

NEGM, A. M., ABDEL-AAL, G. M., ELFIKY, M. M. & MOHAMED, Y. A. 2009a. OPTIMAL WATERWAY PASSAGE IN SUBMERGED CURVED DEFLECTOR FOR MINIMIZATION OF LOCAL SCOUR. *Thirteenth International Water Technology Conference, IWTC 13 2009, Hurghada, gypt*.

NEGM, A. M., ABDELAAL, G. M., ELFIKY, M. I. & ABDALLAH, Y. M. 2009b. EFFECT OF WIDTH AND ORIENTATION OF CURVED HOLLOWED DEFLECTOR ON MAXIMUM SCOUR DEPTH DOWNSTREAM OF MULTI-VENTS REGULATORS *Proc. of 6th Int. Conference on Environmental Hydrology and 1st symp. on Coastal and Port Engineering, 28-30 Sep. 2009, ASCE-ES, Cairo*.

OBAED, I. H., AL-SALIM, N. H. A. & AL-FATLAWY, T. J. 2016. Experimental study for hydraulic characteristics of flow over compound regular notches. *Journal of Babylon University***,** 38-55.

OBEAD, I. H. & KHODAIER, A. A. 2017. FLOOD ROUTING FOR A SPECIFIC ORIENTATION OF PLANNED DEVELOPMENTS

FOR AL-SHAMIYA RIVER IN IRAQ AS CASE STUDY. *Journal of Civil Engineering and Technology (JCIET),* 4**,** 1–12.

PADHI, E. 2022. *A Novel Hybrid Approach For The Design Of Stilling Basin To Counter The Downstream Local Scour* [Online]. 2022. Available: https://civil.snu.edu.in/research/projects/novel-hybrid-approach-design-stilling-basin-counter-downstream-local-scour [Accessed 2023].

PAGLIARA, S., HASSANABADI, L. S. & KURDISTANI, S. M. 2015. Clear Water Scour Downstream of Log Deflectors in Horizontal Channels. *Journal of Irrigation and Drainage Engineering-asce,* 141**,** 04015007-04015007.

PAGLIARA, S., PALERMO, M. & CARNACINA, I. 2009. Scour and hydraulic jump downstream of block ramps in expanding stilling basins. *Journal of Hydraulic Research,* 47**,** 503-511.

PARK, S. W., HWANG, J. H. & AHN, J. 2019. Physical Modeling of Spatial and Temporal Development of Local Scour at the Downstream of Bed Protection for Low Froude Number *water,* 11**,** 1-12.

PIZARRO, A., MANFREDA, S. & TUBALDI, E. 2020. The Science behind Scour at Bridge Foundations: A Review. *water,* 12**,** 1-26.

POPE, S. B. 2001. *Turbulent Flows,* Meas, Sci. Technol.

POURSHAHBAZ, H., ABBASI, S., PANDEY, M., PU, J. H., TAGHVAEI, P. & TOFANGDAR, N. 2022. Morphology and hydrodynamics numerical simulation around groynes. *ISH Journal of Hydraulic Engineering,* 28**,** 53-61.

PRADHAN, P., TINGSANCHALI, T. & SHRESTHA, S. 2020. Evaluation of Soil and Water Assessment Tool and Artificial Neural Network models for hydrologic simulation in different climatic regions of Asia. *Science of the Total Environment,* 701**,** 134308.

PU, J. H. 2015. Turbulence modelling of shallow water flows using Kolmogorov approach. *Computers & Fluids,* 115**,** 66-74.

PU, J. H., HUANG, Y., SHAO, S. & HUSSAIN, K. 2016. Three-gorges dam fine sediment pollutant transport: turbulence SPH model simu lation of multi-fluid flows. *J. Appl. Fluid Mech,* 9.

PU, J. H. & LIM, S. Y. 2014. Efficient numerical computation and experimental study of temporally long equilibrium scour develop ment around abutment. *Environ. Fluid Mech,* 14**,** 69-86.

PU, J. H., SHAO, S. & HUANG, Y. 2014. “Numerical and experimental turbulence studies on shallow open channel flows. *J. Hydro Environ. Res,* 8**,** 9–19.

RASHED, R. H., EL-MASRY, A. & ABDELGAWAD, H. 2022. Effect of Hollow Semi-Circular Baffles Arrangement on Local Scour Downstream Hydraulic Structures *MANSOURA ENGINEERING JOURNAL,* 47.

RECLAMATION, U. S. B. O. 1987. *Design of small dams,* US Department of the Interior, Bureau of Reclamation.

ROBERSON, J. A., CASSIDY, J. J. & CHAUDHRY, M. H. 1998. *Hydraulic engineering,* John Wiley & Sons.

S. MAATOOQ, J., ALWASH, H. H. & MUHAMMAD AL-KHAFAJI, H. 2015. Analysis Seepage and Uplift Pressure for Al-Shamiya Barrage South of Iraq. *Engineering and Technology Journal*.

SALEH, L., MAJEED, S. A. A.-D. & ALGRETAWEE, H. 2021. Analysis of the Euphrates River’s movement within Al-Hindiya, Karbala, relative to steady flow conditions using the HEC-RAS model. *IOP Conference Series: Materials Science and Engineering,* 1067.

SALEH, O. K., NEGM, A. M., WAHEED-ELDIN, O. S. & AHMAD, N. G. EFFECT OF END SILL ON SCOUR CHARACTERISTICS OWNSTREAM OF SUDDEN EXPANDING STILLING BASINS. 2004 Alexandria, Egypt. Eighth International Water Technology Conference, IWTC8.

SAMAD, H. A., HELAL, Y. E., IBRAHIM, S. A. & SOBEIH, M. F. MINIMIZING OF SCOUR DOWNSTREAM HYDRAULIC STRUCTURES USING SEMI – CIRCULAR SILL. 2012.

SARFARAZ, M. V. & ATTARI, J. Numerical Simulation of Uniform Flow Region over a Steeply Sloping Stepped Spillway. 6th National Congress on Civil Engineering, April 26-27 2011 Semnan University,Semnan, Iran.

SHAREEF, M. & ABDULRAZZAQ, D. G. 2021. River Flood Modelling For Flooding Risk Mitigation in Iraq. *Civil Engineering Journal*.

SOHRABI, M., KESHAVARZI, A. & JAVAN, M. 2018. Impact of bed sill shapes on scour protection in river bed and banks. *International Journal of River Basin Management*, 17**,** 277 - 287.

USBR 1997. *Water Measurement Manual*

VAN DER MEULEN, T. & VINJÉ, J. J. Three-dimensional local scour in noncohesive sediments. 1975 Sao Paulo, Brasil (also Delft Hydraulics, Delft, Publication 180). Proceedings of the 16th LAHR-Congress,.

WEI, G., BRETHOUR, J., GRÜNZNER, M. & BURNHAM, J. 2014. The sedimentation scour model in FLOW-3D. *Flow Sci. Rep*, 3–14 Santa Fe, NM: Flow Science.

XIE, L., ZHU, Y., LI, H., LI, Y., YANG, Y. & SU, T.-C. 2020. Local Scour Near Flexible Flow Deflectors. *Water,* 12**,** 153.

XIE, Z. 2011 *Theoretical and numerical research on sediment transport in pressurised flow conditions,* Lincoln, University of Nebraska

YAKHOT, V., ORSZAG, S., THANGAM, S., GATSKI, T. & SPEZIALE, C. 1992. Development of turbulence models for shear flows by a double expansion technique *Physics of Fluids A: Fluid Dynamics,* 4**,** 1510–1520.

YU, D., CHOI, S. U. & WOO, H. 2007. An experimental study of local Scour around V-deflector over fine-grained bed. *Water International,* 32**,** 786 - 797.

ZANKE, U. 1978. Zusammenhänge zwischen Strömung und Sedimenttransport, Teil 1: Berechnung des Sedimenttransportes, -allgemeiner Fall-, Teil 2: Berechnung des Sedimenttransportes hinter befestigten Sohlenstrecken, -Sonderfall zweidimensionaler Kolk-. Mitteilungen des Franzius-Instituts der TU Hannover, Heft 47, 48.

ZHANG, W., WANG, J., ZHOU, C., DONG, Z. & ZHOU, Z. E. 2018. Numerical simulation of hydraulic characteristics in a vortex drop shaft. *Water,* 10.

ZHANG, W., WANG, L., MELVILLE, B. W., GUAN, D., WHITTAKER, C. N. & SHAMSELDIN, A. Y. 2021. Characteristics of the flow field within a developing scour hole at a submerged weir. *Journal of Hydraulic Research,* 60**,** 283-294.

Appendix [A]

Equations for Laboratory Flow Deflector Dimensions and Shapes

For the single perforated triangular flow deflector shape, the following equations were used to determine the deflector dimensions. In Figure (A.1), all the dimensions in meters and all variables required in the equations were specified.

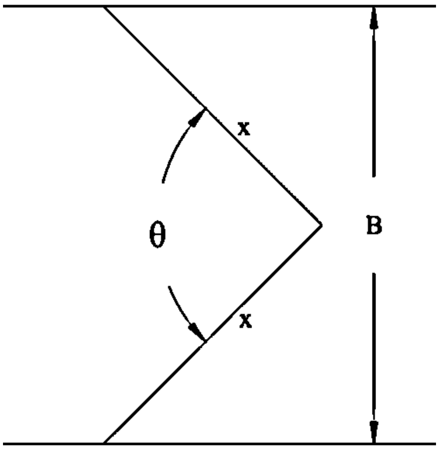

(a) Top view of single perforated triangular flow deflector**.**

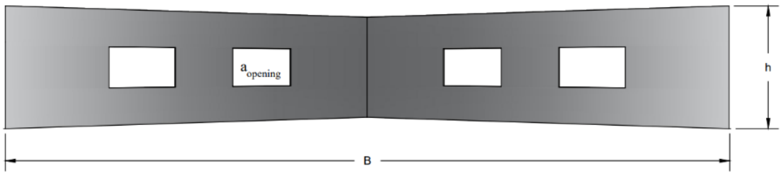

(b) Front view of single perforated triangular flow deflector.

Figure (A.1): Schematic representation for the flow deflector of single perforated triangular shape.

From;

$$B=\sqrt{2}x\sqrt{B-\cos(\theta)}$$

$$\because\ B=1$$

$$\therefore\ x=\frac{1}{\sqrt{2}\sqrt{1-\cos(\theta)}} \qquad \text{(A. 1)}$$

Since;

$$\alpha_0=\frac{a_{opening}}{S_{ST}}$$

Or;

$$\alpha_0=\frac{a_{opening}}{2(xh\text{-}2a_{opening})}=\frac{a_{opening}}{2(x\,0.2\text{-}2a_{opening})}$$

$$2\alpha_0(x\,0.2\text{-}2a_{opening})=a_{opening}$$

Thus;

$$a_{opening}=\frac{0.4\alpha_0}{1+4\alpha_0}x$$

Or;

$$a_{opening}=\left(\frac{0.4\alpha_0}{1+4\alpha_0}\right)\left(\frac{1}{\sqrt{2}\sqrt{1\text{-}\cos(\theta)}}\right) \qquad \text{(A. 2)}$$

Note;

$$\left(\frac{width\ of\ opening}{high\ of\ opening}\right)_{for\ single\ perforated\ triangular\ flow\ deflector.}$$

$$\simeq\left(\frac{width\ of\ opening}{high\ of\ opening}\right)_{for\ double\ solid\ triangular\ flow\ deflector.}$$

Similarly, for the single perforated semi-circular flow deflector shape, the following equations were used to determine the deflector dimensions. In Figure (A.2), all the dimensions and variables required in the equations were specified. all the dimensions in meters and all variables required in the equations were specified.

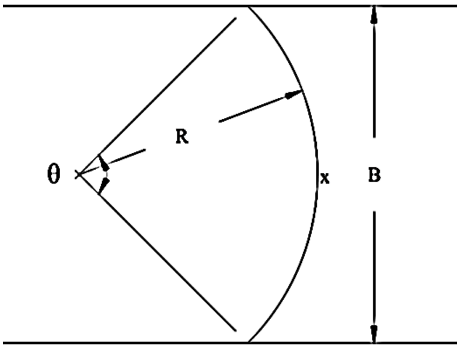

(a) Top view of single perforated semi-circular flow deflector.

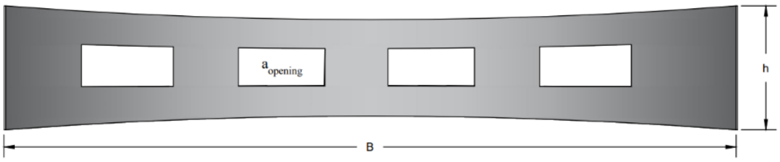

(b) Front view of single perforated semi-circular flow deflector.

Figure (A. 2): Schematic representation for the flow deflector of single perforated semi-circular flow deflector.

From;

$$B=2R\sin\left(\frac{\theta}{2}\right)$$

and;

$$R=\frac{x}{\theta}$$

$$B=1$$

$$\therefore 1=2\frac{x}{\theta}\sin\left(\frac{\theta}{2}\right)$$

Thus;

$$x=\frac{\theta}{2\sin\left(\frac{\theta}{2}\right)} \qquad \text{(A. 3)}$$

Since;

$$\alpha_0=\frac{a_{opening}}{S_{SC}}$$

Or;

$$\alpha_0=\frac{a_{opening}}{hR\theta\text{-}4a_{opening}}=\frac{a_{opening}}{0.2\frac{x}{\theta}\theta\text{-}4a_{opening}}$$

$$\alpha_0\left(0.2x\text{-}4a_{opening}\right)=a_{opening}$$

Thus;

$$a_{opening}=\frac{0.2\alpha_0}{1+4\alpha_0}x$$

Or;

$$a_{opening}=\left(\frac{0.4\alpha_0}{1+4\alpha_0}\right)\left(\frac{\theta}{4\sin\left(\frac{\theta}{2}\right)}\right) \qquad \text{(A. 4)}$$

Note;

$$\left(\frac{width\ of\ opening}{high\ of\ opening}\right)_{for\ single\ perforated\ semi-circular\ flow\ deflector.}$$

$$\simeq\left(\frac{width\ of\ opening}{high\ of\ opening}\right)_{for\ double\ solid\ semi-circular\ flow\ deflector.}$$

Appendix [B]

3D Scour Profile for Flow Deflector in Varying Flows

Figure (B.1): Picture for single perforated triangular flow deflector with design parameter (θ=120^o, L_o=90%, α_o=14%) during a laboratory experiment for Q=0.0154m^3/s.

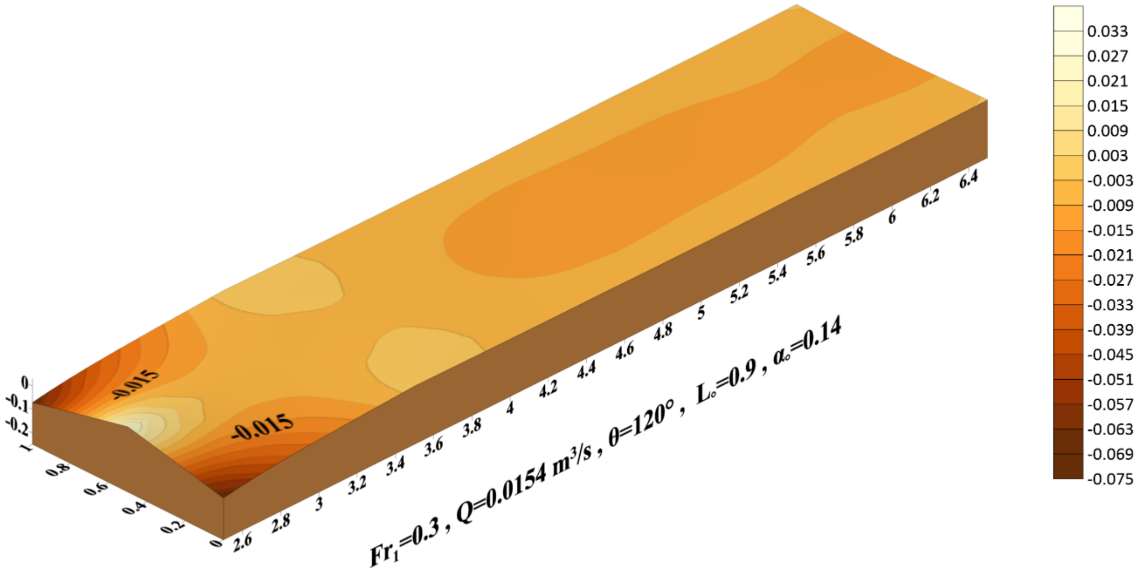

Figure (B.2): 3D scour profile for single perforated triangular flow deflector with design parameter (θ=120^o, L_o=90%, α_o=14%) during a laboratory experiment, all dimensions in (m).

Figure (B.3): Picture for single perforated triangular flow deflector with design parameter (θ=120^o, L_o=90%, α_o=14%) during a laboratory experiment for Q=0.03m^3/s.

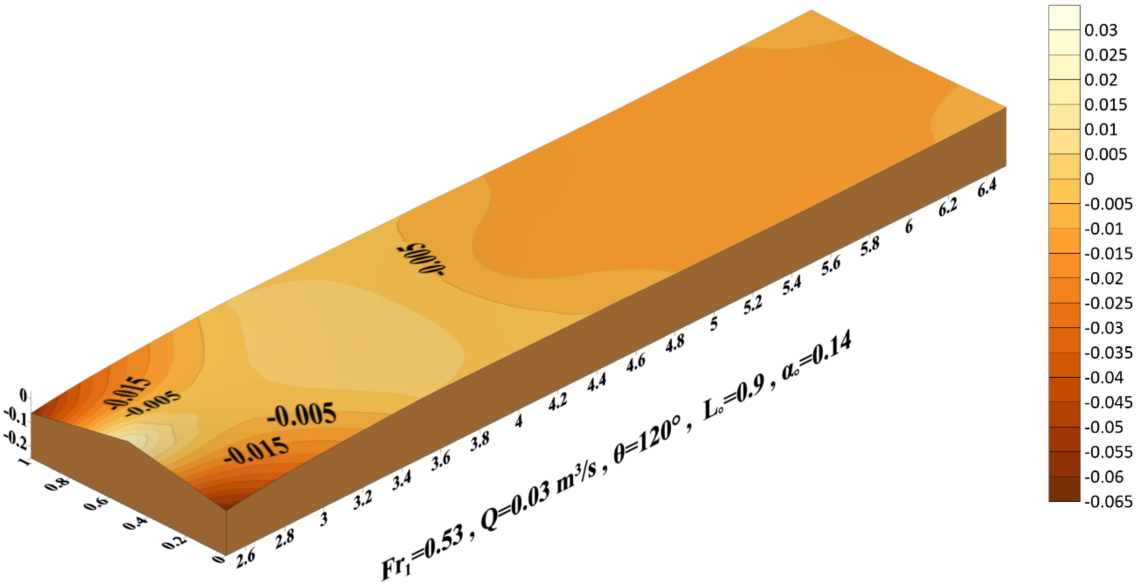

Figure (B.4): 3D scour profile for single perforated triangular flow deflector with design parameter (θ=120^o, L_o=90%, α_o=14%) during a laboratory experiment, all dimensions in (m).

Figure (B.5): Picture for single perforated triangular flow deflector with design parameter (θ=120^o, L_o=90%, α_o=14%) during a laboratory experiment for Q=0.044m^3/s.

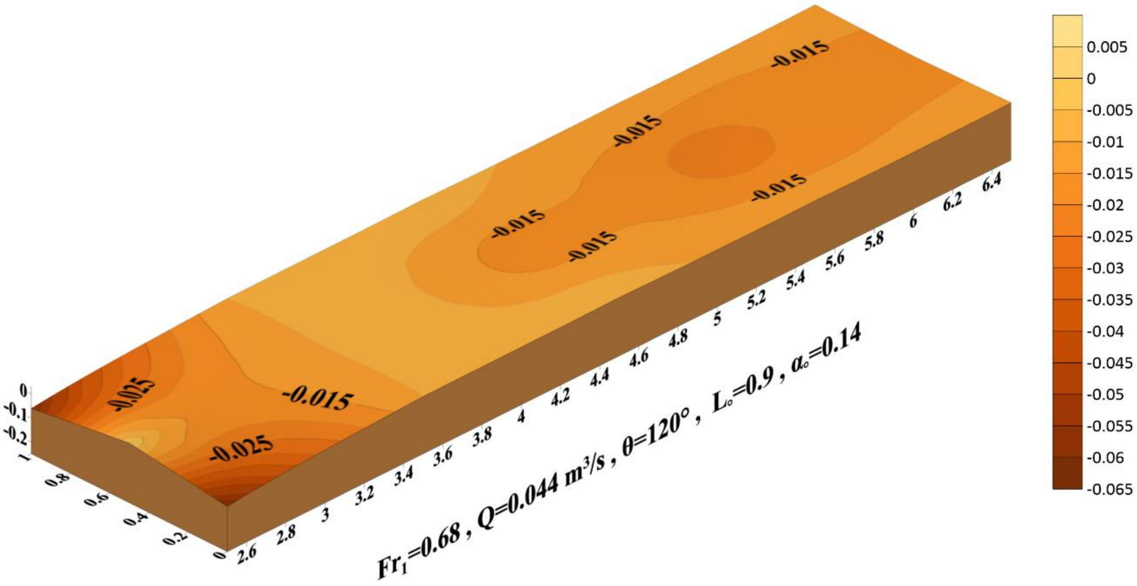

Figure (B.6): 3D scour profile for single perforated triangular flow deflector with design parameter (θ=120^o, L_o=90%, α_o=14%) during a laboratory experiment, all dimensions in (m).

Figure (B.7): Picture for single perforated semicircular flow deflector with design parameter ($\theta=120^o$, $L_o=90\%$, $\alpha_o=14\%$) during a laboratory experiment for $Q=0.0154 m^3/s$.

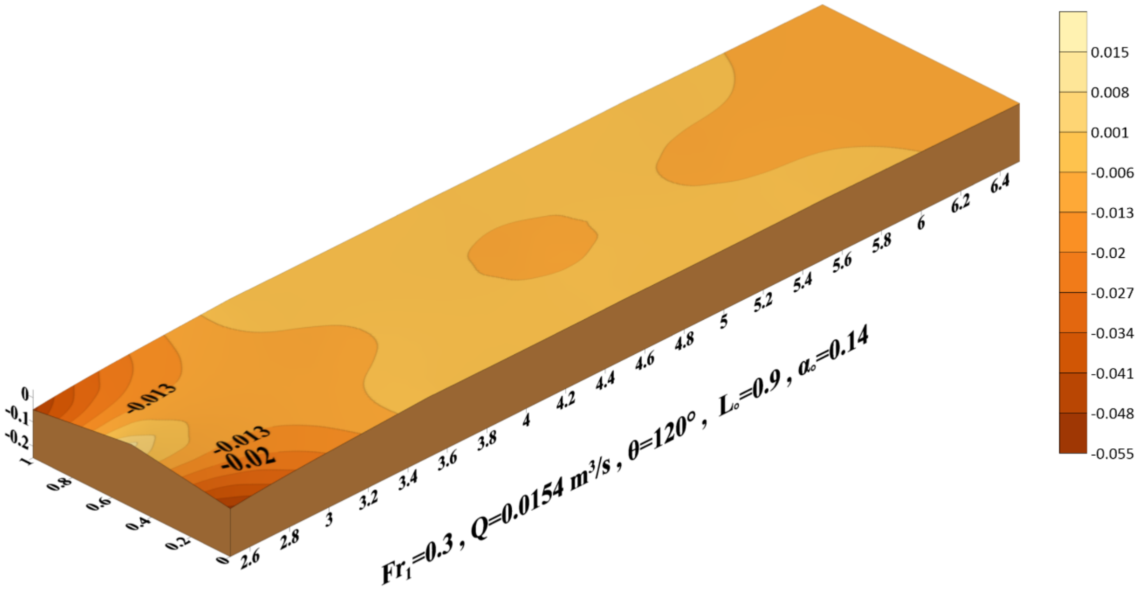

Figure (B.8): 3D scour profile for single perforated semicircular flow deflector with design parameter ($\theta=120^o$, $L_o=90\%$, $\alpha_o=14\%$) during a laboratory experiment, all dimensions in (m).

Figure (B.9): Picture for single perforated semicircular flow deflector with design parameter ($\theta=120^o$, $L_o=90\%$, $\alpha_o=14\%$) during a laboratory experiment for $Q=0.03 m^3/s$.

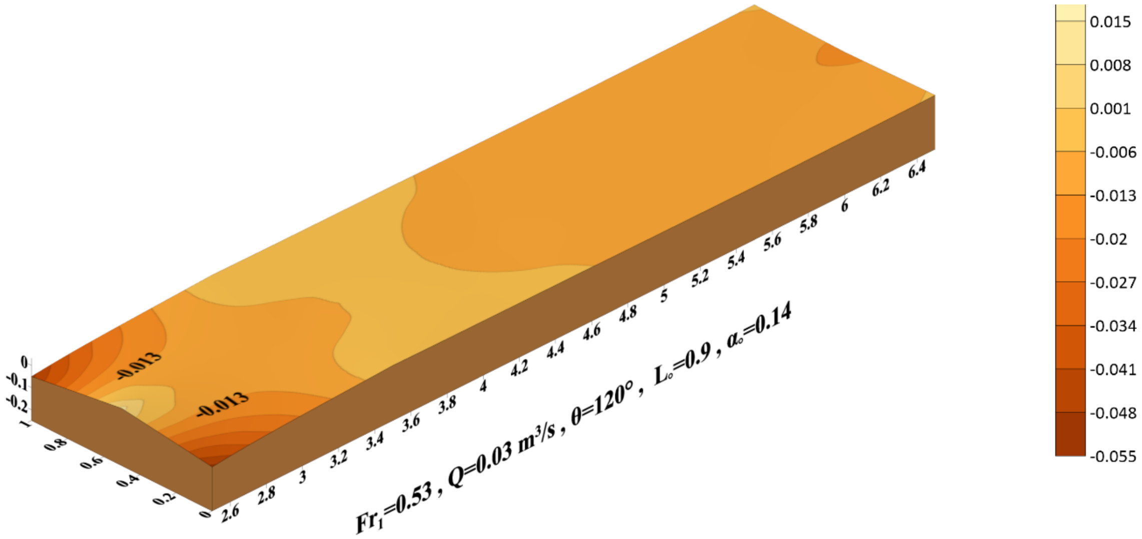

Figure (B.10): 3D scour profile for single perforated semicircular flow deflector with design parameter ($\theta=120^o$, $L_o=90\%$, $\alpha_o=14\%$) during a laboratory experiment, all dimensions in (m).

Figure (B.11): Picture for single perforated semicircular flow deflector with design parameter ($\theta=120^o$, $L_o=90\%$, $\alpha_o=14\%$) during a laboratory experiment for $Q=0.044 m^3/s$.

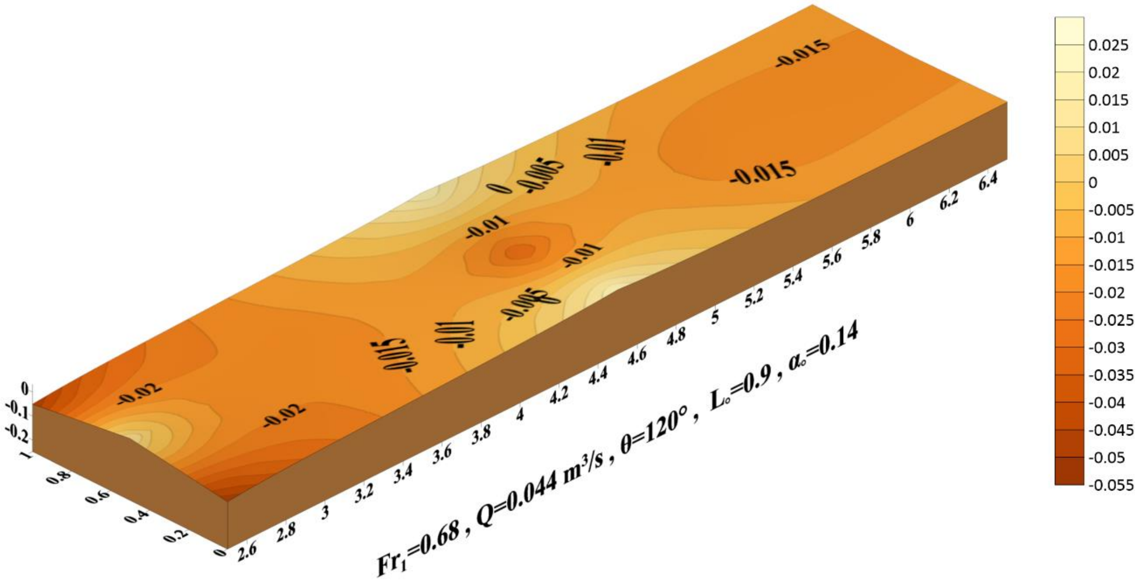

Figure (B.12): 3D scour profile for single perforated semicircular flow deflector with design parameter ($\theta=120^o$, $L_o=90\%$, $\alpha_o=14\%$) during a laboratory experiment, all dimensions in (m).

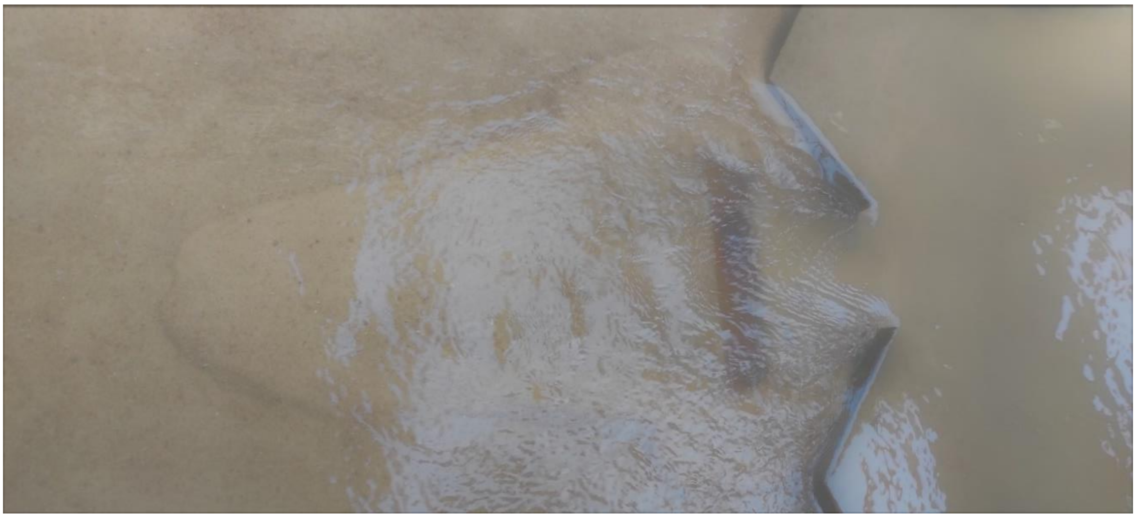

Figure (B.13): Picture for double solid triangular flow deflector with design parameter (θ=120^o, L_o=90%, α_o=14%) during a laboratory experiment for Q=0.0154m^3/s.

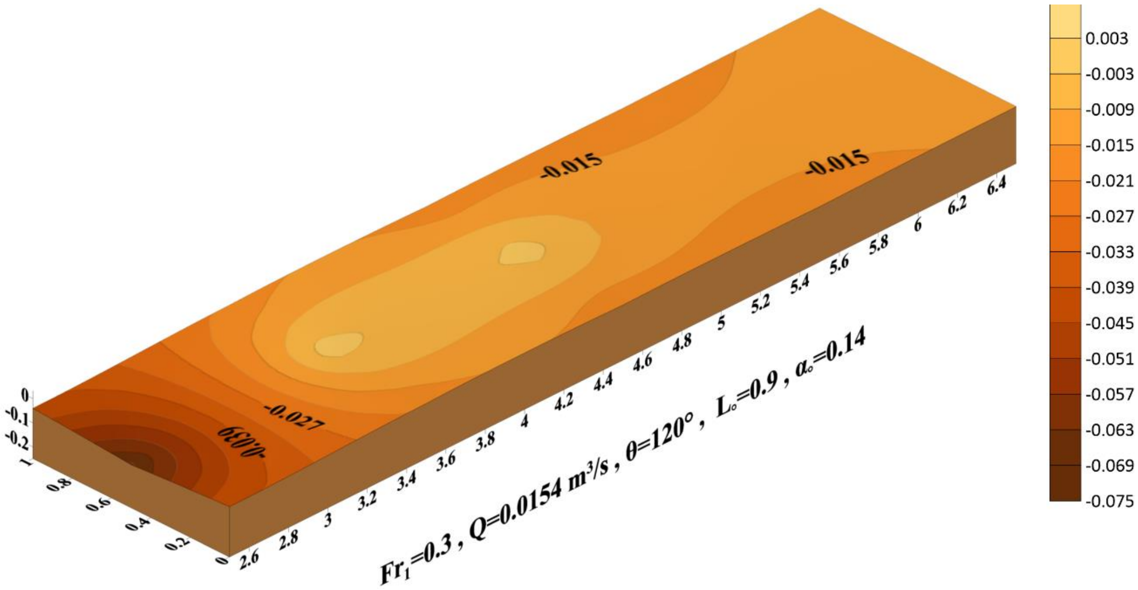

Figure (B.14): 3D scour profile for double solid triangular flow deflector with design parameter (θ=120^o, L_o=90%, α_o=14%) during a laboratory experiment, all dimensions in (m).

Figure (B.15): Picture for double solid triangular flow deflector with design parameter ($\theta=120^o$, $L_o=90\%$, $\alpha_o=14\%$) during a laboratory experiment for $Q=0.03m^3/s$.

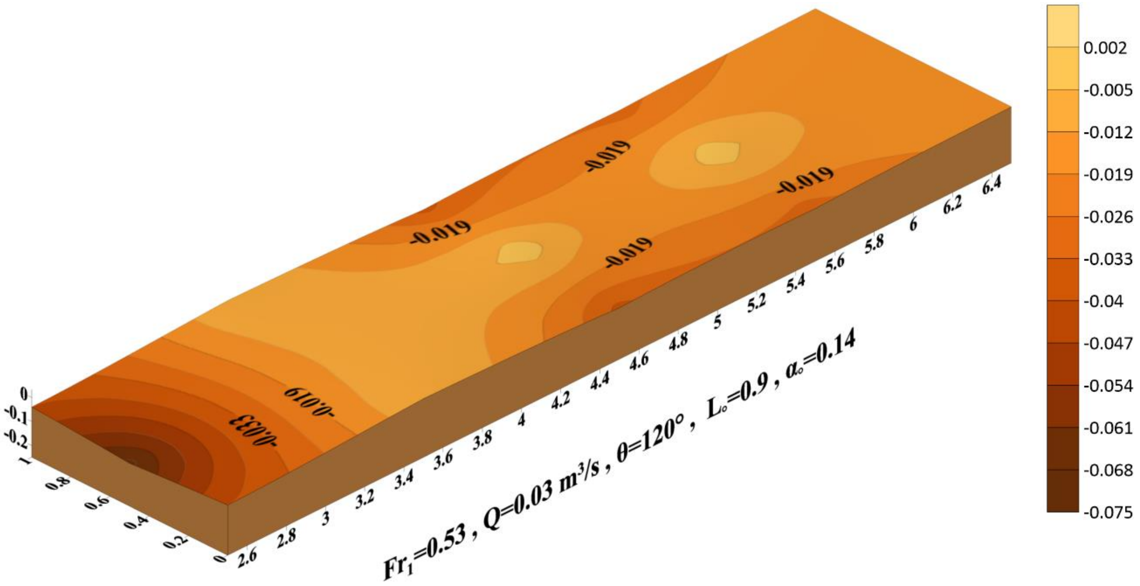

Figure (B.16): 3D scour profile for double solid triangular flow deflector with design parameter ($\theta=120^o$, $L_o=90\%$, $\alpha_o=14\%$) during a laboratory experiment, all dimensions in (m).

Figure (B.17): Picture for double solid triangular flow deflector with design parameter (θ=120^o, L_o=90%, α_o=14%) during a laboratory experiment for Q=0.044m^3/s.

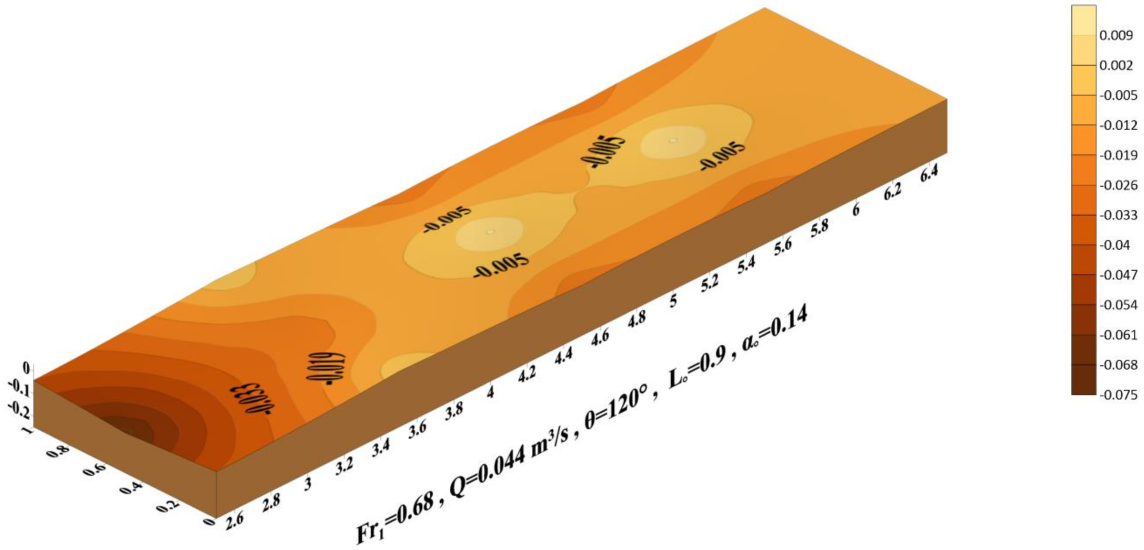

Figure (B.18): 3D scour profile for double solid triangular flow deflector with design parameter (θ=120^o, L_o=90%, α_o=14%) during a laboratory experiment, all dimensions in (m).

Figure (B.19): Picture for double solid semicircular flow deflector with design parameter (θ=120^o, L_o=90%, α_o=14%) during a laboratory experiment for Q=0.0154m^3/s.

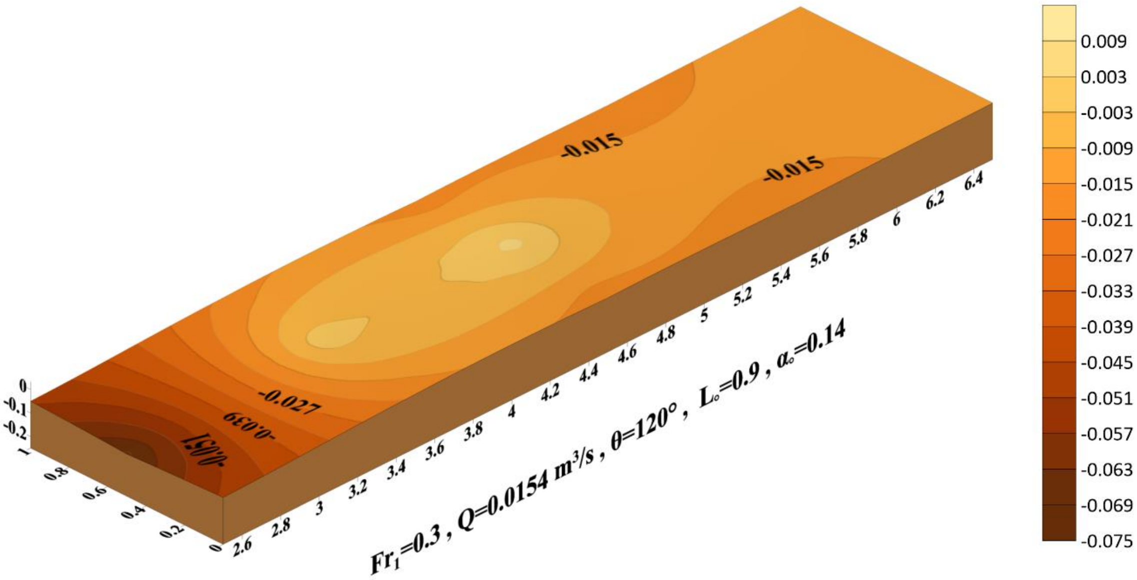

Figure (B.20): 3D scour profile for double solid semicircular flow deflector with design parameter (θ=120^o, L_o=90%, α_o=14%) during a laboratory experiment, all dimensions in (m).

Figure (B.21): Picture for double solid semicircular flow deflector with design parameter (θ=120°, L_o=90%, α_o=14%) during a laboratory experiment for Q=0.03m^3/s.

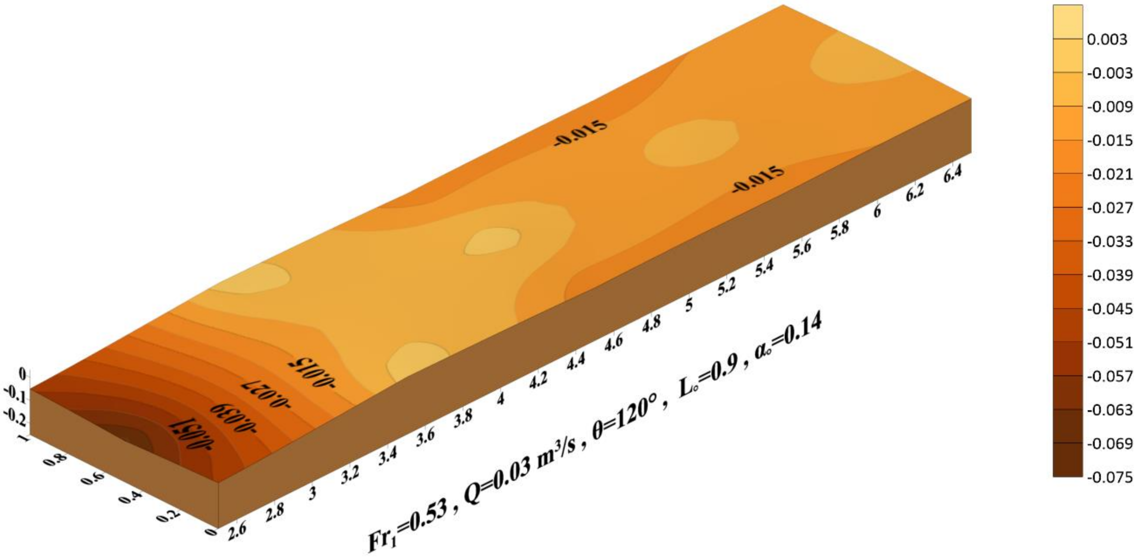

Figure (B.22): 3D scour profile for double solid semicircular flow deflector with design parameter (θ=120°, L_o=90%, α_o=14%) during a laboratory experiment, all dimensions in (m).

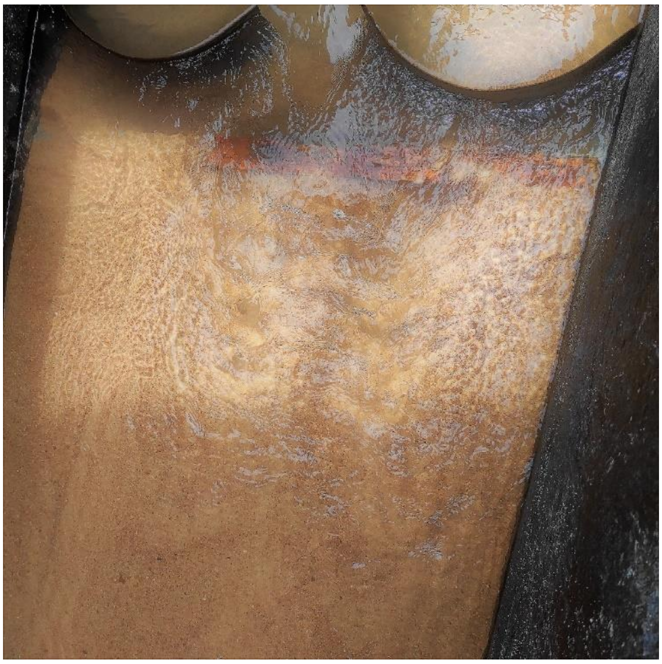

Figure (B.23): Picture for double solid semicircular flow deflector with design parameter ($\theta=120^o$, $L_o=90\%$, $\alpha_o=14\%$) during a laboratory experiment for $Q=0.044m^3/s$.

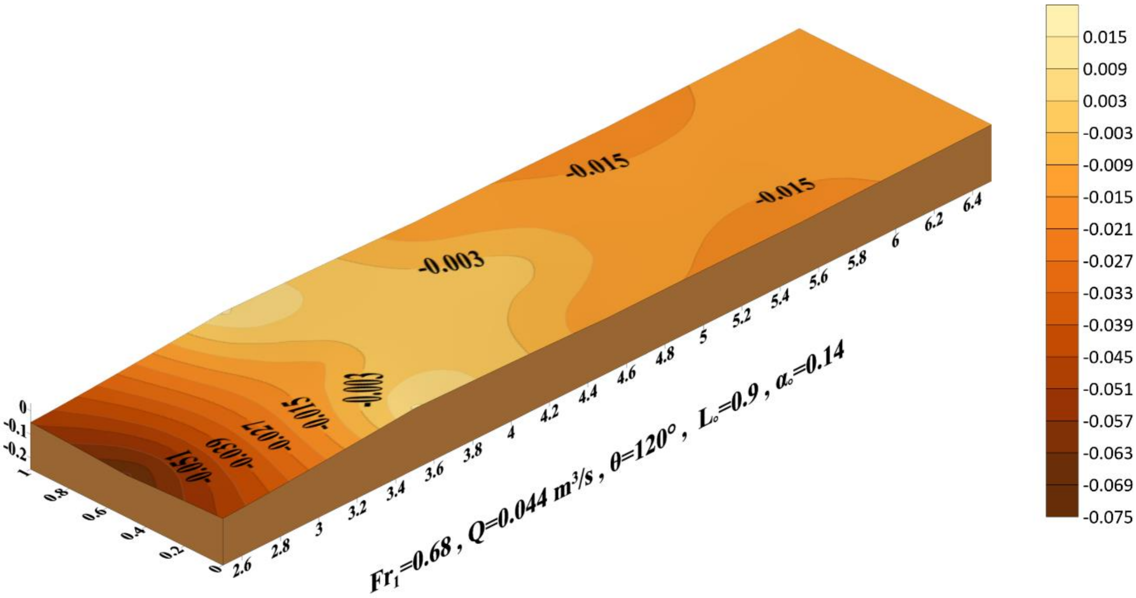

Figure (B.24): 3D scour profile for double solid semicircular flow deflector with design parameter ($\theta=120^o$, $L_o=90\%$, $\alpha_o=14\%$) during a laboratory experiment, all dimensions in (m).

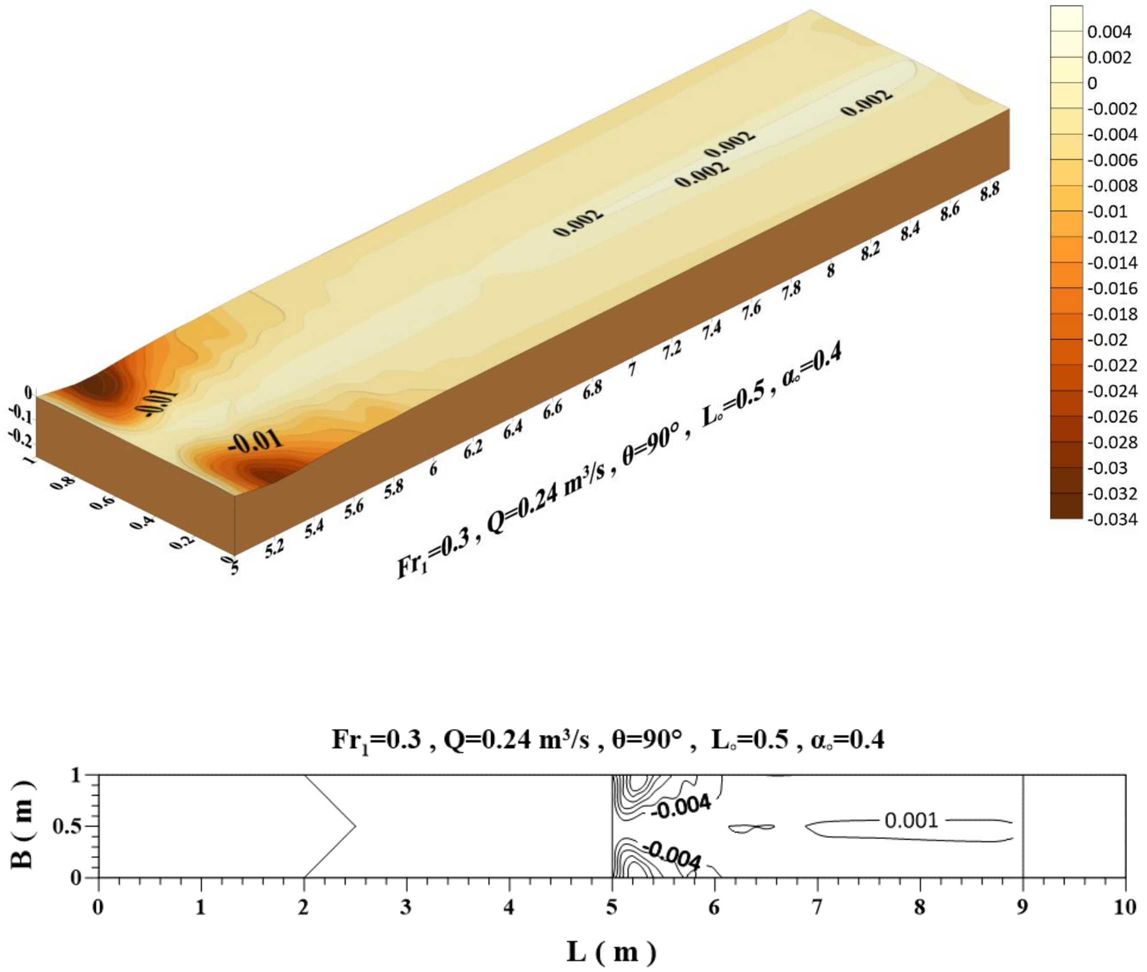

Figure (B.25): 3D scour profile and counter line for single perforated triangular flow deflector with design parameter ($\theta=90^o$, $L_o=50\%$, $\alpha_o=40\%$), all dimensions in (m).

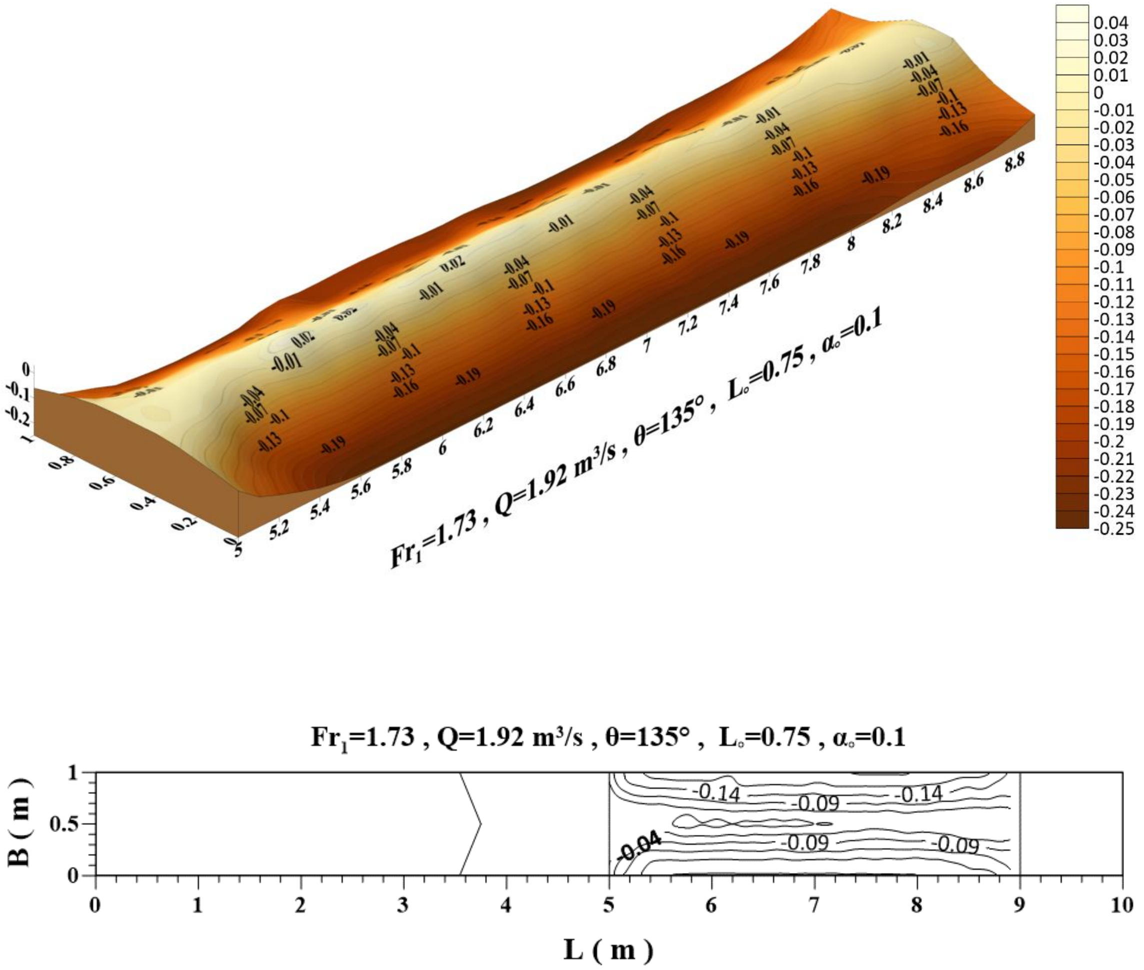

Figure (B.26): 3D scour profile and counter line for single perforated triangular flow deflector with design parameter ($\theta=135^o$, $L_o=75\%$, $\alpha_o=10\%$), all dimensions in (m).

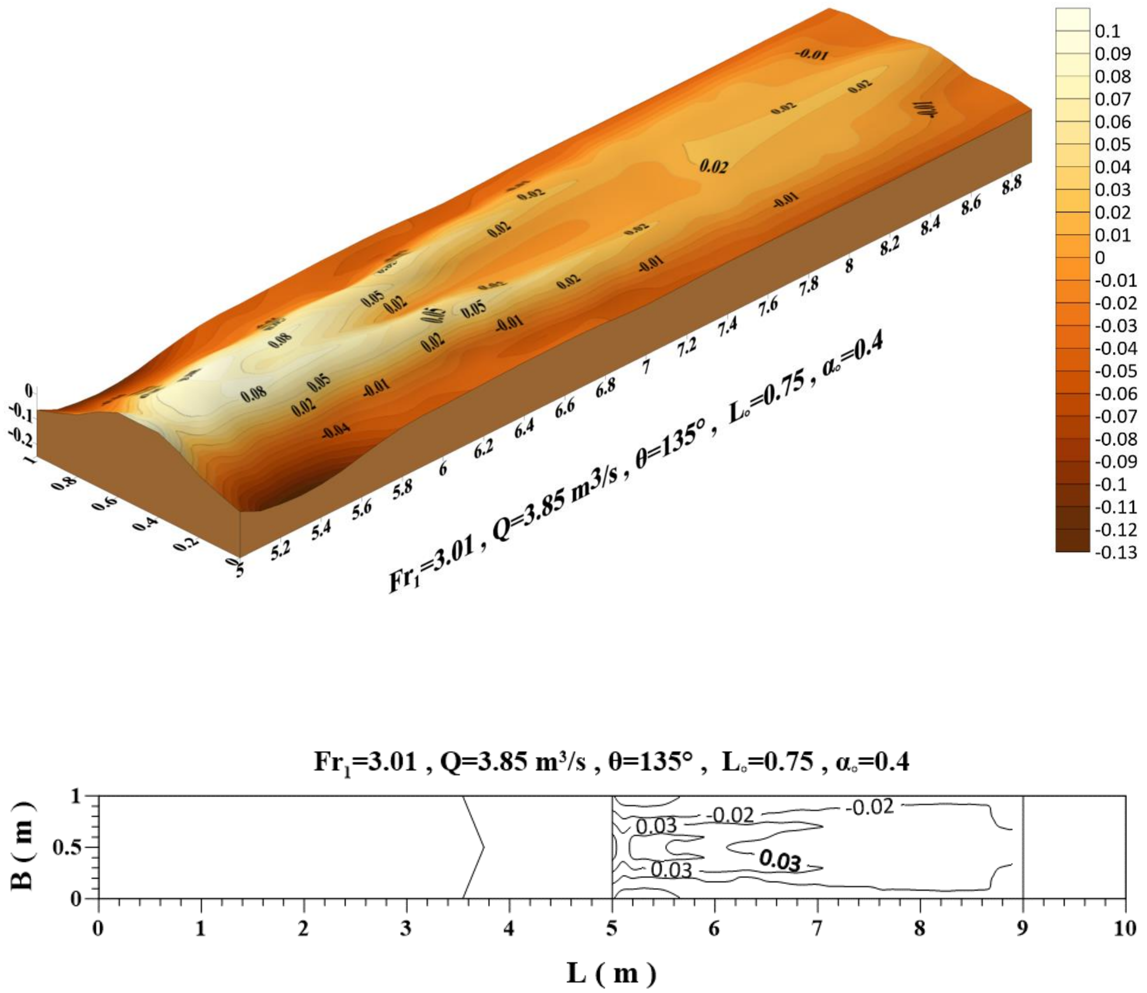

Figure (B.27): 3D scour profile and counter line for single perforated triangular flow deflector with design parameter (θ=135°, L$_o$=75%, α$_o$=40%), all dimensions in (m).

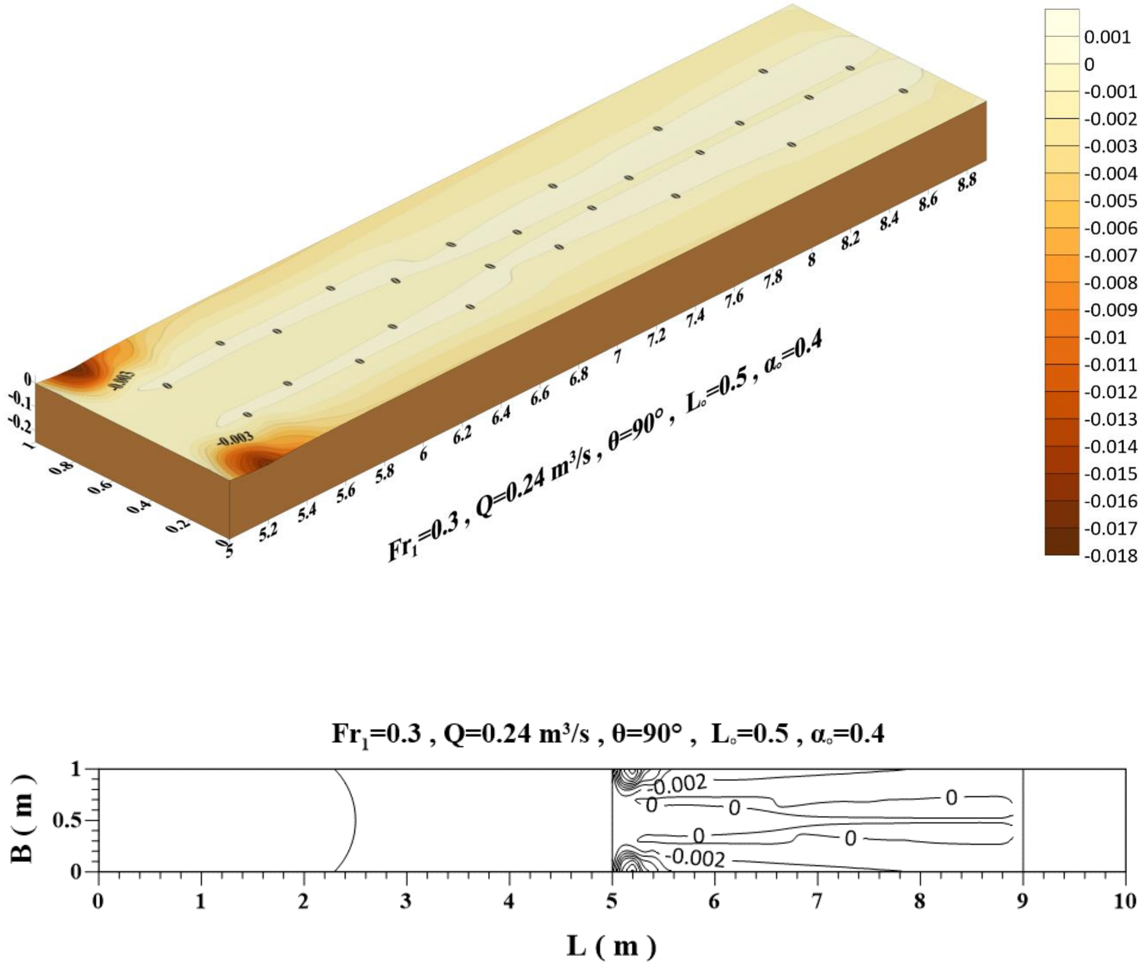

Figure (B.28): 3D scour profile and counter line for single perforated semicircular flow deflector with design parameter (θ=90°, L$_o$=50%, α$_o$=40%), all dimensions in (m).

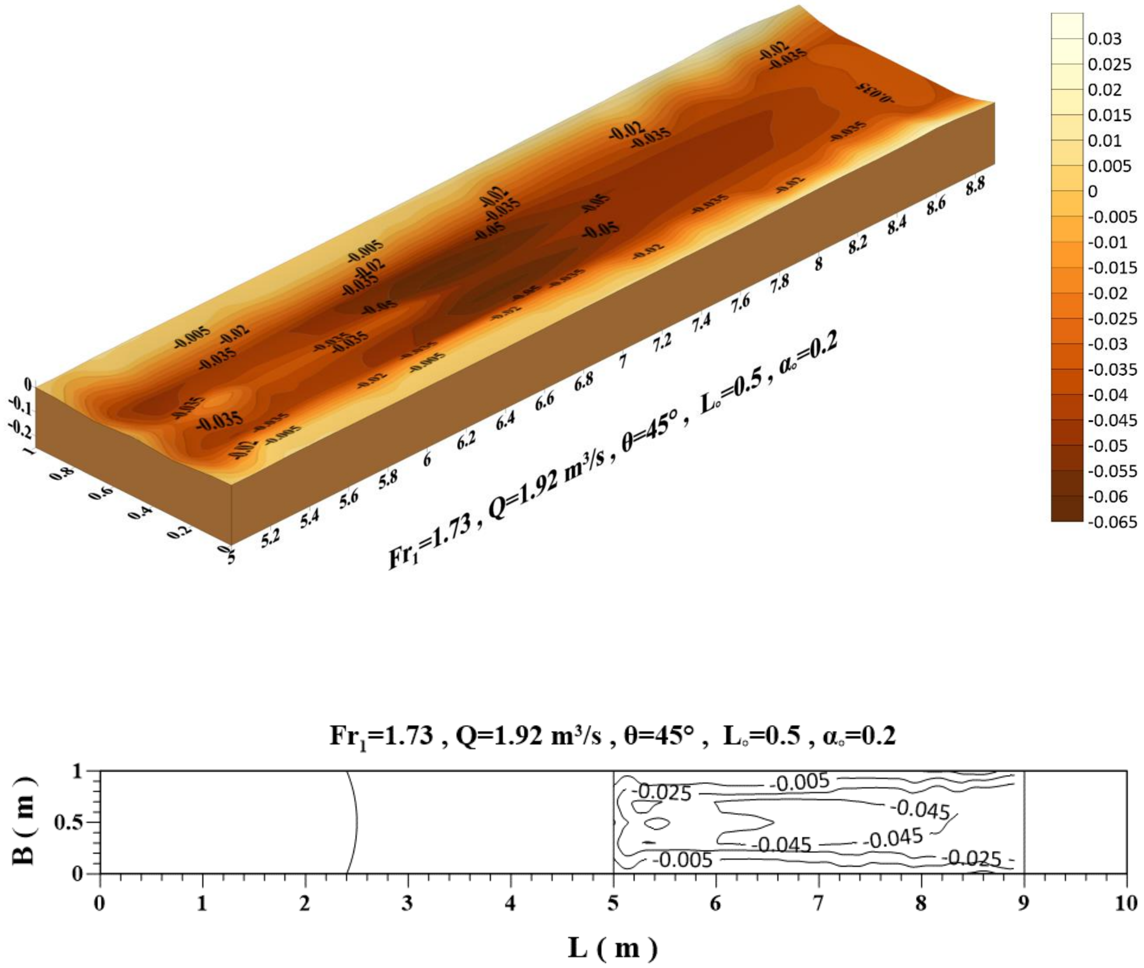

Figure (B.29): 3D scour profile and counter line for single perforated semicircular flow deflector with design parameter (θ=45º, L_o=50%, α_o=20%), all dimensions in (m).

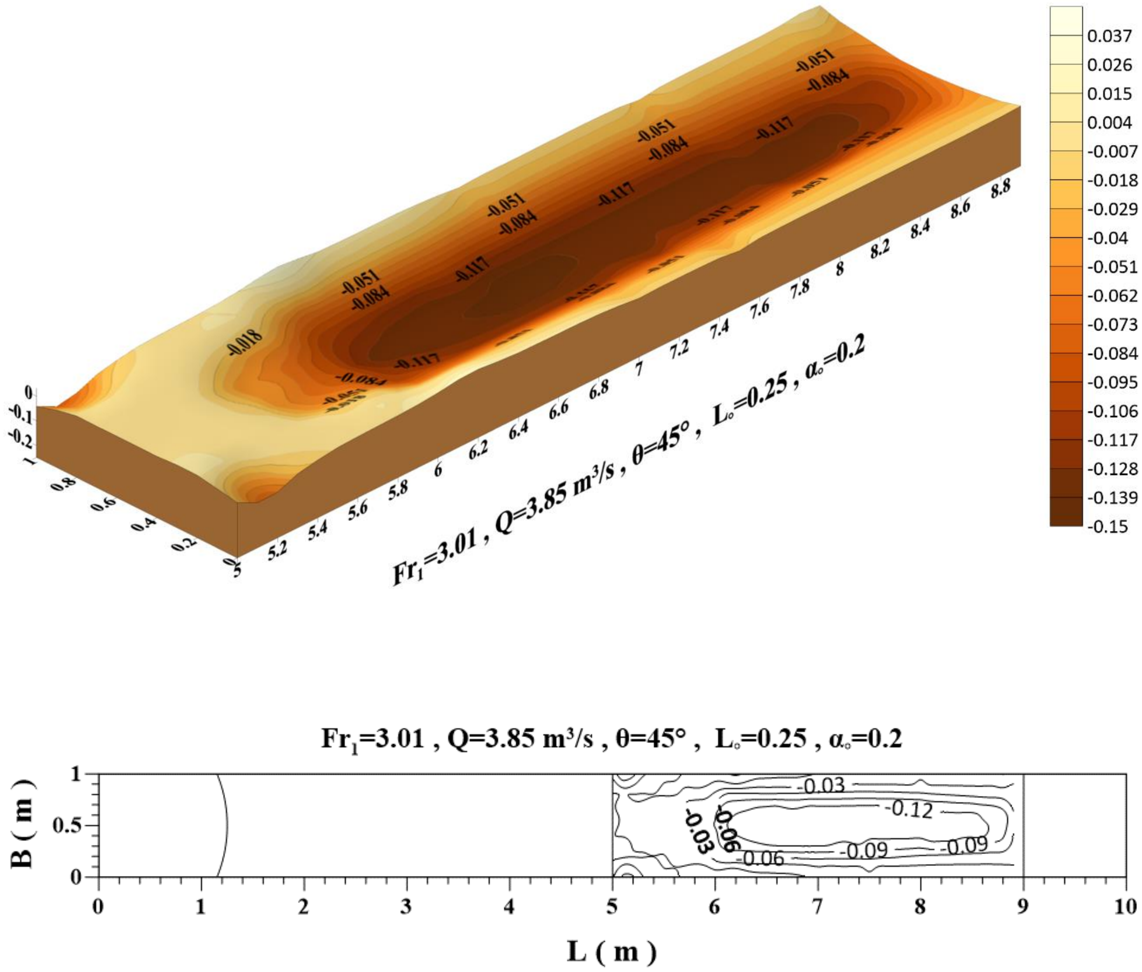

Figure (B.30): 3D scour profile and counter line for single perforated semicircular flow deflector with design parameter (θ=45^{o}, L_o=25%, α_o=20%), all dimensions in (m).

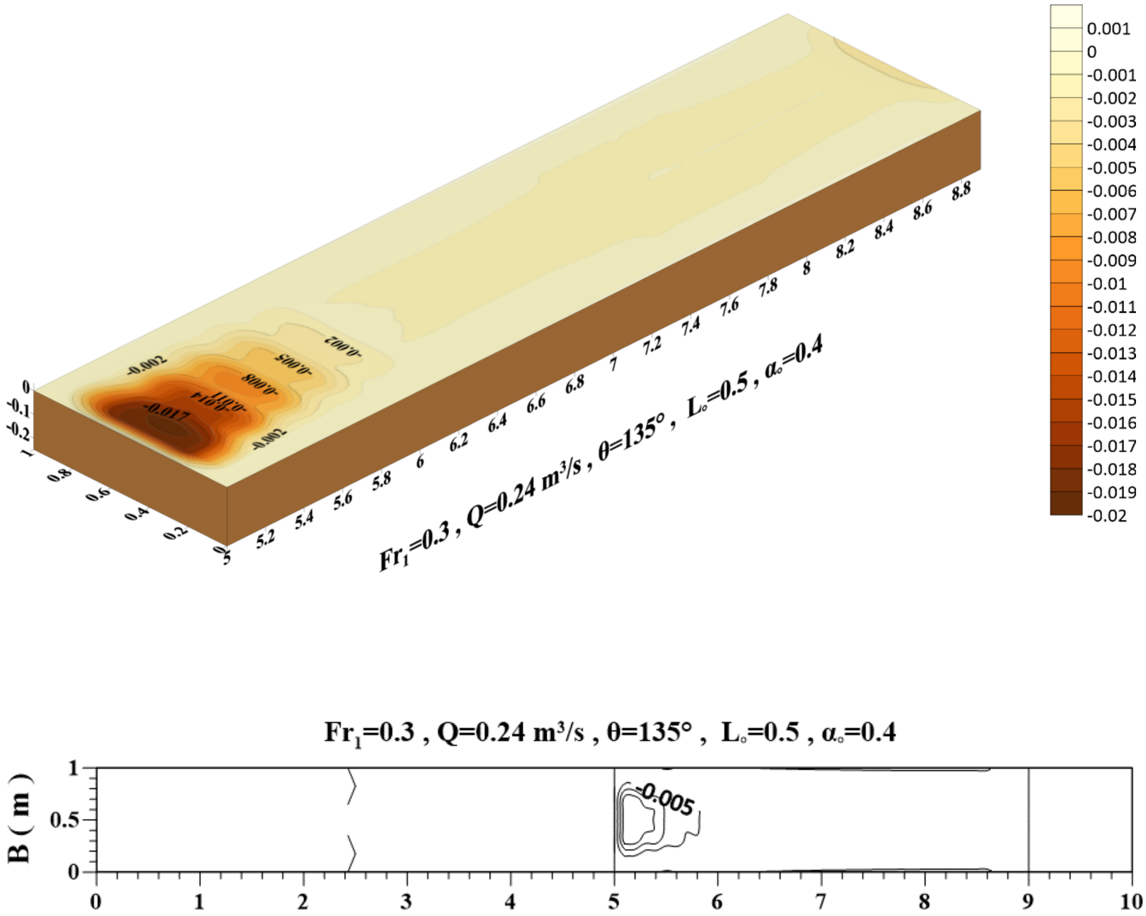

Figure (B.31): 3D scour profile and counter line for double solid triangular flow deflector with design parameter (θ=135°, L_o=50%, α_o=40%), all dimensions in (m).

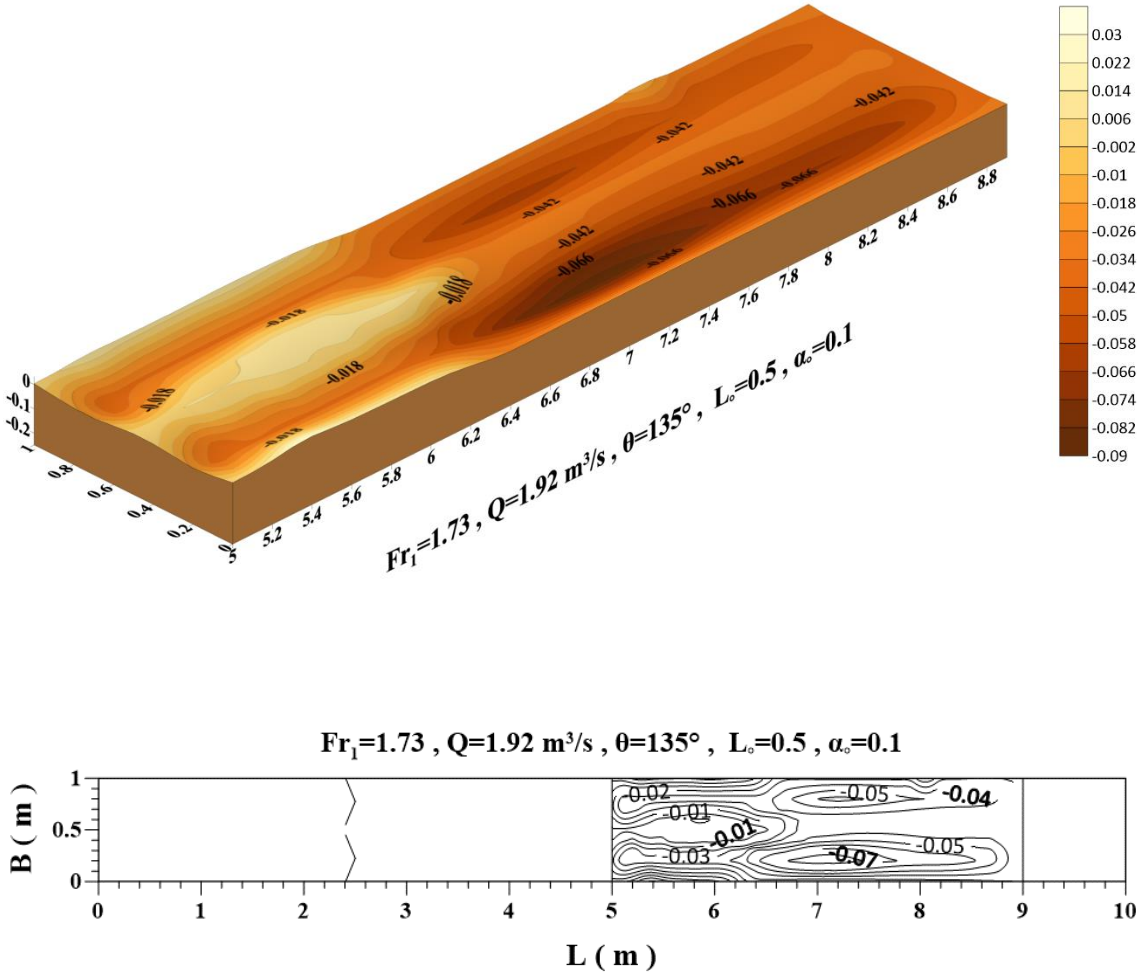

Figure (B.32): 3D scour profile and counter line for double solid triangular flow deflector with design parameter (θ=135°, L_o=50%, α_o=10%), all dimensions in (m).

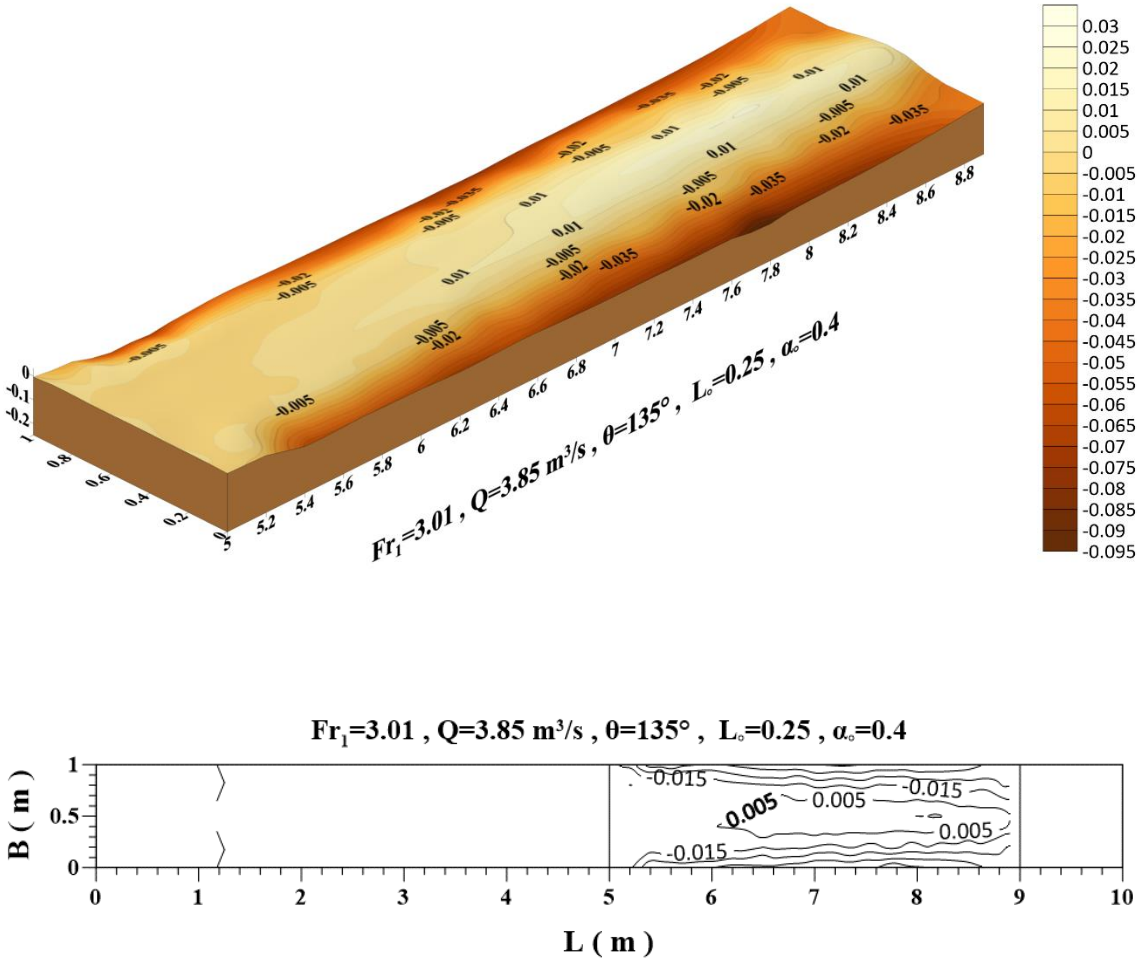

Figure (B.33): 3D scour profile and counter line for double solid triangular flow deflector with design parameter ($\theta=135^o$, $L_o=25\%$, $\alpha_o=40\%$), all dimensions in (m).

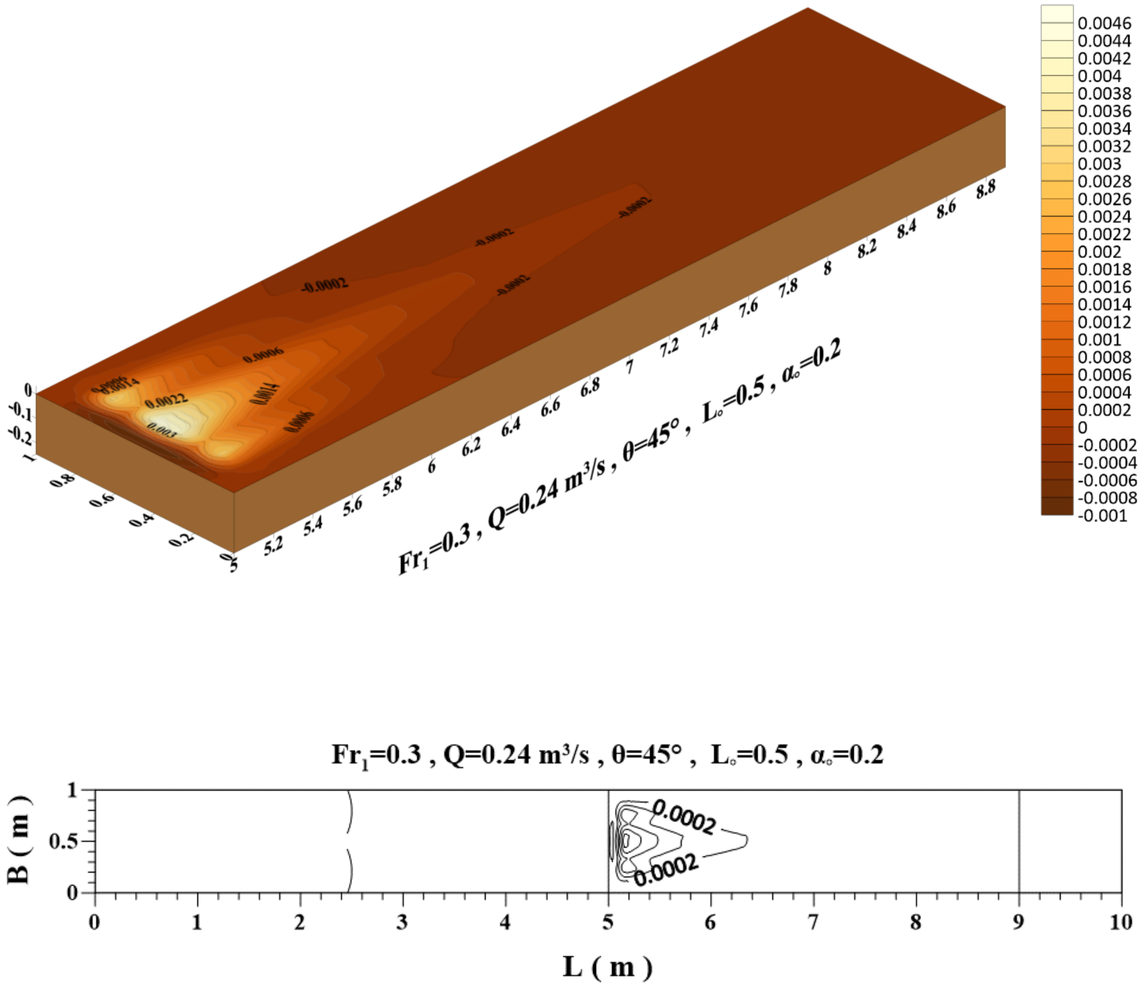

Figure (B.34): 3D scour profile and counter line for double solid semicircular flow deflector with design parameter (θ=45°, L_o=50%, α_o=20%), all dimensions in (m).

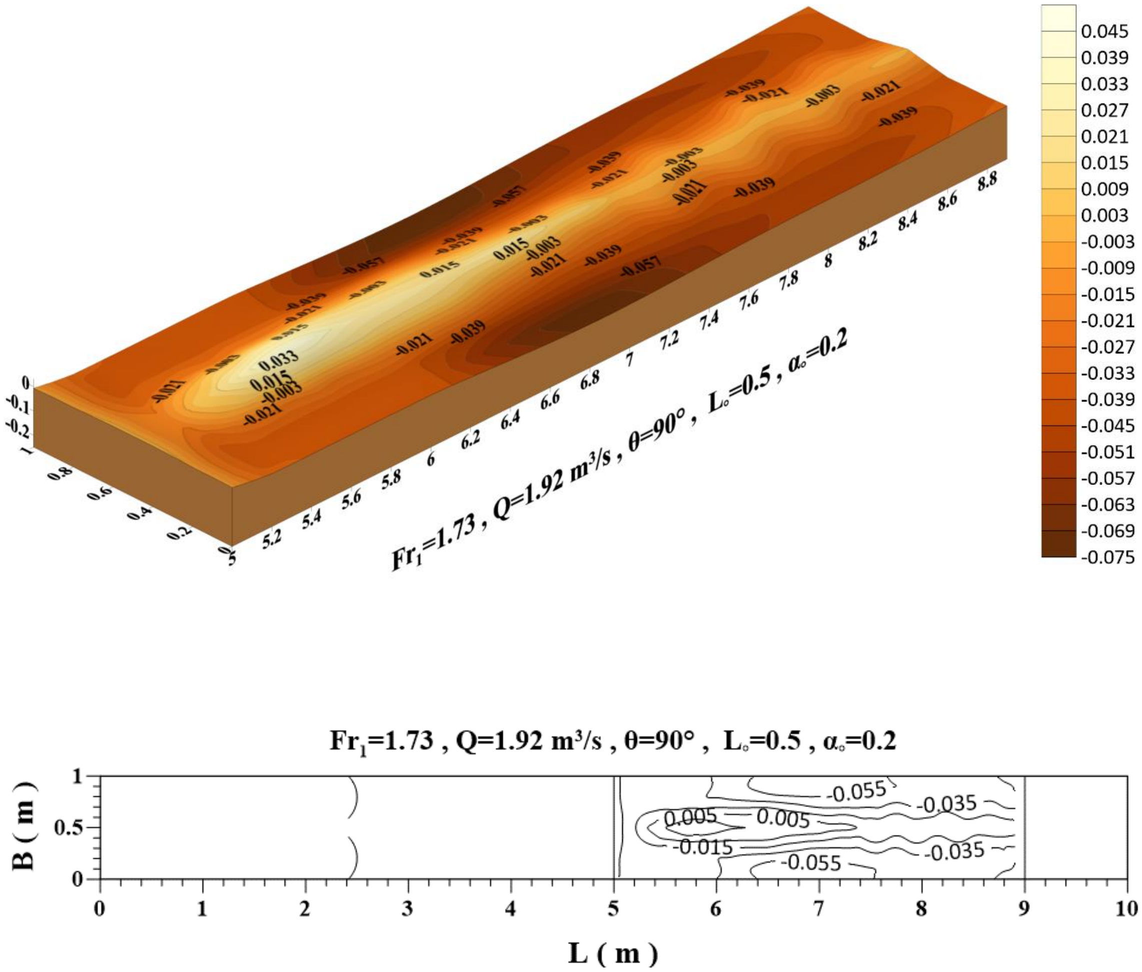

Figure (B.35): 3D scour profile and counter line for double solid semicircular flow deflector with design parameter (θ=90º, L$_o$=50%, α$_o$=20%), all dimensions in (m).

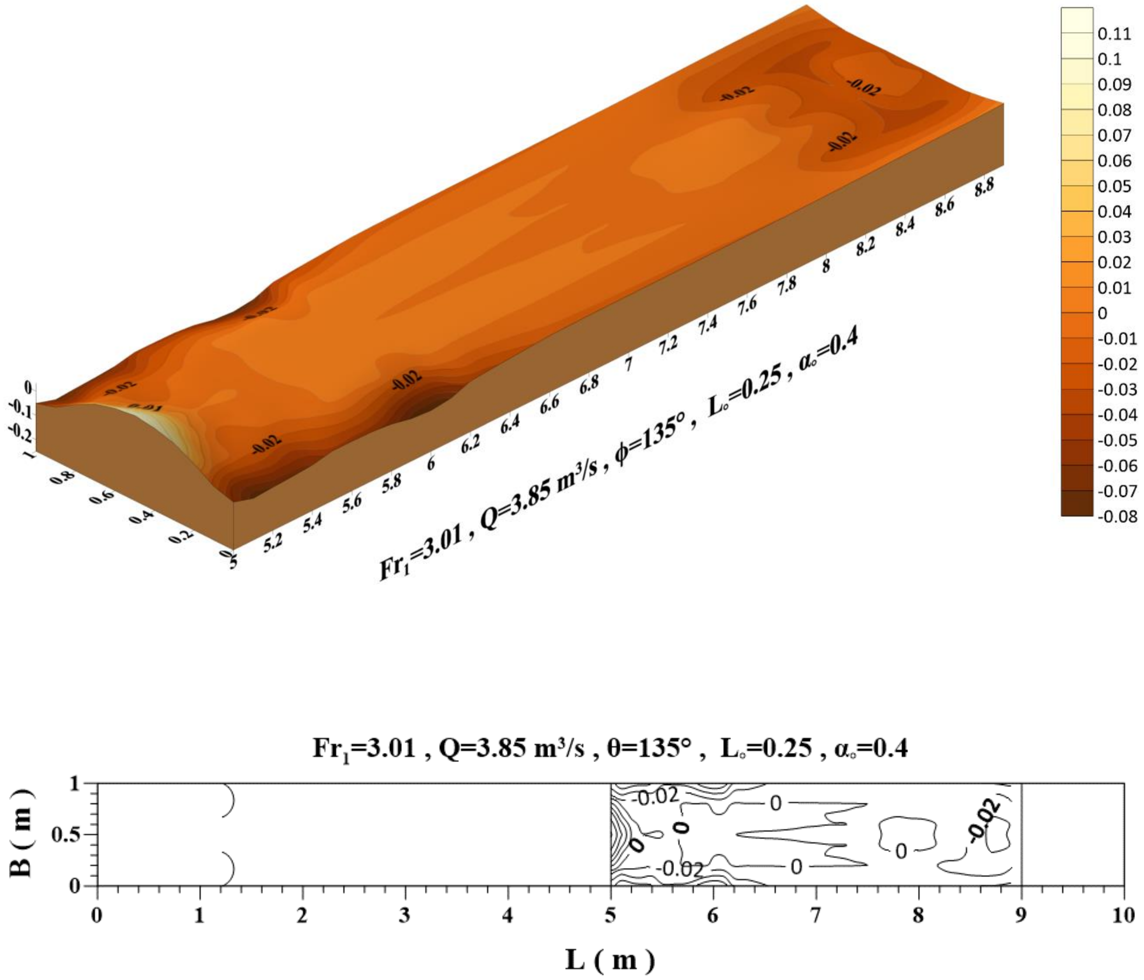

Figure (B.36): 3D scour profile and counter line for double solid semicircular flow deflector with design parameter (θ=135°, L_o=25%, α_o=40%), all dimensions in (m).

Appendix [C]

The design charts for flow deflectors

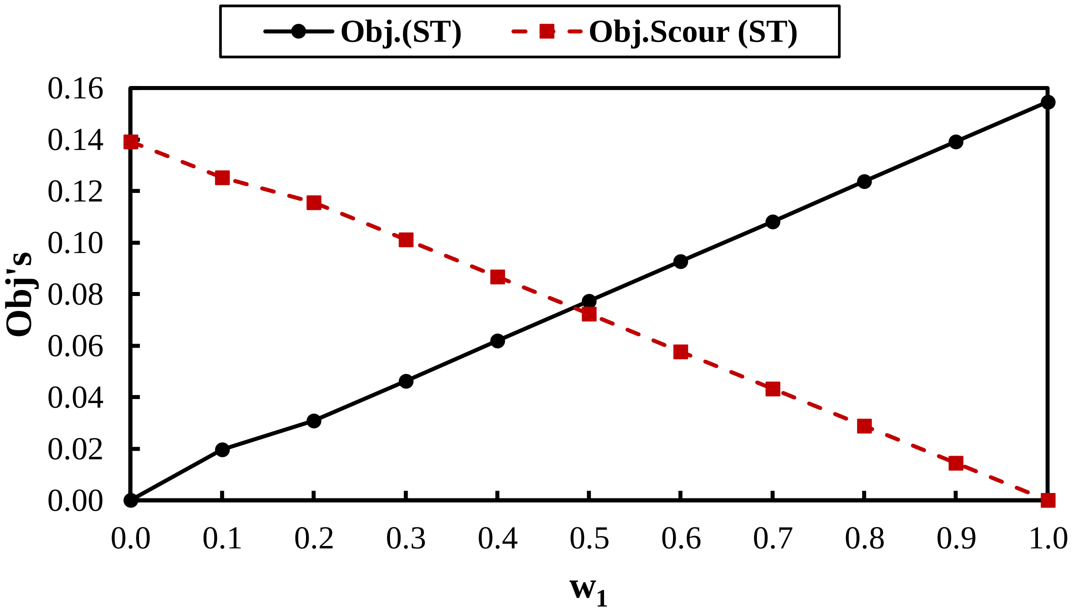

Figure (C. 1): Objective functions versus different value of first objective weights for single perforated triangular deflector.

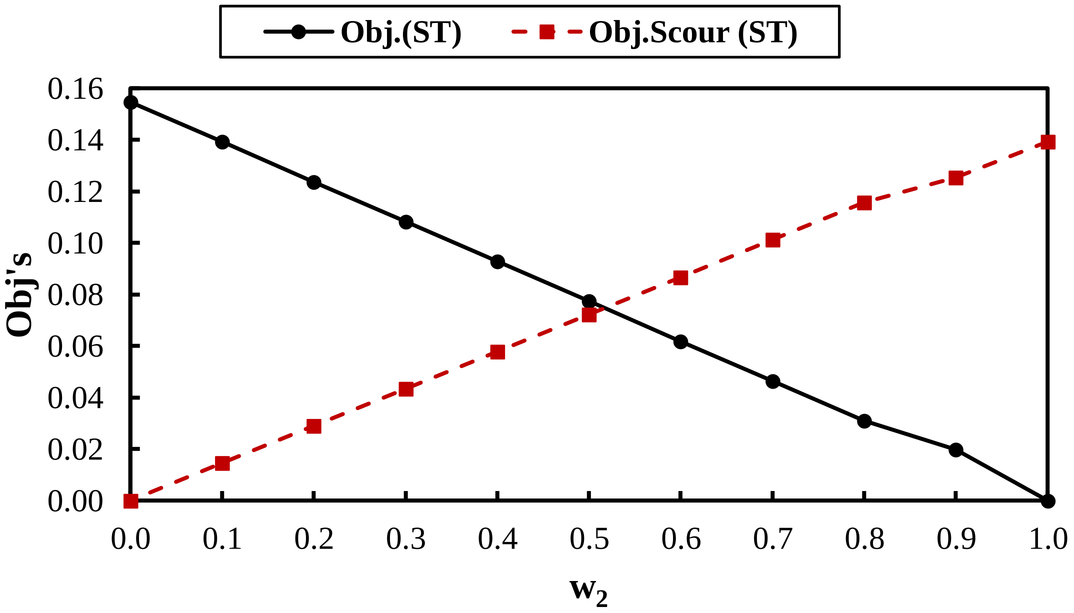

Figure (C.2): Objective functions versus different value of second objective weights for single perforated triangular deflector.

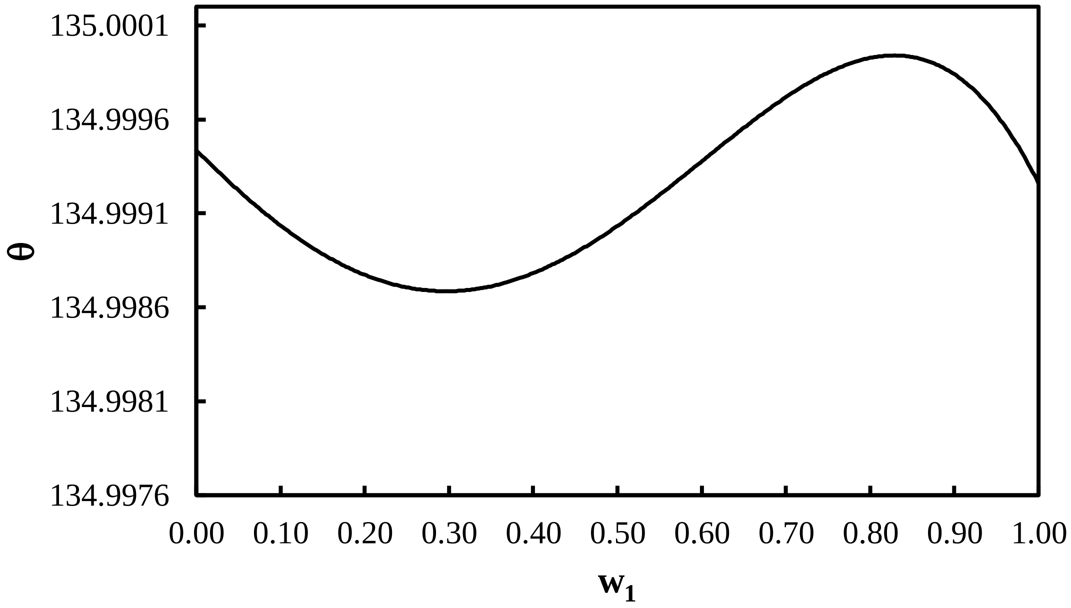

Figure (C.3): Deflector angle (in degree) versus different value of first objective weights for single perforated triangular deflector.

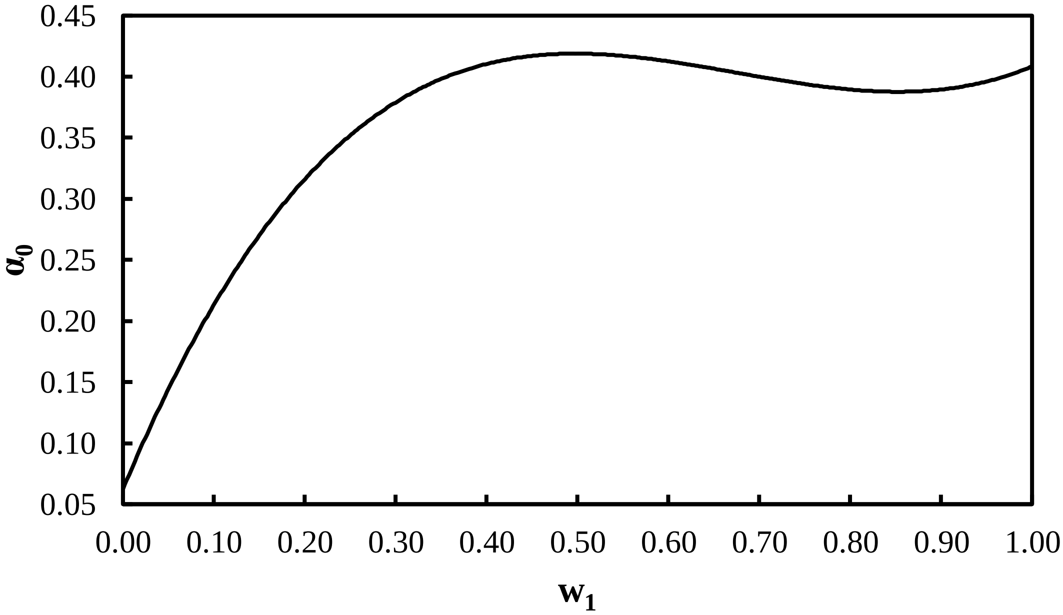

Figure (C.4): Passageway ratio versus different value of first objective weights for single perforated triangular deflector.

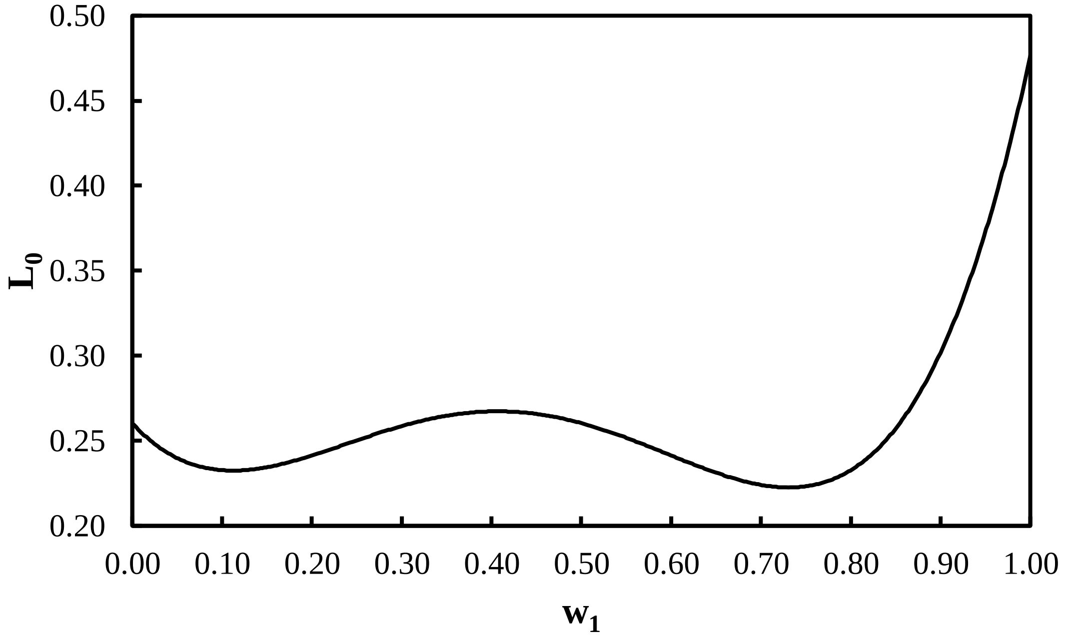

Figure (C.5): Position ratio deflector versus different value of objective weights for single perforated triangular deflector.

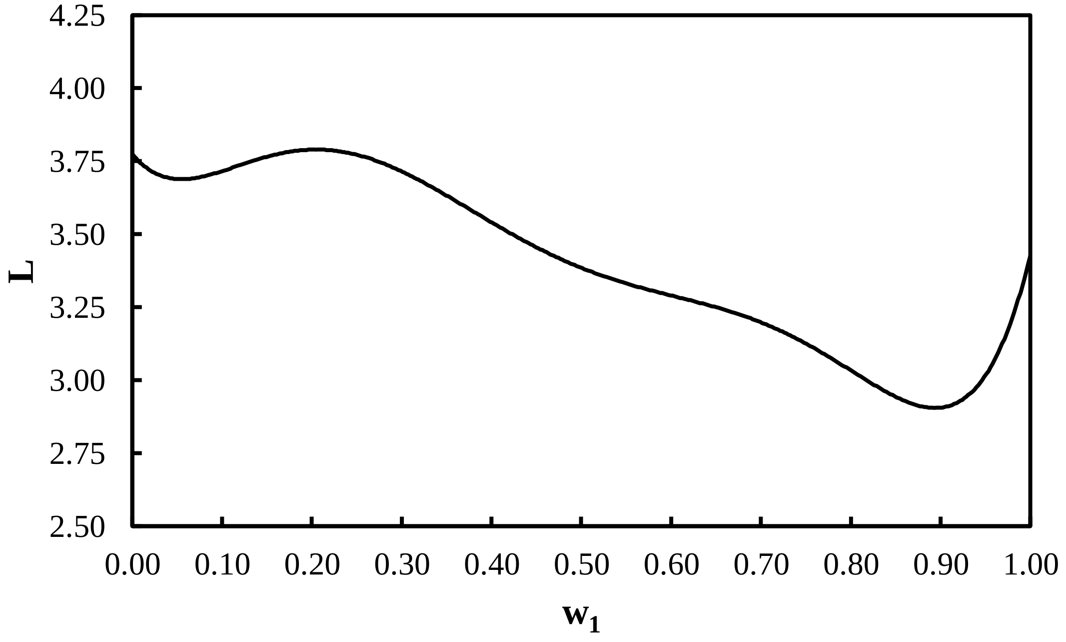

Figure (C.6): Length of stilling basin versus different value of objective weights for single perforated triangular deflector.

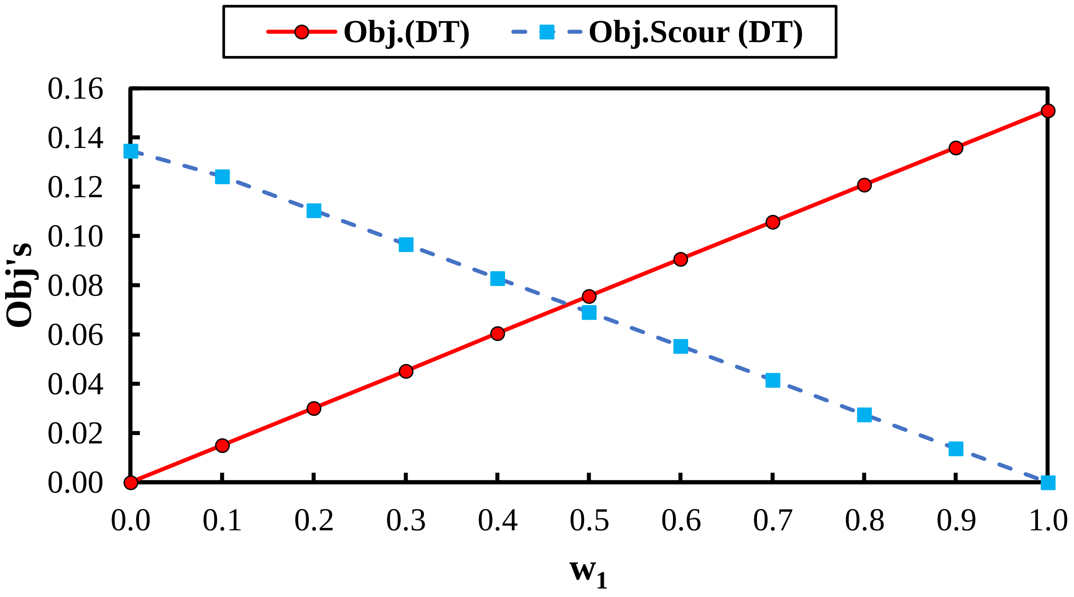

Figure (C.7): Objective functions versus different value of first objective weights for double solid triangular deflector.

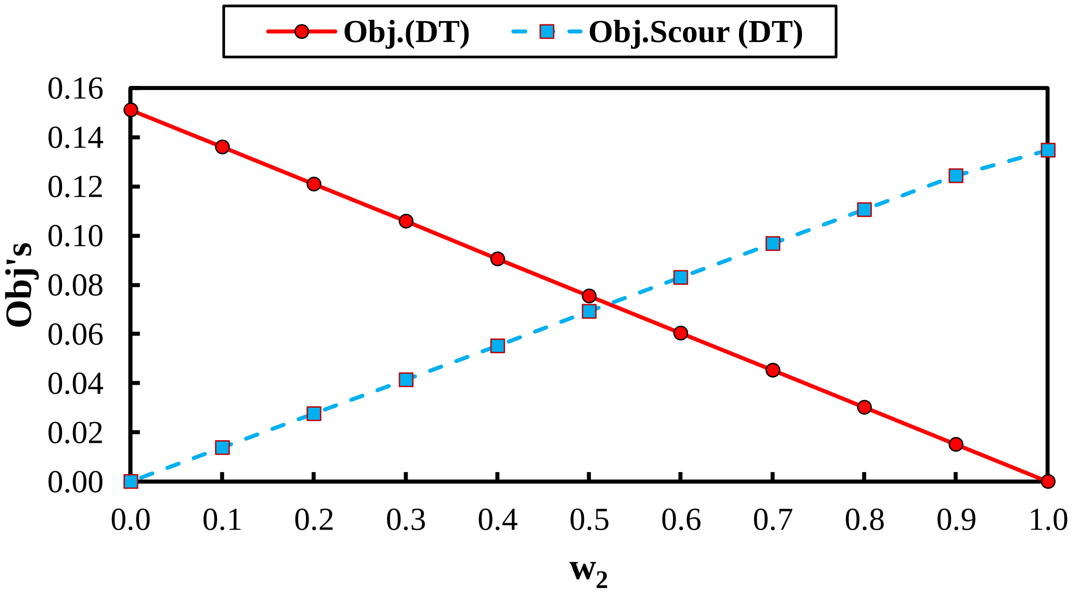

Figure (C.8): Objective functions versus different value of second objective weights for double solid triangular deflector.

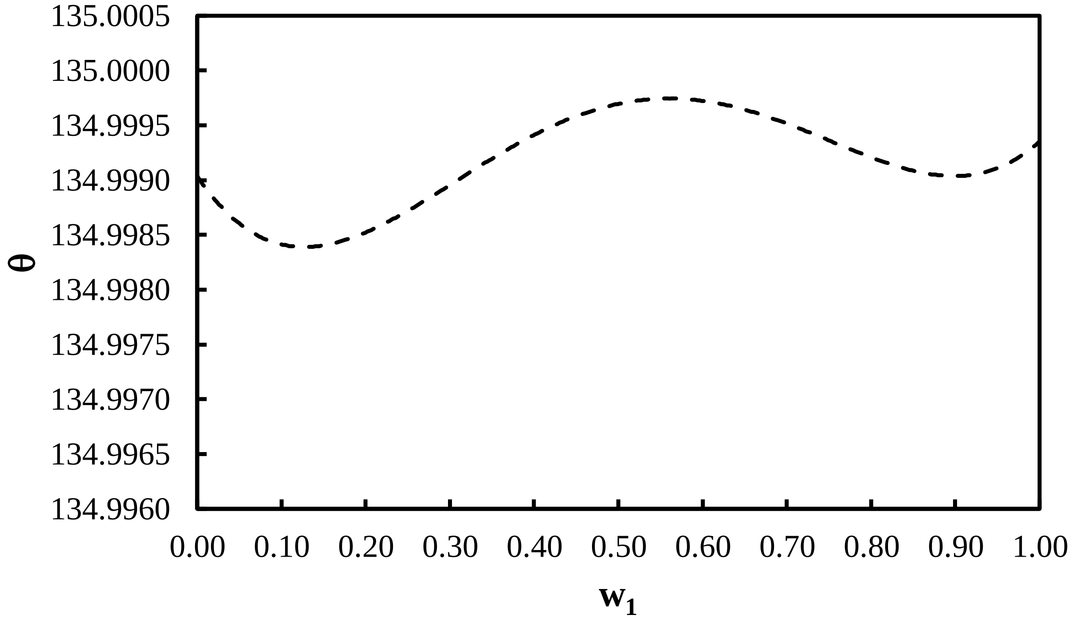

Figure (C.9): Deflector angle (in degree) versus different value of first objective weights for double solid triangular deflector.

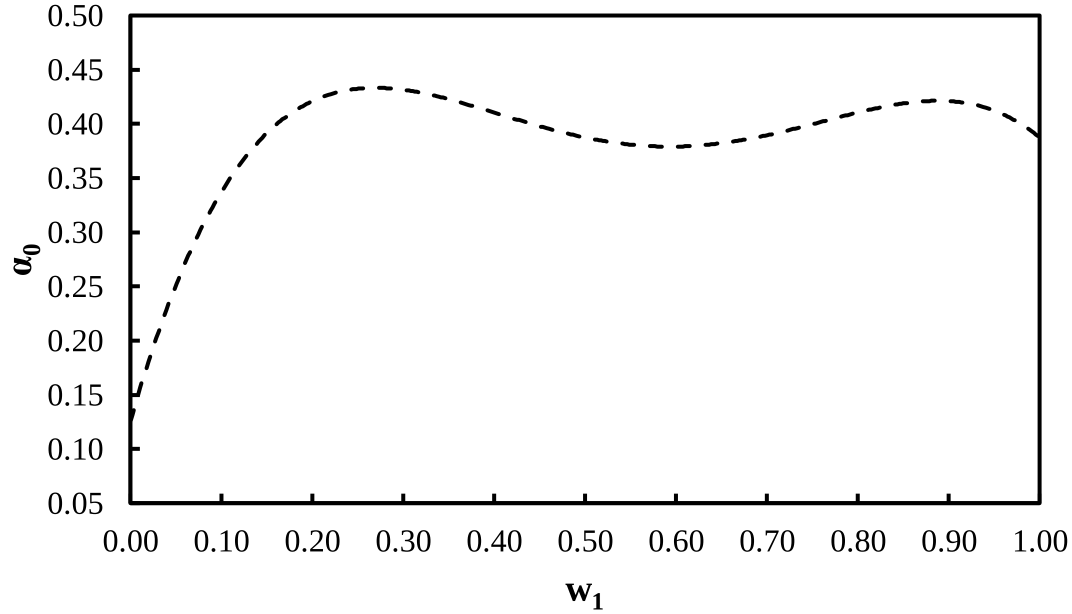

Figure (C.10): Passageway ratio versus different value of first objective weights for double solid triangular deflector.

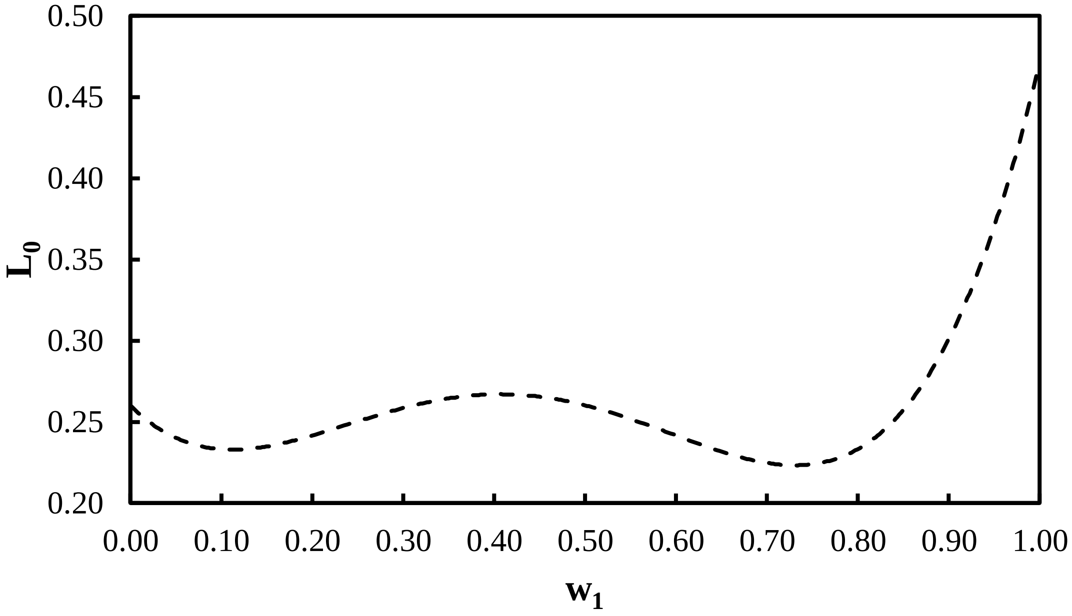

Figure (C.11): Position ratio deflector versus different value of objective weights for double solid triangular deflector.

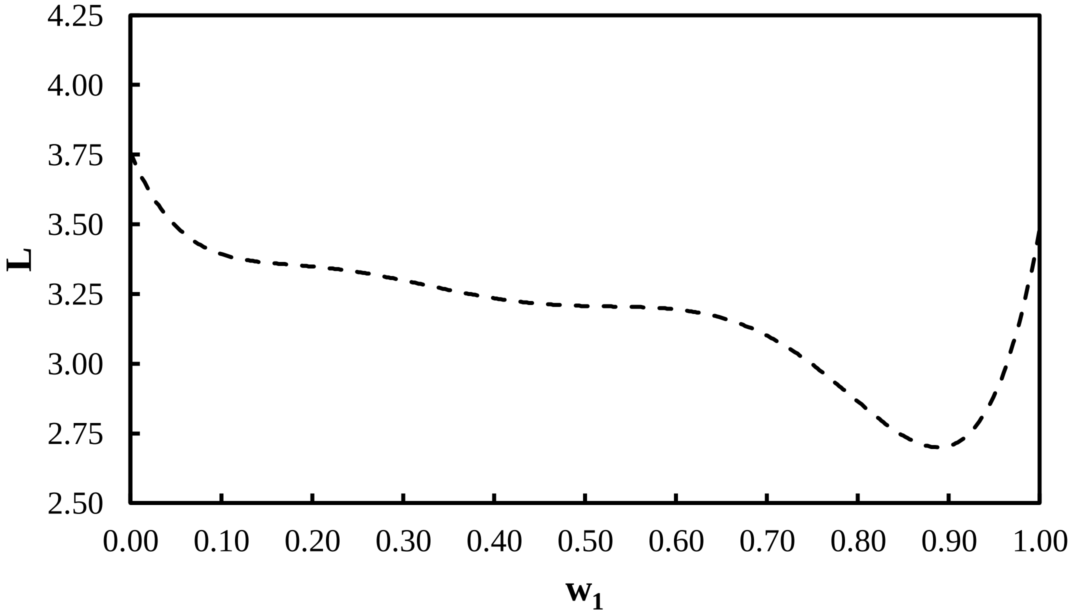

Figure (C.12): Length of stilling basin versus different value of objective weights for double solid triangular deflector.

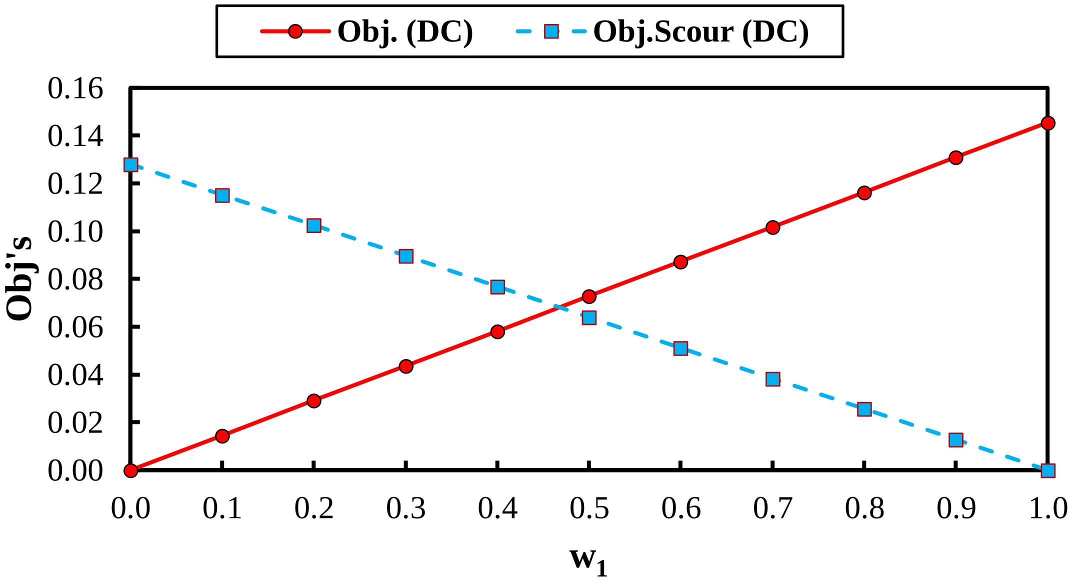

Figure (C.13): Objective functions versus different value of first objective weights for double solid semicircle deflector.

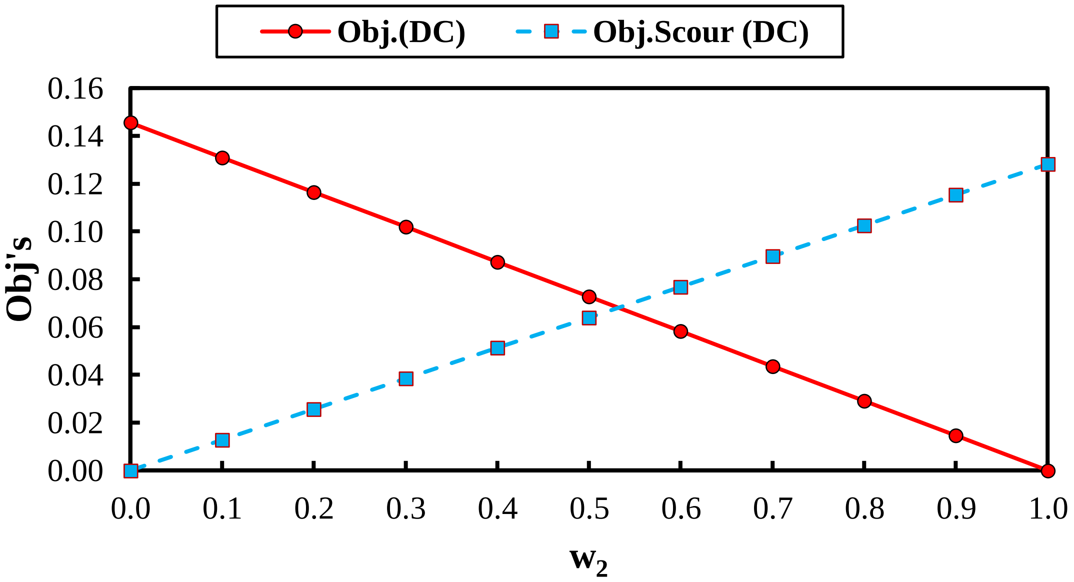

Figure (C.14): Objective functions versus different value of second objective weights for double solid semicircle deflector.

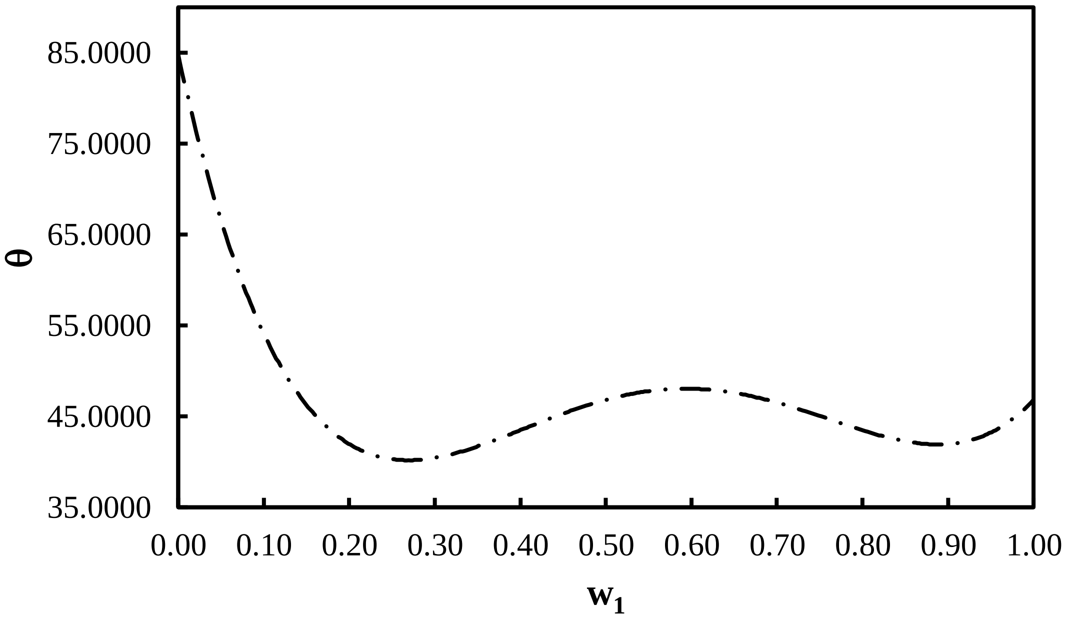

Figure (C.15): Deflector angle (in degree) versus different value of first objective weights for double solid semicircle deflector.

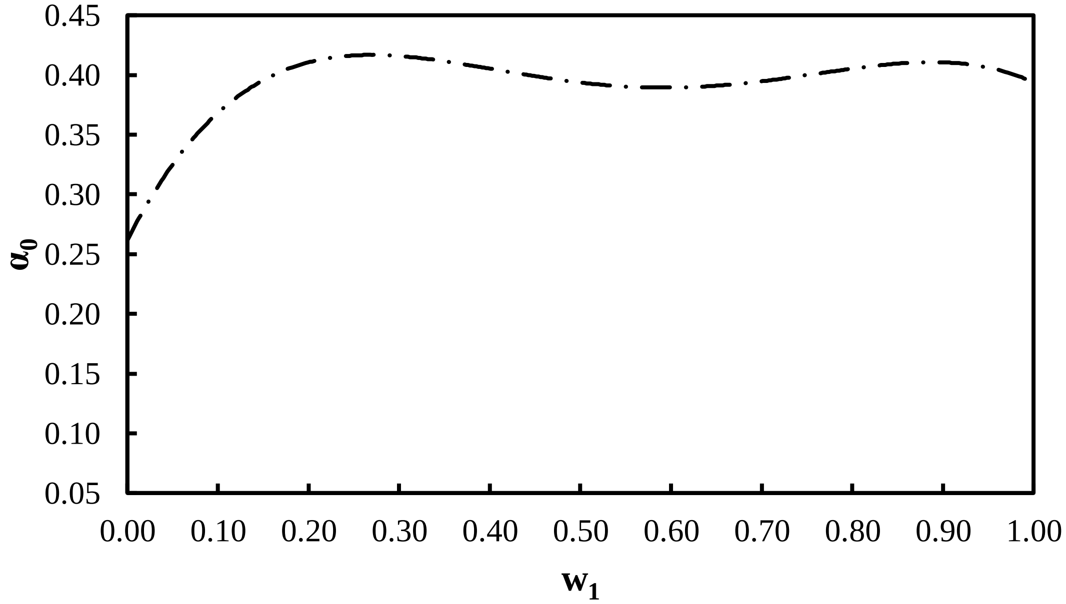

Figure (C.16): Passageway ratio versus different value of first objective weights for double solid semicircle deflector.

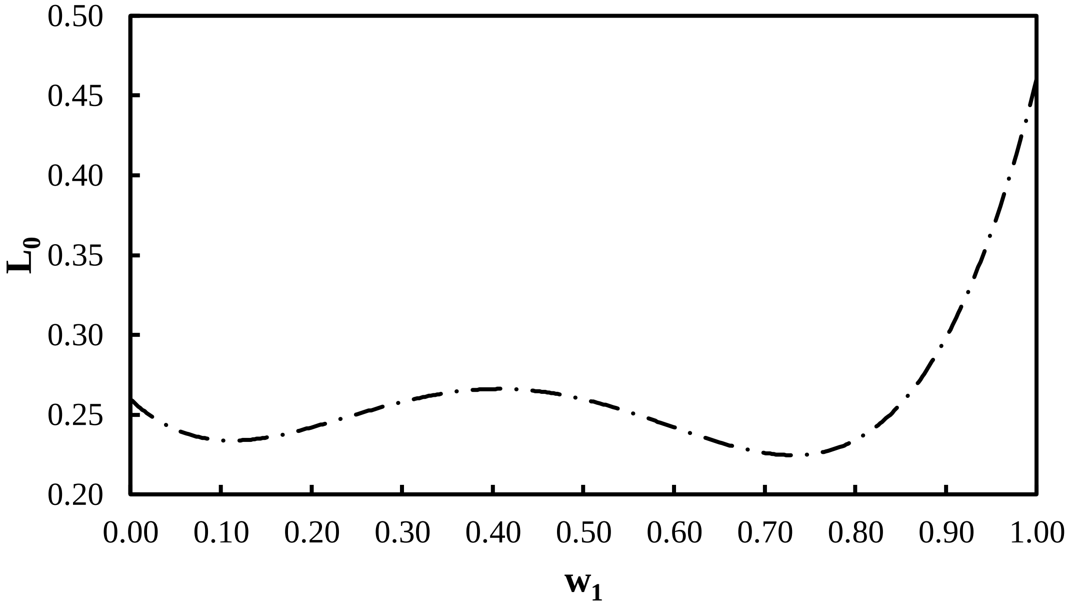

Figure (C.17): Position ratio deflector versus different value of objective weights for double solid semicircle deflector.

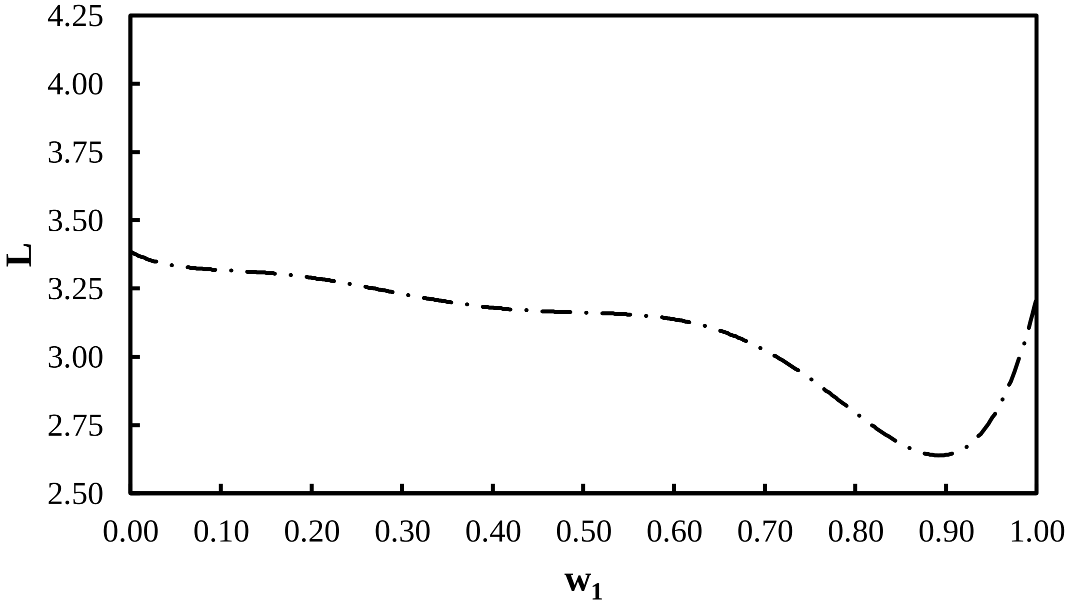

Figure (C.18): Length of stilling basin versus different value of objective weights for double solid semicircle deflector.

الخلاصة

مشكلة البحث التي تناولتها هذه الدراسة هي الاستخدام المحدود للنماذج النظرية التي تتضمن تدفقا على مرحلتين يتكون من الماء والرمل لمحاكاة وتحليل التآكل حول الهياكل الهيدروليكية. ويشير هذا القيد إلى أن هناك حاجة إلى مزيد من التحقيق في هذا المجال. لمعالجة هذه الفجوة البحثية، أجرى البحث الحالي تجارب مختبرية واستخدم نموذج ديناميكا الموائع الحسابية (CFD) للتحقيق في خصائص التدفق وأنماط النحر في اتجاه مجرى الهيكل الهيدروليكي. على وجه التحديد، بحثت الدراسة في استخدام أربعة أشكال أساسية للعاكسات المغمورة (مثلث مثقب واحد، مثلث صلب مزدوج، نصف دائرة مثقبة مفردة، ونصف دائرة صلبة مزدوجة) بزوايا ومواضع مختلفة على طول اتجاه التدفق. كان الهدف من الدراسة هو مقارنة فعالية هذه العاكسات في تقليل النحر في ظل التدفق المختلفة ومقارنتها بالحالة التي لم يتم فيها تركيب عاكس. من خلال معالجة هذه الفجوة البحثية، تهدف الدراسة إلى المساهمة في مجال الهندسة الهيدروليكية وتقديم رؤى حول التآكل حول الهياكل الهيدروليكية.

في هذه الدراسة، تم استخدام نمذجة ديناميكا الموائع الحسابية (CFD) لفحص كيفية تأثير الموقع والزاوية الراسية لعواكس التدفق ونسبة الممر المائي على عمق النحر عبر ظروف التدفق المختلفة. تم استخدام أربعة أنواع من العاكسات، بما في ذلك اثنين من العاكسات المثقبة المفردة (نصف دائرية ومثلثة) واثنين من العاكسات الصلبة المزدوجة (نصف دائرية ومثلثة). تم استخدام معادلات Navier-Stokes والاستمرارية باستخدام طريقة الحجم المحدود والفرق المحدود لحل حركات السوائل، بينما تم اعتماد نموذج الاضطراب RNG κ-ε لنمذجة الاضطراب. تم استخدام إجهاد القص الزائد الناتج عن المياه المتدفقة لتحديد نموذج حمل الرواسب، وتم استخدام تقنية حجم السائل (VOF) لنمذجة الأسطح الحرة. أشارت النتائج إلى أن العاكس المثقوب نصف الدائري كان الأكثر فعالية في تقليل عمق النحر الموقعي الأقصى. قلل هذا العاكس من عمق النحر الأقصى بحوالي 76.8٪، بينما قلل العاكس الصلب نصف الدائري المزدوج من عمق النحر الأقصى بحوالي 75.7٪. قلل العاكس المثقوب المثلث والعاكس الصلب المثلث المزدوج من عمق النحر الأقصى بحوالي 22٪ و71.1٪ على التوالي، عند مقارنته بحوض السكون بدون العاكس. توصي هذه النتائج بأن العاكس المثقوب نصف الدائري هو الخيار الأمثل لتقليل أقصى عمق للنحر المحلي.

تتميز المشكلة بأنها مشكلة متعددة الامثلية، الأمر الذي يتطلب الحاجة إلى تحسين عوامل متعددة في وقت واحد من أجل تحقيق حل موثوق. سهلت نتائج حل الامثلية تقدير عمق النحر وتحديد أبعاد التصميم المثلى لعاكسات التدفق، مع مراعاة الظروف المشابهة لتلك المستخدمة في هذه الدراسة.

جمهورية العراق
وزارة التعليم العالي والبحث العلمي
جامعة بابل
كلية الهندسة
قسم الهندسة المدنية

التصميم الهيدروليكي الأمثل لعواكس الجريان في حوض تسكين الناظم متعدد الفتحات

رسالة
مقدمة الى كلية الهندسة / جامعة بابل
كجزء من متطلبات نيل شهادة الماجستير في الهندسة / الهندسة المدنية / الموارد المائية

من قبل
احمد رحيم صاحب ياسين

بإشراف
أ.م.د عماد حبيب عبيد

1445 **2023**